Computational and Experimental Study of the Microstructure Evolution of Inconel 625 Processed by Laser Powder Bed Fusion

COMPUTATIONAL AND EXPERIMENTAL STUDY OF THE MICROSTRUCTURE EVOLUTION OF INCONEL 625 PROCESSED BY LASER POWDER BED FUSION

BY

PARDIS MOHAMMADPOUR, M.Sc.

A THESIS

SUBMITTED TO THE DEPARTMENT OF MATERIAL SCIENCE AND ENGINEERING

AND THE SCHOOL OF GRADUATE STUDIES

OF MCMASTER UNIVERSITY

IN PARTIAL FULFILMENT OF THE REQUIREMENTS

FOR THE DEGREE OF

DOCTOR OF PHILOSOPHY

Doctor of Philosophy (2022) McMaster University

(Material Science and Engineering) Hamilton, Ontario, Canada

TITLE:	Computational and Experimental Study of the Microstructure Evolution of Inconel 625 Processed by Laser Powder Bed Fusion
AUTHOR:	Pardis Mohammadpour M.Sc. (Material Engineering), Iran University of Science and Technology, Iran B.Sc. (Material Engineering, Metallurgy), Iran University of Science and Technology, Iran
SUPERVISOR:	Prof. Andre B. Phillion
NUMBER OF PAGES:	xxvii, 150

Preface

This Ph.D. thesis is an integrated article thesis, also known as sandwich thesis, which has been composed of six main chapters all dealing with the computational and experimental study of the LPBF-processesed INCONEL 625. The thesis is composed of three journal papers and one conference paper:

Chapter 1: Presents a review on LPBF process, IN625, and rapid solidification as well as the motivation, objectives, and research plan of this thesis.

Chapter 2: A version of this chapter is published in Additive Manufacturing Journal as a research paper: Mohammadpour, Pardis, Alex Plotkowski, and Andre B. Phillion. "Revisiting solidification microstructure selection maps in the frame of additive manufacturing." Additive Manufacturing 31 (2020): 100936.

Chapter 3: A version of this chapter is published in IOP Conference Series: Materials Science and Engineering (MCWASP XV online conference, Stockholm, Sweden). Mohammadpour, P., and A. B. Phillion. "Solidification microstructure selection maps for laser powder bed fusion of multicomponent alloys." IOP Conference Series: Materials Science and Engineering. Vol. 861. No. 1. IOP Publishing, 2020.

Chapter 4: A version of this chapter is published in Additive Manufacturing Journal: Mohammadpour, P., H. Yuan, and A. B. Phillion. "Microstructure evolution of Inconel 625 alloy during single-track Laser Powder Bed Fusion." Additive

Manufacturing 55 (2022): 102824.

Chapter 5: A version of this chapter is to be submitted to Acta Materialia: Mohammadpour, P., H. Yuan, Z. Li, and A. B. Phillion. "Evaluation of Microstructure Heterogeneity in INCONEL 625 Thin-wall Fabricated by Laser Powder Bed Fusion Additive Manufacturing.".

Chapter 6: Summarizes the main conclusions of the thesis, outlines the strength and limitations the outcomes, and highlights some future work suggestions. Moreover, it presents the contribution of this research to the literature.

Abstract

This study aims to improve the Additive Manufacturing (AM) design space for the popular multi-component Ni alloy Inconel 625 (IN625) thorough investigating the microstructural evolution, namely the solidification microstructure and the solid-state phase transformations during the Laser Powder Bed Fusion (LPBF) process. Highly non-equilibrium solidification and the complex reheating conditions during the LPBF process result in the formation of various types of solidification microstructures and grain morphologies which consequently lead to a wide range of mechanical properties. Understanding the melt's thermal conditions, alloy chemistry, and thermodynamics during the rapid solidification and solid-state phase transformation in AM processes will help to control material properties and even produce a material with specific microstructural features suited to a given application. This research helps to better understand the process-microstructure-property relationships of LPBF IN625.

First, a set of simple but effective analytical solidification models were employed to evaluate their ability to predict the solidification microstructure in AM applications. As a case study, Solidification Microstructure Selection (SMS) maps were created to predict the solidification growth mode and grain morphology of a ternary Al-10Si-0.5Mg alloy manufactured by the LPBF process. The resulting SMS maps were validated against the experimentally obtained LPBF microstructure available

in the literature for this alloy. The challenges, limitations, and potential of the SMS map method to predict the microstructural features in AM were comprehensively discussed.

Second, The SMS map method was implemented to predict the solidification microstructure and grain morphology in an LPBF-built multi-component IN625 alloy. A single-track LPBF experiment was performed utilizing the EOSINT M280 machine to evaluate the SMS map predictions. The resulting microstructure was characterized both qualitatively and quantitatively in terms of the solidification microstructure, grain morphology, and Primary Dendrite Arm Spacing (PDAS). Comparing the experimentally obtained solidification microstructure to the SMS map prediction, it was found that the solidification mode and grain morphology of the primary phase were correctly predicted by the SMS maps method. However, this technique does not predict the formation of precipitates thus requiring a more comprehensive numerical method such as CALculation of PHAse Diagrams (CALPHAD) approach.

Third, to further investigate the microsegregation and precipitation in IN625, Scanning Transmission Electron Microscopy (STEM) using Energy-Dispersive X-ray Spectroscopy (EDS), High-Angle Annular Dark-Field Scanning Transmission Electron Microscopy (HAADF-STEM), Scheil-Gulliver (with solute trapping) model, and DIffusion-Controlled TRAnsformations (DICTRA) method were employed. It was found that the microstructural morphology mainly consists of the Nickel-Chromium (γ-FCC) dendrites and a small volume fraction of precipitates embedded into the interdendritic regions. The precipitates predicted with the computational method were compared with the precipitates identified via HAADF-STEM analysis inside the interdendritic region. The level of elemental microsegregation was overestimated in

DICTRA simulations compared to the STEM-EDS results; however, a good agreement was observed between the Scheil and STEM-EDS microsegregation estimations.

Finally, the spatial variations in the mechanical properties and the underlying microstructural heterogeneity of a multi-layer as-built LPBF part were investigated to complete the process-structure-properties relationships loop of LPBF IN625. Towards this end, numerical thermal simulation, electron microscopy, nano hardness test, and a CALPHAD approach were utilized to investigate the mechanical and microstructural heterogeneity in terms of grain size and morphology, PDAS, microsegregation pattern, precipitation, and hardness along the build direction. It was found that the as-built microstructure contained mostly columnar (Nickel–Chromium) dendrites that grew epitaxially from the substrate along the build direction. The hardness was found to be minimum in the middle and maximum in the bottom layers of the build's height. Furthermore, smaller melt pools, grains, and PDAS as well as higher thermal gradients and cooling rates were observed in the bottom layers as compared to the top layers. Microsegregation patterns in multiple layers were also simulated using DICTRA, and the results were compared with the STEM-EDS results. The mechanism of the formation of precipitates in different regions along the build direction and the precipitates' corresponding effects on the mechanical properties were also discussed.

Keywords: Rapid solidification, Solidification microstructure selection maps, Additive Manufacturing (AM), Columnar to Equiaxed Transition (CET), Inconel625, Laser Powder Bed Fusion (LPBF), Microsegregation, Microstructure heterogeneity

To my beloved parents who live 10,000 km away

I owe you everything

Acknowledgements

I would like to express my sincere gratitude to my supervisor Dr. Andre Phillion for his guidance, encouragement, and support. His wide knowledge of solidification and sharp vision of future trends formed the basis of this thesis. I would also like to thank Dr. Hatem Zurob and Dr. Mo Elbestawi for being my annual committee meeting members and providing me with great suggestions during my Ph.D. I would also like to thank my collaborators Dr. Alex Plotkowski and Dr. Hui Yuan for many useful interactions and discussions. My gratitude also goes to my best friends Niloufar Kodaei, Vince, Dr. Saharnaz Montazeri, Neda Taslimian, Abrisham, Mina, Shayan, Shima, Morteza, Arsalan Shirani, Roja, Nastaran, Bita, Neda Salari, and Dr. Arsalan Jameei for their company; Special thanks to my colleagues Dr. Yi Feng, Mohammad Ghoncheh, Zhen Li, Coleton Parks, Farheen Ahmed, Angshuman Podder, Prabhakar Pal, Kaamil Shibly, Araf Rafi, Olajide Akintayo, Kai Kang, Javier Miranda, Abishek Aria, Cole Becker, Talha Aziz, Neil, Dr. Khaled AbuSamk, Dr. Stefan Heugenhauser, Dr. Daniela Caballero, and Dr. Muhammad Nabeel for generously sharing their thoughts and knowledge. Their help and friendship have made my Ph.D. journey an unforgettable experience. Last but by no means least, I would like to thank my lovely parents, my older siblings (Pouria and Parisa), my niece (Hanna), and my twin sister (Paniz) for their unconditional love, trust, support, and endless patience.

Contents

List of Figures

List of Tables

Notation, Definitions, and Abbreviations

Abbreviations

AlSi10Mg	Al-10wt.%Si-0.5wt.%Mg
AM	Additive Manufacturing
CET	Columnar to Equiaxed Transition
CA	Cellular Automata
CALPHAD	CALculation of PHAse Diagrams
CCEM	Canadian Centre for Electron Microscopy
DICTRA	DIffusion-Controlled TRAnsformations
EBSD	Electron Backscatter Diffraction
EDS	Energy-Dispersive X-ray Spectroscopy
FEA	Finite Element Analysis

FFT	Fast Fourier Transform
HAADF	High-Angle Annular Dark-Field
HRTEM	High-Resolution Electron Microscopy
ICP	Inductively Coupled Plasma
IN625	Inconel 625
IPF	Inverse Pole Figure
L-DMD	Laser-based Direct Metal Deposition
LPBF	Laser Powder Bed Fusion
NbC	Niobium Carbide
OM	Optical Microscope
PDAS	Primary Dendrite Arm Spacing
PF	Phase-Field
PSP	Process-Structure-Property
SAED	Selected Area Electron Diffraction
SEM	Scanning Electron Microscope
SLM	Selective Laser Melting
SMS	Solidification Microstructure Selection
SSR	Scan Strategy Rotation

STEM	Scanning Transmission Electron Microscopy
TEM	Transmission Electron Microscopy
XRD	X-Ray Diffraction

Notation

V	Growth velocity
V_{sr}	Solidification rate
V_s, V_{lss}	Laser scanning speed
G	Thermal gradient
C_0	Alloy Composition
T_{PL}	Temperature at the planar interface
T_m	Melting point of pure metal
m	Liquidus slope
k	Partition coefficient
m^v	Velocity-dependent liquidus slope
k^v	Velocity-dependent partition coefficient
μ_v	Velocity-dependent interface kinetic coefficient
Pe	Péclet number

V_0	Speed of sound in the pure metal
a_0	Interatomic spacing
D	Solute diffusion coefficient
ΔT_{tip}	Non-equilibrium dendrite tip undercooling
ΔT_0^v	Non-equilibrium solidification interval
Iv	Ivantsov function
Γ	Gibbs-Thomson coefficient
Pe_d	Solutal péclet number, dendrite
E_1	Exponential integral function
σ^*	Dendrite tip selection parameter
R	Dendrite tip radius
G_c	Concentration gradient
ξ_d	Deviation from the equilibrium state
C_t	Dendrite tip composition
T_D	Dendrite tip temperature
ΔT_{eut}	Eutectic undercooling
λ	Lamellar spacing
K_1, K_2	Velocity-dependent parameters

C_0^v	Difference between the non-equilibrium composition of the two phases at the eutectic temperature
m_{eut}^v	Average velocity-dependent liquidus slope at the eutectic point
P	Infinite series
P	Laser power
$\overline{m}$	Average equilibrium liquidus slope
Pe_e	Solutal péclet number, eutectic
ξ_e	Eutectic function of the péclet number
T_{eut}	Equilibrium eutectic temperature
T_E	Eutectic interface temperature
φ	Material property
V_B	Velocity of formation of the banded structure
ϕ	Volume fraction of equiaxed grains
ΔT	Undercooling for columnar growth
ΔT	Non-equilibrium solidification range
N_0	Nucleant volume density for equiaxed grains
ΔT_n	Nucleation undercooling for equiaxed grains
n	Material constant

θ_j	Contact angle
f	Volume fraction
A	Fitting parameter
T_0	Temperature far from the heat source
r	radial distance from the moving point
λ	absorptivity
k	thermal conductivity
α	thermal diffusivity
γ"	Ni_3Nb
γ'	Ni_3Al
δ	Ni_3(Nb; Mo)
laves	(Ni; Cr; F e)$_2$(Nb; Mo;Ti)
$(\gamma - FCC)$	Nickel-chromium matrix
aqua regia	3 HCl: 1 HNO3
D_l	Diffusion coefficient in the liquid

Chapter 1

Introduction

1.1 Background

1.1.1 Additive Manufacturing

Additive Manufacturing (AM) has developed significantly and experienced a fast-growing industrial adoption since its advent in the 1980s. AM can be defined as a layer-by-layer deposition of the feedstock materials to fabricate a net-shaped 3-D part from a Computer Aided Design (CAD) model [1,2]. According to the American Society for Testing and Materials (ASTM) International Committee F42, AM processes can be categorized into seven groups; VAT Photopolymerization, Powder Bed Fusion (PBF), Directed Energy Deposition (DED), Material Jetting (MJ), Binder Jetting (BJ), and Sheet Lamination (SL). These AM methods can be used to build parts made of different materials in various industries [3,4].

There are commercial applications of all these AM techniques in the metal AM market. The largest industrial adoption of metal AM processes belongs to the Powder

Bed Fusion (PBF) method, with 54% of the whole market [5]. To initiate the PBF process, a 3D CAD model of the part must be designed and then sliced to be used in the PBF machine. The process starts by spreading a thin layer of metal powder as a feedstock over the substrate, and a heat source (electron beam or laser beam) melts the first layer based on the data from the sliced 3D design. Afterward, the build plate is lowered, and another layer of metal powder is spread across the build plate. The layering and melting process is repeated till the part is complete [2].

Laser Powder Bed Fusion (LPBF) LPBF is one of the most used PBF methods because it is a hihgly versatile and excellent candidate for fabricating non-ferrous materials such as aluminum, copper, titanium, and nickel-based superalloys . Although there are other techniques that have higher outputs, the better surface quality and higher dimensional accuracy of the LPBF process make it an exceptional choice for the metal AM industry in terms of quality assurance [6].

Figure 1.1 presents the overall correlations between the processing parameters, microstructure, and mechanical properties in LPBF processing. Frame (1) shows how alloy composition, powder characteristics, and processing parameters critically influence the governing thermal condition during the LPBF process. Frame (2) shows the different microstructural evolution modes that can occur during the LPBF process. All the parameters introduced in the first frame greatly affect the final microstructure. Due to the high laser power, scanning velocity, and repeated thermal cycles during the LPBF process, metal powders experience a complex thermal condition with rapid melting and solidification, high thermal gradient, and localized reheating and remelting, which results in obtaining various solidification microstructures and

the occurrence of solid-state transformation. Finally, frame (3) links the microstructural features to the physical properties and, consequently, the mechanical properties of the LPBF-produced products. The mechanical properties are strongly influenced by the grain morphology, modes of solidification, Primary Dendrite Arm Spacing (PDAS), grain size, solid-state transformation, and the type, size, and distribution of the precipitates in the microstructure. A small change in any of these microstructural features can significantly affect the final properties of the LPBF parts [7,8,9].

1.1.2 Inconel625

Inconel 625 (IN625) is a nickel-based superalloy strengthened mainly by the strengthening effect of alloying elements, like niobium and molybdenum, in a nickel-chromium (γ-FCC) matrix. The nominal chemical composition of IN625 based on the ASTM F3056 standard [10] is shown in Table 1.1. This alloy shows outstanding corrosion and oxidation resistance in high-temperature corrosive atmospheres, as well as excellent yield strength, creep strength, and fatigue strength due to the formation of intermetallic precipitates like γ"-Ni3Nb, δ-Ni3(Nb; Mo), laves-(Ni; Cr; Fe)$_2$(Nb; Mo; Ti) and complex carbides, including MC, M_2C, M_6C, and $M_{23}C_6$, etc., in the -FCC matrix. These properties make Inconel alloys a perfect candidate in aerospace, marine, and nuclear industries and other high-temperature application [11,12,13,14,15,16,17]. Furthermore, as a result of the low aluminum and titanium content in IN625, this alloy has good weldability, making it suitable for LPBF processing [18,19]. On the other hand, this alloy has been known to have poor machinability due to low thermal conductivity and the occurrence of work hardening [20].

In IN625 LPBF part, columnar grain growth is dominant due to the large thermal

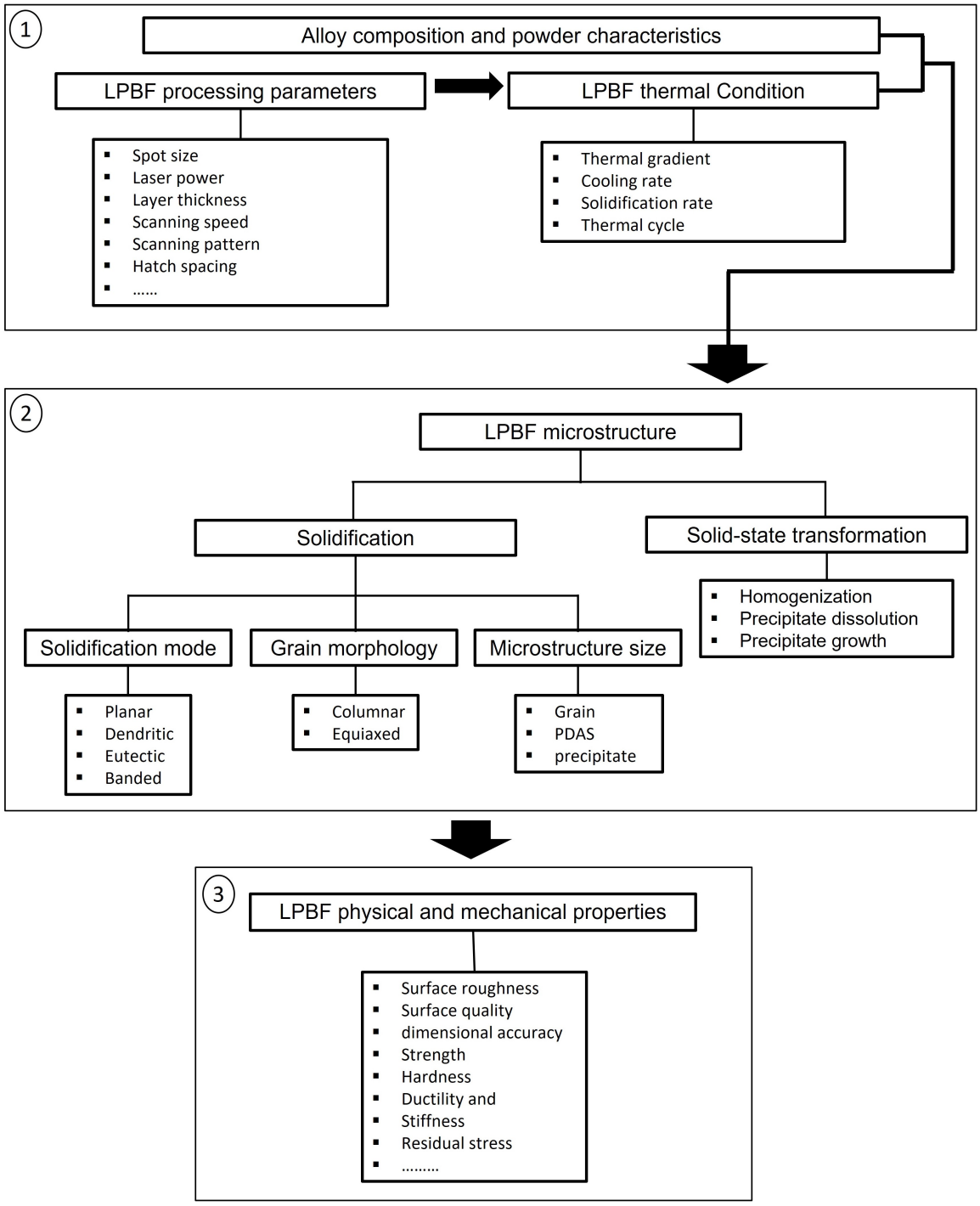

Figure 1.1: Schematic showing the overall correlations between the processing parameters, microstructure, and mechanical properties in the LPBF process.

Table 1.1: Nominal chemical composition of Inconel 625 based on the ASTM F3056 standard [10].

Element	C	Mn	Si	Cr	Co	Mo	Nb	Ti	Al	Fe	Ni
Min (wt%)	-	-	-	20.00	-	8.00	3.15	-	-	-	balance
Max (wt%)	0.10	0.50	0.50	23.00	1.00	10.00	4.15	0.40	0.40	5.00	

gradient present ahead of the solid/liquid interface during the solidification. As a result of rapid solidification, the dendritic structure contains mainly fine primary arms with a few tiny secondary arms. Some nano-size precipitates may also form in LPBF microstructure of IN625 [14,15,16,21]. This is in contrast with wrought material in which equiaxed grains, larger dendrites with the classical secondary arms, and bigger precipitates are present [22]. As shown earlier in Figure 1.1, the mechanical properties of the LPBF part are strongly influenced by microstructural evolution. For example, γ", γ', and δ enhance the hardness and tensile strength while the brittle laves and MC carbides precipitate can degrade the ductility. Moreover, the columnar grain growth causes severe anisotropic mechanical properties, and finer microstructural features result in higher hardness and tensile strength [23,24]. Several studies have been conducted to investigate the link between the initial processing parameters and the mechanical properties of the LPBF IN625 part while paying less attention to the microstructural evolution during the LPBF process and the process-microstructure-properties relationship [25,26,27,28]. Microstructure development is at the heart of all metal manufacturing processes linking properties to composition. One can control the mechanical properties of the final LPBF part by manipulating the microstructure.

1.1.3 Modeling of Microstructural Evolution during AM

Controlling the microstructure is impossible without solidification knowledge. In-situ microstructural observation is difficult during the LPBF process because of the melt pool's rapid solidification and complex thermal condition. This makes numerical methods such as the Phase-Field (PF) method and Cellular Automata (CA) as well as analytical approaches, i.e., Solidification Microstructure Selection (SMS) maps, an effective alternative to investigate the relation between solidification parameters and microstructure evolution. The use of such simulation methods has enabled the prediction of solidification characteristics, including dendrite tip shape, dendrite arm spacing, grain size and morphology, and segregation patterns, amongst others [29,30,31,32].

Although the numerical simulation of solidification microstructure is a powerful method to predict the microstructure, these methods are too complex and time-consuming. Since the simulations are on the scale of a dendrite, it will be highly time-consuming to predict the microstructure of the whole part. On the other hand, growth-controlled analytical modeling combined with interface responses (the interface temperatures as a function of interface velocities), SMS maps, and Columnar to Equiaxed Transition (CET) models have collectively grown into a simple but consistent method for predicting microstructure during rapid solidification, which can be used to expand the diversity of printable alloys with desirable properties, and consequently, take advantage of AM in different metal industries. The other advantage of the analytical approach over numerical simulation is predicting the microstructure over a wide range of composition and growth velocity in a short time. Analytical growth models [33,34,35,36], which describe the behavior of solid/liquid interface

during rapid solidification, have been proposed by Kurz, Trivedi, and colleagues for various types of growth, including planar, dendritic, eutectic, and banded. Concurrently, the columnar to equiaxed transition grain morphology has been proposed by Hunt [37], which has been extended by Gaumann et al. [38] to describe the CET transition in rapid solidification. These analytical models, combined with thermal data, can be used to create SMS maps to predict the solidification microstructures and grain morphologies that are expected to form for a given set of alloy compositions and thermal conditions.

Two types of SMS maps can be defined. Type 1 shows the stable solidification morphology for a set of growth velocities and alloy compositions under a constant thermal gradient. Type 2 indicates whether the morphology for a specific alloy composition will be expressed by columnar or equiaxed grains. Both are needed to rationalize the different kinds of microstructures achieved in AM. A tool that efficiently maps the structure–process relationship would be very informative in guiding AM development [32].

Although the SMS map method will be shown to be an efficient technique for rationalizing the microstructure and the grain morphology of a rapidly solidified microstructure, it is unable to accurately predict the formation of precipitates, especially those forming at very small volume fraction. Further, this method cannot fully predict phase formation during a commercial LPBF process due to the complicated thermal cycles that results in microstructural heterogeneity and solid-state phase transformations. The repeated thermal cycles during AM can lead to partial remelting, reheating, and resolidification in the solidified layers, which may change the local composition, microsegregation pattern, and phase transformation conditions [7,8,9]. Thus in

addition to developing the SMS map method for LPBF processing it is necessary to investigate the correlation between the spatial variations in mechanical properties and the underlying microstructural heterogeneity using alternative modelling technique. Combined electron microscopy with numerical thermal simulation and CALculation of PHAse Diagrams (CALPHAD) [39] method is an effective technique to understand the solidification and solid-state phase transformations that occur during the LPBF process of IN625.

1.2 Motivation

The industrial adoption of metal AM is growing very fast, with the largest market in North America [40]. The global metal AM market is anticipated to grow by about USD 8 billion from 2022 to 2030 [5]. Although many well-known companies, such as General Electric (GE), NASA, Airbus, and Boeing have been investing in metal AM, some manufacturing experts are not optimistic about the future of the AM market. A robust understanding of the AM technology and identification of the barriers and challenges associated with the AM application is required. The product's quality assurance plays one of the most critical roles in the survival of this technology. Among all metal AM processes, LPBF is one the most dominant technique due to its dimensional accuracy, versatility, and better surface quality [41]. Moreover, IN625 accounts for 20% of the nickel-based superalloys production and is very demanding in different industries [5,6,24]. Although the IN625 has proven to be printable via LPBF, it is necessary to investigate the whole of its microstructural features to achieve complete industrial adoption, elevate the quality of the LPBF part, and develop the required post-processing design procedures end-to-end.

1.3 Research Objectives

This thesis aims to develop new knowledge of linking the processing parameters, microstructure, and properties of LPBF-produced parts. IN625, one of the most commonly used nickel-based superalloys, is the main focus of this thesis. The specific objective of this research can be divided into four areas:

(i) To develop an analytical technique based on the SMS map approach to predict the solidification microstructure of the multi-component metal AM parts for a wide processing window;

(ii) To create SMS maps for IN625 multi-component alloy for a wide range of processing parameters. Then, to evaluate the SMS map predictions against the experimentally characterized solidification microstructure and grain morphology of an as-built LPBF IN625;

(iii) To investigate microsegregation and mechanism of the precipitate formation in LPBF microstructure of IN625; and

(iv) To explore the microstructural and mechanical heterogeneity in an as-built LPBF IN625 by investigating the correlation between microstructure, thermal evolution, and mechanical properties.

1.4 Thesis Outline

The main findings of this thesis have been written in three journal papers and a conference paper. Thus, this thesis includes the following chapters:

Chapter 1 briefly presents the background of metal LPBF processing, as well as the motivation behind this research and the thesis objectives.

Chapter 2 is the first published journal paper that addresses objective (i) centering around "SMS maps" for AM applications. In this study, a set of simple but effective analytical models is revisited and developed in the context of AM to predict the solidification microstructure and grain morphology of LPBF multi-component parts. The model is applied to the Al-10Si-0.5Mg alloy, and then the simulation results are validated against the experimental results available in the literature. Please note that this ternary alloy was chosen, instead of the IN625 10+ component alloy, because it is a simple alloy system with readily available thermodyanic information and much experimental data for validation.

Chapter 3 is a published conference paper that fulfills objective (ii). This study aims to improve the AM design space for the popular multi-component Ni alloy Inconel 625 (IN625) processed by LPBF by combining knowledge of microstructure development gained through analytical predictive approaches (discussed in chapter 2) and experimentation. Both types of SMS maps are created for the non-equilibrium solidification of this alloy. The microstructure of LPBF processed material is then characterized to validate the SMS maps predictions both qualitatively and quantitatively in terms of the solidification microstructure, grain morphology, and PDAS.

Chapter 4 is the second published journal paper that satisfies objective (iii). This study aims to take advantage of computational thermodynamics and kinetics and electron microscopy to set up a comprehensive investigation of the solidification

microstructure as well as the detailed mechanism of the formation of the precipitates during the single-track LPBF processing of IN625. Thus, this study improves our fundamental understanding of the solidification and solid-state phase transformations in nickel-based superalloys.

Chapter 5 is the third journal paper that investigates the microstructural heterogeneity in order to fulfill objective (iv). In this chapter, the correlation between the spatial variations in mechanical properties and the underlying microstructural heterogeneity of a multi-layer as-solidified LPBF IN625 part are investigated using modern electron microscopy techniques, nano-hardness testing, FEA thermal simulation [42], Scheil, and DIffusion-Controlled TRAnsformations(DICTRA) [43] simulations. The results from this study can be used as a guide to better understand the as-build LPBF microstructure to design an appropriate post-treatment process to achieve suitable mechanical properties.

Chapter 6 summarizes the overall conclusions of this thesis, introduces the strength and limitations of this study, presents suggestions for future work, and highlights the contributions of this thesis to the literature.

References

[1] J. Shah, B. Snider, T. Clarke, S. Kozutsky, M. Lacki, and A. Hosseini, "Large-scale 3d printers for additive manufacturing: design considerations and challenges," *The International Journal of Advanced Manufacturing Technology*, vol. 104, no. 9, pp. 3679–3693, 2019.

[2] T. DebRoy, H. Wei, J. Zuback, T. Mukherjee, J. Elmer, J. Milewski, A. M. Beese,

A. d. Wilson-Heid, A. De, and W. Zhang, "Additive manufacturing of metallic components–process, structure and properties," *Progress in Materials Science*, vol. 92, pp. 112–224, 2018.

[3] M. Monzón, Z. Ortega, A. Martínez, and F. Ortega, "Standardization in additive manufacturing: activities carried out by international organizations and projects," *The international journal of advanced manufacturing technology*, vol. 76, no. 5, pp. 1111–1121, 2015.

[4] A. I. F42, "Astm f42, standard for additive manufacturing technologies," 2009.

[5] A. Vafadar, F. Guzzomi, A. Rassau, and K. Hayward, "Advances in metal additive manufacturing: a review of common processes, industrial applications, and current challenges," *Applied Sciences*, vol. 11, no. 3, p. 1213, 2021.

[6] V. Bhavar, P. Kattire, V. Patil, S. Khot, K. Gujar, and R. Singh, "A review on powder bed fusion technology of metal additive manufacturing," *Additive manufacturing handbook*, pp. 251–253, 2017.

[7] W. J. Sames, K. A. Unocic, R. R. Dehoff, T. Lolla, and S. S. Babu, "Thermal effects on microstructural heterogeneity of inconel 718 materials fabricated by electron beam melting," *Journal of materials research*, vol. 29, no. 17, pp. 1920–1930, 2014.

[8] Y. Kok, X. P. Tan, P. Wang, M. Nai, N. H. Loh, E. Liu, and S. B. Tor, "Anisotropy and heterogeneity of microstructure and mechanical properties in metal additive manufacturing: A critical review," *Materials & Design*, vol. 139, pp. 565–586, 2018.

[9] Z. Liu, D. Zhao, P. Wang, M. Yan, C. Yang, Z. Chen, J. Lu, and Z. Lu, "Additive manufacturing of metals: Microstructure evolution and multistage control," *Journal of Materials Science & Technology*, vol. 100, pp. 224–236, 2022.

[10] A. International, "Astm f3056-14, standard specification for additive manufacturing nickel alloy (uns n06625) with powder bed fusion," 2014.

[11] V. Shankar, K. B. S. Rao, and S. Mannan, "Microstructure and mechanical properties of inconel 625 superalloy," *Journal of nuclear materials*, vol. 288, no. 2-3, pp. 222–232, 2001.

[12] M. Shaikh, M. Ahmad, K. Shoaib, J. Akhter, and M. Iqbal, "Precipitation hardening in inconel* 625," *Materials science and technology*, vol. 16, no. 2, pp. 129–132, 2000.

[13] G. Dey, S. Albert, D. Srivastava, M. Sundararaman, and P. Mukhopadhyay, "Microstructural studies on rapidly solidified inconel 625," *Materials Science and Engineering: A*, vol. 119, pp. 175–184, 1989.

[14] G. Dinda, A. Dasgupta, and J. Mazumder, "Laser aided direct metal deposition of inconel 625 superalloy: Microstructural evolution and thermal stability," *Materials Science and Engineering: A*, vol. 509, no. 1-2, pp. 98–104, 2009.

[15] L. E. Murr, S. M. Gaytan, D. A. Ramirez, E. Martinez, J. Hernandez, K. N. Amato, P. W. Shindo, F. R. Medina, and R. B. Wicker, "Metal fabrication by additive manufacturing using laser and electron beam melting technologies," *Journal of Materials Science & Technology*, vol. 28, no. 1, pp. 1–14, 2012.

[16] K. Amato, J. Hernandez, L. Murr, E. Martinez, S. Gaytan, P. Shindo, and S. Collins, "Comparison of microstructures and properties for a ni-base superalloy (alloy 625) fabricated by electron and laser beam melting," *Journal of Materials Science Research*, vol. 1, no. 2, p. 3, 2012.

[17] M. Sundararaman, L. Kumar, G. E. Prasad, P. Mukhopadhyay, and S. Banerjee, "Precipitation of an intermetallic phase with pt 2 mo-type structure in alloy 625," *Metallurgical and Materials Transactions A*, vol. 30, no. 1, pp. 41–52, 1999.

[18] J. DuPont, "Solidification of an alloy 625 weld overlay," *Metallurgical and Materials Transactions A*, vol. 27, no. 11, pp. 3612–3620, 1996.

[19] W. J. Sames, F. List, S. Pannala, R. R. Dehoff, and S. S. Babu, "The metallurgy and processing science of metal additive manufacturing," *International Materials Reviews*, vol. 61, no. 5, pp. 315–360, 2016.

[20] E. Ezugwu, Z. Wang, and A. Machado, "The machinability of nickel-based alloys: a review," *Journal of Materials Processing Technology*, vol. 86, no. 1-3, pp. 1–16, 1999.

[21] S. Li, Q. Wei, Y. Shi, Z. Zhu, and D. Zhang, "Microstructure characteristics of inconel 625 superalloy manufactured by selective laser melting," *Journal of Materials Science & Technology*, vol. 31, no. 9, pp. 946–952, 2015.

[22] N. Ramenatte, A. Vernouillet, S. Mathieu, A. V. Put, M. Vilasi, and D. Monceau, "A comparison of the high-temperature oxidation behaviour of conventional wrought and laser beam melted inconel 625," *Corrosion Science*, vol. 164, p. 108347, 2020.

[23] F. Xu, Y. Lv, Y. Liu, B. Xu, and P. He, "Effect of heat treatment on microstructure and mechanical properties of inconel 625 alloy fabricated by pulsed plasma arc deposition," *Physics Procedia*, vol. 50, pp. 48–54, 2013.

[24] M. Shahwaz, P. Nath, and I. Sen, "A critical review on the microstructure and mechanical properties correlation of additively manufactured nickel-based superalloys," *Journal of Alloys and Compounds*, p. 164530, 2022.

[25] I. Koutiri, E. Pessard, P. Peyre, O. Amlou, and T. De Terris, "Influence of slm process parameters on the surface finish, porosity rate and fatigue behavior of as-built inconel 625 parts," *Journal of Materials Processing Technology*, vol. 255, pp. 536–546, 2018.

[26] K. Mumtaz and N. Hopkinson, "Top surface and side roughness of inconel 625 parts processed using selective laser melting," *Rapid Prototyping Journal*, 2009.

[27] H. Soni, M. Gor, G. S. Rajput, and P. Sahlot, "A comprehensive review on effect of process parameters and heat treatment on tensile strength of additively manufactured inconel-625," *Materials Today: Proceedings*, vol. 47, pp. 4866–4871, 2021.

[28] Z. Tian, C. Zhang, D. Wang, W. Liu, X. Fang, D. Wellmann, Y. Zhao, and Y. Tian, "A review on laser powder bed fusion of inconel 625 nickel-based alloy," *Applied Sciences*, vol. 10, no. 1, p. 81, 2019.

[29] X. Wang, P. Liu, Y. Ji, Y. Liu, M. Horstemeyer, and L. Chen, "Investigation on microsegregation of in718 alloy during additive manufacturing via integrated

phase-field and finite-element modeling," *Journal of Materials Engineering and Performance*, vol. 28, no. 2, pp. 657–665, 2019.

[30] L.-Q. Chen, "Phase-field models for microstructure evolution," *Annual review of materials research*, vol. 32, no. 1, pp. 113–140, 2002.

[31] S. Raghavan and S. S. Sahay, "Modeling the grain growth kinetics by cellular automaton," *Materials Science and Engineering: A*, vol. 445, pp. 203–209, 2007.

[32] W. Kurz, "Solidification microstructure-processing maps: theory and application," *Advanced Engineering Materials*, vol. 3, no. 7, pp. 443–452, 2001.

[33] R. Trivedi and W. Kurz, "Morphological stability of a planar interface under rapid solidification conditions," *Acta Metallurgica*, vol. 34, no. 8, pp. 1663–1670, 1986.

[34] W. . Kurz, B. Giovanola, and R. Trivedi, "Theory of microstructural development during rapid solidification," *Acta Metallurgica*, vol. 34, no. 5, pp. 823–830, 1986.

[35] W. Kurz and R. Trivedi, "Banded solidification microstructures," *Metallurgical and Materials Transactions A*, vol. 27, no. 3, pp. 625–634, 1996.

[36] R. Trivedi, P. Magnin, and W. Kurz, "Theory of eutectic growth under rapid solidification conditions," *Acta Metallurgica*, vol. 35, no. 4, pp. 971–980, 1987.

[37] J. Hunt, "Steady state columnar and equiaxed growth of dendrites and eutectic," *Materials science and engineering*, vol. 65, no. 1, pp. 75–83, 1984.

[38] M. Gäumann, C. Bezencon, P. Canalis, and W. Kurz, "Single-crystal laser deposition of superalloys: processing–microstructure maps," *Acta Materialia*, vol. 49, no. 6, pp. 1051–1062, 2001.

[39] B. Sundman, H. Lukas, and S. Fries, *Computational thermodynamics: the Calphad method*. Cambridge university press New York, 2007.

[40] G. V. Research, "Additive manufacturing market size, share trends analysis report by component, by printer type, by technology, by software, by application, by vertical, by material, by region, and segment forecasts, 2022 - 2030," *Market Analysis Report*, vol. GVR-4-68039-922-9, 2021.

[41] Z. Chen, C. Han, M. Gao, S. Y. Kandukuri, and K. Zhou, "A review on qualification and certification for metal additive manufacturing," *Virtual and Physical Prototyping*, vol. 17, no. 2, pp. 382–405, 2022.

[42] P. Promoppatum, S.-C. Yao, P. C. Pistorius, and A. D. Rollett, "A comprehensive comparison of the analytical and numerical prediction of the thermal history and solidification microstructure of inconel 718 products made by laser powder-bed fusion," *Engineering*, vol. 3, no. 5, pp. 685–694, 2017.

[43] J.-O. Andersson, T. Helander, L. Höglund, P. Shi, and B. Sundman, "Thermo-calc & dictra, computational tools for materials science," *Calphad*, vol. 26, no. 2, pp. 273–312, 2002.

Chapter 2

Revisiting solidification microstructure selection maps in the frame of additive manufacturing

Complete Citation:

P. Mohammadpour, A. Plotkowski, A.B. Phillion, "Revisiting solidification microstructure selection maps in the frame of additive manufacturing," *Additive Manufacturing*, vol. 31, pp. 100936, 2020.

Revisiting solidification microstructure selection maps in the frame of additive manufacturing

P. Mohammadpour[a], A. Plotkowski[b,c], A.B. Phillion[c]

[a]*Department of Materials Science and Engineering, McMaster University, Hamilton, Canada*

[b]*Materials Science and Technology Division, Oak Ridge National Laboratory, Oak Ridge, TN, USA*

[c]*Manufacturing Demonstration Facility, Oak Ridge National Laboratory, Knoxville, TN, USA*

Abstract: Understanding microstructural development in additive manufacturing under highly non-equilibrium cooling conditions and the consequent effects on mechanical properties of the final component is critical for accelerating industrial adoption of these manufacturing techniques. In this study, simple but effective theoretical solidification models are recalled to evaluate their ability to predict of microstructural features in additive manufacturing applications. As a case study, the resulting solidification microstructure selection maps are created to predict the stable growth modality and the columnar to equiaxed transition (CET) of an Al-10Si-0.5Mg alloy processed via selective laser melting. The potential of this method in microstructural predictions for additively manufactured products, as well as outstanding challenges and limitations, are discussed.

Keywords: Rapid solidification, Solidification microstructure selection maps, Additive manufacturing, Columnar to equiaxed transition

2.1 Introduction

Metal-based additive manufacturing (AM) promises a great ability to produce complex geometries, and reduced lead times by eliminating expensive downstream processing stages [1]. However, there are a number of significant challenges that must be overcome for this set of techniques to reach wide industrial adoption. In metal AM, the process of part consolidation begins via laser, electron beam, or arc melting. The resulting non-equilibrium solidification conditions lead to a variety of microstructures - often preferentially selecting non-equilibrium growth modes or displaying variations in columnar or equiaxed grain morphologies [2,3,4] which consequently result in a wide range of mechanical properties. The microstructure achieved during solidification is a result of the melt thermal conditions, alloy chemistry, and thermodynamic properties. Understanding these phenomena will aid in reducing unwanted variability in material properties and even enable the design of site-specific microstructural features to suit a given application.

About 30 years ago, Kurz, Trivedi, and colleagues proposed a set of analytical models that describe the growth of planar [5], dendritic (KGT model [6]), eutectic (TKM model [7]), and banded [8] microstructures during rapid unidirectional solidification. Concurrently, Hunt proposed an analytical model [9], later extended by Gaumann et al. [10], to identify the thermal conditions required to transition from columnar to equiaxed grain morphologies. Collectively, these analytical expressions can be used to create Solidification Microstructure Selection (SMS) maps, *i.e.* to predict the solidification microstructure and grain morphology that forms for a set of alloy composition and thermal conditions. A tool that efficiently maps the structure - process relationship would be very informative in guiding AM development.

The creation of SMS maps is computationally efficient when compared to more complex approaches such as phase field and cellular automata and has been used to predict microstructure during laser treatment processes [11,12,13,14,15], among others. Although solidification during AM is not unidirectional at the scale of the melt pool, the assumption of local unidirectional solidification at the scale of the dendrite tips is required in order to create SMS maps using the provided analytical expressions. Recently, Kurz and Trivedi's expressions have been used to create SMS maps for an Al-12%Ce alloy to validate the suitability of this alloy for AM applications (16; 17). Although only limited thermodynamic data was available for the Al-Ce system, the authors predicted reasonably well the developed microstructure when compared against experimental data for different thermal conditions. Further, variations on Hunt's expression has been used by a number of authors to predict whether columnar or equiaxed microstructures form during metal AM [18,19,20,21,22,2].

In this study, we revisit the above analytical expressions required to create SMS maps in the context of Selective Laser Melting (SLM), a powder-bed metal AM process. The main advantages of analytical expressions is their high-throughput and simple extension to multi-component systems. Although accuracy is sacrificed, SMS maps provide the opportunity to efficiently assess a wide parameter space and to act as a guide for more detailed numerical simulations. This work provides a detailed yet concise presentation of the equations, assumptions, and limitations of the different models so that future researchers can fully utilize the SMS approach to improve the properties of SLM -produced components. As a case study, these models are applied to the Al-Si-Mg ternary system. This system is the current standard for AM of Al alloys and has readily available thermodynamic data.

2.2 Growth Models for Solidification Microstructures

Interface response, *i.e.* the solid/liquid interface temperature of a specific solidification mode as a function of interface growth velocity, V for a given alloy composition, C_0 and thermal gradient, G form the basis of Kurz and Trivedi's analytical models for predicting solidification microstructure under the non-equilibrium solidification conditions. The set of solidification modes to be considered depends on the alloy system. For a simple binary eutectic phase diagram, four possible microstructures exist: planar, dendritic, eutectic, and banded, irrespective of the actual alloy content. The microstructure having the maximum interface temperature is the one that is most stable [12].

The underlying assumption of the theoretical equations used to predict the interface responses is columnar (directional) and steady-state growth conditions on the scale of the transport phenomena that control microstructure selection. With respect to AM, on one hand the thermal behaviour in the melt pool is highly transient and may vary by many orders of magnitude. On the other hand, the analytical models are applied on the length scale of the transport phenomena (e.g. solute diffusion at the length scale of the dendrite tip) which are indeed quite short. Although additional research is required to properly quantify the limits of this assumption, it is reasonable at present to assume that this methodology can be used to rationalize microstructure trends during AM.

2.2.1 Planar Growth

Assuming linear superposition of the effects of various solute elements, the interface response for planar morphology can be written as

$$T_{PL} = T_m - \sum^{i} C_{0,i} \frac{m_i^v}{k_i^v} - \frac{V}{\mu_{k,i}}, \tag{2.1}$$

where T_{PL} is the temperature at the planar interface, T_m is the melting point of the pure metal, the summation symbol along with the subscript i allow for generalization to multi-component systems, $C_{0,i}$ is the initial composition, m_i^v, k_i^v, and $\mu_{k,i}$ are the liquidus slope, partition coefficient and interface kinetic coefficient for each element, and V is the interface velocity. The superscript v is added to both m_i and k_i to denote the velocity-dependency because of the non-equilibrium state of the interface. This is needed to predict solidification morphologies under the complex non-equilibrium conditions found in SLM. Note that a convention of defining the liquidus slopes and all compositional gradients as positive values is adopted.

The velocity-dependent liquidus slope and partition coefficient can be defined as [23,24]

$$m_i^v = m_i \left(1 + \frac{k_i - k_i^v[1 - \ln(k_i^v/k_i)]}{1 - k_i} \right), \text{and} \tag{2.2}$$

$$k_i^v = \frac{(k_i + Pe_i)}{(1 + Pe_i)}, \tag{2.3}$$

where m_i and k_i are the equilibrium liquidus slope and partition coefficient for each element assuming a linearized phase diagram, and Pe_i is the interfacial Péclet number for solute redistribution. Often, phase diagrams are not linear; this assumption is an

important limitation of current growth models for accurately predicting microstructure. Furthermore, $\mu_{k,i}$ is approximated as

$$\mu_{k,i} \approx \frac{V_0(1-k_i)}{m_i}, \tag{2.4}$$

in which V_0 is the speed of sound in the pure metal in the solid state, and Pe_i is given by

$$Pe_i = \frac{a_0 V}{D}, \tag{2.5}$$

where a_0 is the interatomic spacing and D is the solute diffusion coefficient in the liquid. D is assumed to be the same for all alloying elements while diffusion in the solid state is assumed to be negligible.

2.2.2 Dendritic Growth

The KGT [6] model and later work by Trivedi and Kurz [25] have been used for several years to calculate dendritic growth under rapid solidification conditions. Following their research, the non-equilibrium dendrite tip undercooling, ΔT_{tip}, can be written as

$$\Delta T_{tip} = \sum^{i} \Big(\frac{k_i^v \Delta T_{0,i}^v \mathrm{Iv}(Pe_d)}{1-(1-k_i^v)\mathrm{Iv}(Pe_d)} + C_{0,i}(m_i - m_i^v) + \frac{V}{\mu_{k,i}} \Big) + \frac{2\Gamma}{R} + \frac{GD}{V}, \tag{2.6}$$

where ΔT_0^v is the non-equilibrium solidification interval, Iv is the Ivantsov function, Γ is the Gibbs-Thomson coefficient, and Pe_d is the solutal Péclet number. The first four terms on the right-hand side represent the effects of the growth dynamics / non-equilibrium state, solute, kinetic attachment, and dendrite curvature on the dendrite

tip undercooling for each solute element. The last term is related to the cell growth at low interface velocities. Although not strictly required for studies of AM, it is included for completeness.

The non-equilibrium solidification interval, which is obtained from thermodynamic considerations, is given by

$$\Delta T^{v}_{0,i} = \frac{m^{v}_{i} C_0 (k^{v}_{i} - 1)}{k^{v}_{i}}. \tag{2.7}$$

The Iv function, for different morphologies of the dendrite [25,26], is given by

$$\begin{cases} \mathrm{Iv}(Pe_d) = Pe_d \exp(Pe_d)\mathrm{E}_1(Pe_d), & \text{needle} \\ \mathrm{Iv}(Pe_d) = (\pi Pe_d)^{1/2} \quad Pe_d \ll 1 & \text{plate} \\ \mathrm{Iv}(Pe_d) = 1 - \frac{1}{2Pe_d} + \frac{3}{4{Pe_d}^2} \quad Pe_d \gg 1 & \end{cases} \tag{2.8}$$

where the exponential integral function, $\mathrm{E}_1(Pe_d)$, is estimated based upon the approximation of Barry, Parlange and Li [27].

The solutal Péclet number ahead of the dendrite tip is defined as

$$Pe_d = \frac{RV}{2D}, \tag{2.9}$$

with the dendrite tip radius estimated from linear stability analysis [28] as

$$R = \left(\frac{\Gamma}{\sigma^* (\sum^{i} m_i G_{c,i} \xi_{d,i} - G)} \right)^{1/2}. \tag{2.10}$$

where σ^* is the dendrite tip selection parameter, R is the dendrite tip radius, $G_{c,i}$

is the concentration gradient in the liquid ahead of the dendrite tip, and $\xi_{d,i}$ is the deviation from the equilibrium state also known as the dendritic function of Péclet number. $\xi_{d,i}$ and $G_{c,i}$ are given by

$$\xi_{d,i} = 1 - \frac{2k_i^v}{\left[1 + \frac{1}{\sigma^* Pe_i^2}\right]^{1/2} - 1 + 2k_i^v}, \tag{2.11}$$

and

$$G_{c,i} = \frac{(C_{t,i} - C_{0,i})V}{D\ \mathrm{Iv}(Pe_d)}, \tag{2.12}$$

where $C_{t,i}$ is the dendrite tip composition,

$$C_{t,i} = \frac{C_0}{1 - (1 - k_i^v)\mathrm{Iv}(Pe_d)}. \tag{2.13}$$

Note that k_i^v is used in Eq. 2.13 instead of the equilibrium partition coefficient.

R and Pe_d are thus inter-related. Eqs. 2.8-2.13 are iteratively solved in order to determine R and Pe_d. These values are then used to calculate ΔT_{tip}. Finally, the interface temperature for dendritic morphology, T_D, can be determined,

$$T_D = T_{liq} - \Delta T_{tip}, \tag{2.14}$$

where T_{liq} is the equilibrium liquidus temperature.

It should be noted that the term σ^* comes from the dependence of the solute diffusion in the liquid on the Péclet number, which only gives the product of R and V and not the relationship between them. So, an additional constraint is required, specifically it is assumed that σ^* is constant for a given alloy system [25]. This assumption is valid as long as linear stability in dendritic growth remains valid [29].

It has been shown in more recent studies using phase field simulations that σ^* and thus dendritic growth directions can vary under certain conditions with alloy composition as well as imposed undercooling [30,31]. σ^* could thus be calculated as a function of interfacial energy, alloy composition and imposed undercooling. But this is beyond the scope of the present study.

2.2.3 Eutectic Growth

The model of lamellar eutectic growth during rapid solidification is based on the TMK approach [7], which links the eutectic undercooling, ΔT_{eut}, to V and lamellar spacing, λ. In this model,

$$\Delta T_{eut} = K_1 \lambda V + \frac{K_2}{\lambda}, \text{and} \tag{2.15}$$

$$\lambda^2 \, V = \frac{K_2}{K_1}, \tag{2.16}$$

where K_1 and K_2 are given by velocity-dependent parameters,

$$K_1 = \sum^{i} \left(\frac{m^v_{eut,i} C^v_{0,i}}{D} \frac{P}{f_{\alpha,i} f_{\beta,i}} \right), \text{and} \tag{2.17}$$

$$K_2 = 2 \sum^{i} m^v_{eut,i} \left(\frac{\Gamma_{\alpha,i} \sin\theta_{\alpha,i}}{m^v_{\alpha,i} f_{\alpha,i}} + \frac{\Gamma_{\beta,i} \sin\theta_{\beta,i}}{m^v_{\beta,i} f_{\beta,i}} \right). \tag{2.18}$$

For planar and dendritic growth, the calculations are performed on a single phase; however calculations for eutectic growth must consider two phases: the solute lean α phase and the solute rich β phase. Thus $f_{j,i}$ and $\theta_{j,i}$ are the the volume fraction and contact angle of phase j for the binary system with solute i, $m^v_{j,i}$ is calculated using

Eq. 2.2, $m^v_{eut,i}$ is the average velocity-dependent liquidus slope at the eutectic point, $C^v_{0,i}$ is the difference between the non-equilibrium composition of the two phases at the eutectic temperature, and P is an infinite series. Some of these terms require further definition. Specifically,

$$m^v_{eut,i} = \overline{m}_i \left(1 + \frac{k_i - k^v_i[1 - \ln(k^v_i/k_i)]}{1 - k_i} \right), \tag{2.19}$$

where $\overline{m}_i$ is the average equilibrium liquidus slope given by $\overline{m}_i = \frac{m_{\alpha,i} \cdot m_{\beta,i}}{m_{\alpha,i} + m_{\beta,i}}$,

$$C^v_{0,i} = C_{\beta,i} - k^v_{\beta,i}\Big(\frac{T_{m,i} - T_E}{m^v_{\beta,i}}\Big) - k^v_{\alpha,i}\Big(\frac{T_{m,p} - T_E}{m^v_{\alpha,i}}\Big), \tag{2.20}$$

where $k^v_{j,i}$ is calculated by Eq. 2.3, $T_{m,p}$ is the melting temperature of the pure metal, $T_{m,i}$ is the melting temperature of the second element or the intermetallic compound, and

$$P \approx 0.335\big(f_{\alpha,i} f_{\beta,i}\big)^{1.65} \xi_{e,i}. \tag{2.21}$$

For eutectic growth, the solutal Péclet number, Pe_e and the eutectic function of the Péclet number, $\xi_{e,i}$, are given by

$$Pe_e = \frac{\lambda V}{2D}, \text{and} \tag{2.22}$$

$$\xi_{e,i} = 1 - \frac{2.5\pi/Pe_e}{\left[1 + (\frac{2.5\pi}{Pe_e})^2\right]^{1/2} - 1 + 2k^v_i}. \tag{2.23}$$

The use of k^v_i within Eq. 2.23 implies that the partition coefficient of the α and β phases are equal. Either this assumption or the assumption that the α and β liquidus slopes are equal is required for the problem to be analytically tractable. A

numerical model could be used to eliminate this assumption, but this would obviously be more complex and computationally expensive. Finally, the interface temperature for eutectic growth, T_E, is calculated by

$$T_E = T_{eut} - \Delta T_{eut}\,, \tag{2.24}$$

where T_{eut} is the equilibrium eutectic temperature. Eqs. 3.3-2.24 are iteratively solved in order to determine T_E.

In some alloying system like Al-Si, due to the faceted interface of the Si phase, the resulting eutectic is irregular. For an irregular eutectic, the Jackson-Hunt growth model can be extended by defining a criterion to describe this microstructure in which the lamellar spacing varies. Specifically, when $\lambda = \lambda_{min}$, lamellae will stop growing and when $\lambda = \lambda_{max}$, branching will occur [28,32]. Thus, the average spacing $\bar{\lambda}$ can be defined as

$$\bar{\lambda} = \frac{\lambda_{min} + \lambda_{max}}{2} = \varphi\lambda_{ext}\,, \tag{2.25}$$

where λ_{ext} is the lamellar spacing corresponding the minimum undercooling (ΔT_{eut}) at a given interface velocity and φ is a material property. The Jackson-Hunt growth kinetic model is then

$$\bar{\lambda}\Delta T_{eut} = (\varphi^2 + 1)K_2, \tag{2.26}$$

$$\Delta T_{eut} = (\varphi^{-1} + \varphi)\sqrt{K_1 K_2}\sqrt{V}, \text{and} \tag{2.27}$$

$$\bar{\lambda}^2 V = \varphi^2 \frac{K_2}{K_1}. \tag{2.28}$$

2.2.4 Banded Structure

The final probable microstructure that could form during rapid solidification occurs when solute trapping causes a loss of equilibrium in the moving interface. This interface instability results in oscillatory behaviour between the plane front and dendritic microstructures, *i.e.* a banded structure [8,15,33]. Solute trapping occurs solely due to the high interface velocity and is not dependent on the thermal gradient [28,25]. Based on a stability analysis of the interface, the banded structure will form between the range of velocities corresponding to the minimum dendritic growth interface temperature, and the maximum planar front interface temperature. This condition can be expressed as:

$$V_B^{min} : \frac{dT_D}{dV} = 0 \text{ and } \frac{dT_D^2}{dV^2} > 0, \tag{2.29}$$

$$V_B^{max} : \frac{dT_{PL}}{dV} = 0 \text{ and } \frac{dT_{PL}^2}{dV^2} < 0. \tag{2.30}$$

where V_B is the velocity of formation of the banded structure.

2.2.5 Grain Morphology

In both dendritic and eutectic solidification [9], one must also differentiate between columnar and equiaxed grains. Most metallic AM components show anisotropy in mechanical properties due to the favourability in forming columnar grains. For some

applications this is desirable, but others require instead equiaxed grains to improve both process and product performance. In recent years there has been considerable experimental research carried out to enhance the homogeneity of AM microstructures through manipulation of G and V. Predicting the columnar-to-equiaxed transition (CET) is challenging owing to the complexity of this phenomenon. Gaumann's expression [10], building on Hunt's criterion [9], can be used to predict whether the rapidly solidified grain morphology will be columnar or equiaxed. This expression relates the volume fraction of equiaxed grains, ϕ, to G as

$$G = \frac{1}{1+n}\sqrt[3]{\frac{-4\pi N_0}{3\ln(1-\phi)}}\Delta T_c\Big(1-\frac{\Delta T_n^{n+1}}{\Delta T^{n+1}}\Big), \tag{2.31}$$

where N_0 is the nucleant volume density for equiaxed grains, ΔT is the undercooling for columnar growth, ΔT_n is the nucleation undercooling for equiaxed grains, and n is a material constant. Based on several studies, a fully equiaxed microstructure is achieved with $\phi > 0.49$, while a fully columnar microstructure is achieved with $\phi < 0.0066$ [21,34].

There are two main limitations to this approach to determining the CET. The first is the assumption of constant values for nucleant density and nucleation undercooling as these are known to be linked to alloy and nuclei composition, the presence of impurities, and the kinetics of atom attachment, and are better represented as a distribution of nucleation site characteristics [35]. A precise prediction of CET can only be obtained if the effect of these parameters on N_0 and ΔT_n are known; however, this is extremely challenging in cases where grain refiner particles are not intentionally added. Consequently, they represent a significant source of uncertainty in these CET models.

The second limitation lies within the derivation of Hunt's criterion itself, as a simplified relationship between dendrite growth velocity and undercooling that neglects the effects of thermal gradient was utilized, *i.e.* $\Delta T = \sqrt{VC_0/A}$ where A is a fitting parameter, instead of a more complex relationship such as the KGT model shown in Section 2.2. Furthermore, the same growth model was applied for both the directional growth of columnar dendrites, and non-oriented growth of equiaxed dendritic grains. The generality of the model could be improved by adopting an approach following Haines et al. [21] whereby the KGT model is used to predict undercooling for columnar dendritic, which is then substituted directly into Eq. 3.4. However, the equiaxed growth velocity was still calculated using a simplified relationship, and an appropriate equiaxed growth algorithm to assist CET predictions has not been determined.

2.3 Results and Discussion

The above set of models defines the interface temperatures of planar, dendritic, banded, and eutectic solidification microstructures, as well as the transition in grain morphology from columnar to equiaxed for a given V, G, and $C_{0,i}$. Their application requires considerable thermo-physical properties. T_m, m_i and k_i, $f_{j,i}$ can be taken from thermodynamic databases while a_0, V_0, σ^*, Γ, θ_j and D must typically be experimentally-determined, or estimated from atomistic simulations [36] and are sometimes found in the literature. All used thermophysical and thermodynamic properties are summarized in table. 3.2 The terms k_i^v and m_i^v can be calculated from Eqs. 2.2 and 2.3, and are assumed to be the same for all types of growth. Furthermore, it is assumed that the maximum value of the interface growth velocity, V, is maximally bounded by the scanning speed[37]. Scanning speeds in SLM typically vary between

≈0.3-1.4 m/s. The corresponding thermal gradient in the mushy zone duing SLM can be determined, as a first approximation, using the Rosenthal Equation [38]-an analytical solution to the heat conduction equation developed for welding that is able to estimate the temperature field around a moving heat source. The general Rosenthal solution equation is given by

$$T = T_0 + \frac{\lambda P}{2\pi k r} \exp\left[-\frac{V_s(x+r)}{2\alpha} \right] \tag{2.32}$$

where T_0 is the temperature far from the heat source, r is the radial distance from the moving point, λ is absorptivity, k and α are thermal conductivity and diffusivity, and P is laser power. Applying this equation to the common AM alloy Al-10wt.%Si-0.5wt.%Mg (AlSi10Mg) while assuming an energy input of $P = 200$W and a scanning speed $V_s = 1.4$ m/s [39], the SLM thermal gradients along the edge of the radius of the melt pool range from 10^6K/m to 10^9K/m.

Although the Rosenthal solution is a very quick way to predict the thermal history, due to the use of various simplifying assumptions, it gives only a rough estimation of the temperature profile. One of the most important limitations of the Rosenthal solution is the neglection of convection, latent heat, and the effects of temperature-dependent properties in the melt pool. Marangoni flow, i.e., an inevitable phenomenon resulting from a high heat input during laser heating and its influence on the local temperature-dependent surface tension, may cause significant variation in the melt pool shape and resulting thermal profile. To address this limitation, future work will involve a precise thermal-flow calculation using numerical methods.

Table 2.1: Physical and thermodynamic properties of Al-Si-Mg system [13,35,40,41,42].

Parameter		**Unit**
Initial composition of Si, $C_{0,Si}$	10	wt%
Initial composition of Mg, $C_{0,Mg}$	0.5	wt%
Melting temperature of pure Al, $T_{m,Al}$	933.33	K
Melting temperature of pure Si, $T_{m,Si}$	1687	K
Eutectic composition, C_{Eut}	12.63	wt%Si
Eutectic temperature, T_{Eut}	848	K
Liquidus slope of phase α in Al-Si isopleth system, $m_{\alpha,Si}$	6.74	$\text{Kwt\%}^{-1}$
Liquidus slope of phase α in Al-Mg isopleth system, $m_{\alpha,Mg}$	3.1	$\text{Kwt\%}^{-1}$
Liquidus slope of phase Si Al-Si isopleth system, m_{Si}	9.59	$\text{Kwt\%}^{-1}$
Partition coefficient of phase α in Al-Si isopleth system, $k_{\alpha,Si}$	0.131	-
Partition coefficient of phase α in Al-Mg isopleth system, $k_{\alpha,Mg}$	0.47	-
Partition coefficient of phase Si in Al-Si isopleth system, k_{Si}	5×10^{-11}	-
Gibbs-Thomson coefficient for the phase α, Γ_α	1.96×10^{-7}	mK
Gibbs-Thomson coefficient for the phase Si, Γ_{Si}	1.7×10^{-7}	mK
Contact angle of phase α, θ_α	30	degrees
Contact angle of phase Si, θ_{Si}	65	degrees
Volume fraction of phase α, f_α	0.8684	
Volume fraction of phase Si, f_{Si}	0.1316	
Diffusion coefficient in the liquid, D	3×10^{-9}	m^2s^{-1}
Speed of sound in pure Al, V_0	5100	ms^{-1}
Interatomic distance, a_0	10^{-9}	m
Material property, φ	3.2	
Nucleation undercooling, ΔT_n	2	K
Nucleation density, N_0	5×10^{10}	m^{-3}
Material parameter, n	2.5	-
Dendrite Tip Selection Parameter, σ^*	$(2\pi)^{-2}$	-

2.3.1 Interface Response

As shown in Fig. 2.1, the isopleth Al-Si phase diagram with 0.5 wt% Mg - calculated via the Thermo-Calc software using the COST 507 database-, shows that the microstructure of AlSi10Mg may possibly contain α-Al (FCC), Si (Diamond cubic) and eutectic phases. The resulting possible solidification microstructure are α-Al plane front, α-Al dendritic, Si-primary, and eutectic. The Si-planar growth is neglected due to the extremely low solubility of Al in Si. Further, it is assumed that the Si-primary growth morphology is plate-like. Thus, the second Ivantsov function in Eq.2.8, for plates, has been used for this interface response calculation.

Fig. 2.2 shows the resulting set of interface responses for the possible solidification microstructures. As previously explained in Section 2, the stable solidification microstructure is the one with the highest interface temperature. For this alloy, the stable solidification microstructure changes with increasing growth velocity as: eutectic $\rightarrow$ α-Al dendritic $\rightarrow$ banded $\rightarrow$ planar. Further, as shown in the figure, the stable solidification microstructures during SLM is expected to be eutectic, α-Al dendritic, and perhaps banded. These predictions and micrographs of SLM-produced AlSi10Mg [39,43,44,45] show reasonable agreement, specifically primary dendritic Al and a novel eutectic structure containing very small Si particles depending on the scanning speed. No banded structures have been reported in the literature. Matching predicted microstructures and micrographs is complicated by the fact that the prediction is limited to the melt pool scale; however, in AM the processing of subsequent layers will affect the microstructures of previous layers. Although it was assumed that interface growth velocity and scanning speed are equivalent, it will be the center of the melt pool which has the maximum growth velocity and thus the most

probable location for forming a banded microstructure. Regardless of the scan pattern used in AM, the top-most region of the melt pool experiences the maximum rate of growth velocity and consequently banded microstructure. In the case that layers are subsequently printed on each other, the banded microstructure will be eliminated due to the partial melting of upper regions of those previously-processed layers. The center of the melt pool is most-likely to remelt upon processing subsequent layers. It should also be noted that although the figure was created using $G = 10^6$K/m, simulations at higher values up to $G = 10^9$K/m showed no appreciable differences in form.

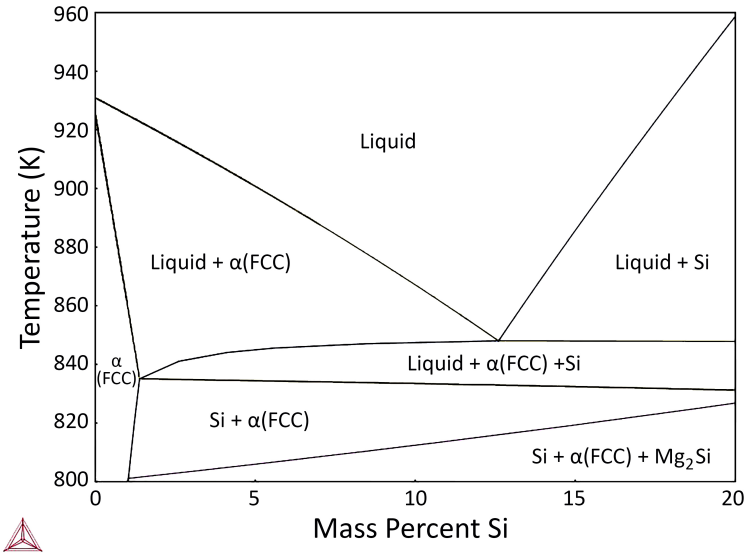

Figure 2.1: The iso-pleth phase diagram of Al-Si at (0.5wt%) Mg content, calculated using Thermo-Calc Software.

2.3.2 SMS Maps

SMS maps are graphical representations to show the stability of microstructures under specific conditions. They are useful to track phase transformation and to design AM

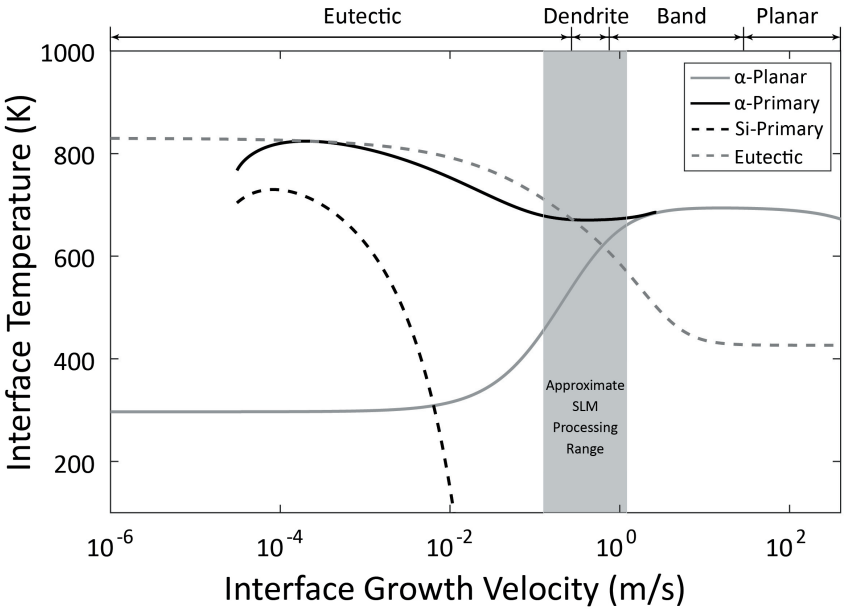

Figure 2.2: The variation in interface temperature with solidification velocity for all possible growth morphologies of the AlSi10Mg alloy experiencing a thermal gradient of 10^6K/m.

processes that will contain desirable mirostructures through manipulation of process parameters. Two types of SMS maps can be defined. Type 1 shows the stable solidification morphology for a set of growth velocities and alloy compositions under constant thermal gradient. Type 2 shows whether (or not) the morphology for a specific alloy composition will be expressed by columnar or equiaxed grains. Both are needed to rationalize the different kinds of microstructures achieved in AM.

A Type 1 SMS map for the Al-Si-Mg system, assuming $G = 10^6$ K/m and C_{Mg}=0.5 wt.%, is shown in Fig. 2.3, identifies the predominant solidification mode for a set of compositions and interface velocities. For this system at constant Mg content, the eutectic and dendritic morphologies are seen to dominate in the processing range of SLM as shown previously in Fig. 2.2 for the specific AlSi10Mg alloy. Type 1 SMS

maps can thus be thought of as interface response diagrams extended over a range of alloy nominal compositions to show trends in solidification microstructure evolution. Although there are some dissimilarities with respect to the banded structure attributed to the layered nature of the AM processing, such maps can be very effective in guiding SLM process and chemistry design to control solidification microstructure.

A Type 2 SMS map for the same alloy is shown in Fig. 2.4. This map is derived by combining the undercooling for the stable microstructure morphology predicted by the interface response with Eq.3.4. The nucleation density was estimated from [40,41,42]. Extending upon Haines's proposed approach, which utilized the undercooling from the KGT growth model to predict CET in electron beam AM (21), the term ΔT is taken as the stable value determined through the interface response analysis. Fig. 2.4 shows the stability range of dendritic grain morphologies for the AlSi10Mg alloy over a range of thermal gradients and interface velocities. As can be seen in the figure, the conditions present during SLM are predicted to result in both columnar dendritic and mixed equiaxed/columnar grain morphologies. Experimentally, the mixed region has been rarely found in the micrographs of SLM-produced AlSi10Mg [43,44,45]. It is hypothesized that this is for the same reasons as a lack of evidence for the banded structure, namely that the centre of the melt pool is likely remelted in subsequent layers. Another possible reason for a lack of experimental results showing the mixed region is that because the thermal gradients are very high, one would expect the mixed microstructure to still result in grains that compete towards columnar growth.

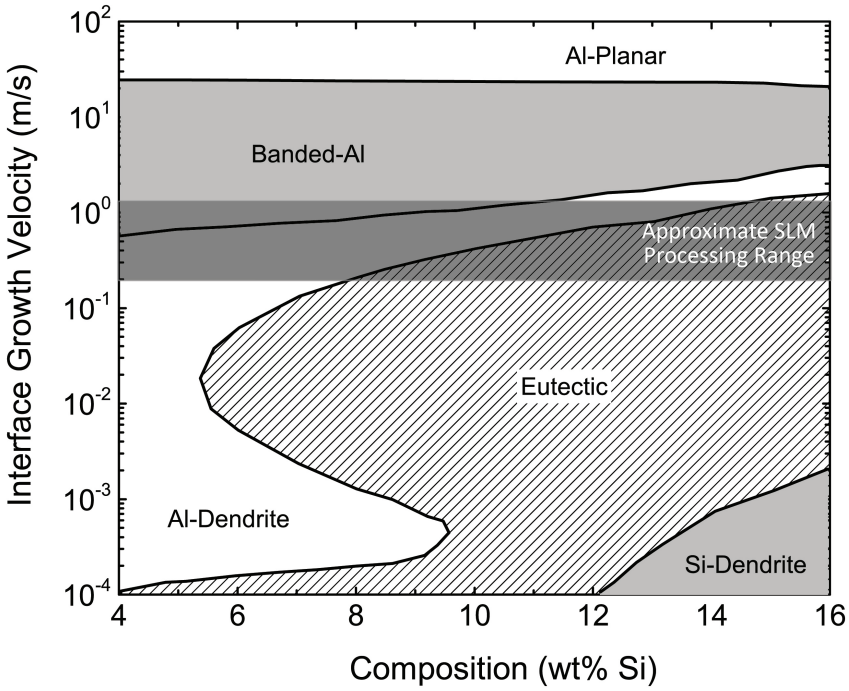

Figure 2.3: Type 1 SMS map for the Al-Si-Mg ternary system assuming $G = 10^6$K/m and $C_{Mg} = 0.5\%$wt.

2.4 Conclusions

SMS maps provide significant opportunities for improving microstructure selection during additive manufacturing. The use of analytical models that predict the interface response of the possible solidification morphologies that could exist at high thermal gradients and high solidification velocities, coupled with an analytical expression for CET will allow for new AM alloy and process development in an efficient manner, and should be used by the research community. Due to the layered nature and thermal complexity of SLM, coupling the SMS map approach with macro-scale numerical methods of heat transfer would further assist in predicting microstructure resulting from this process.

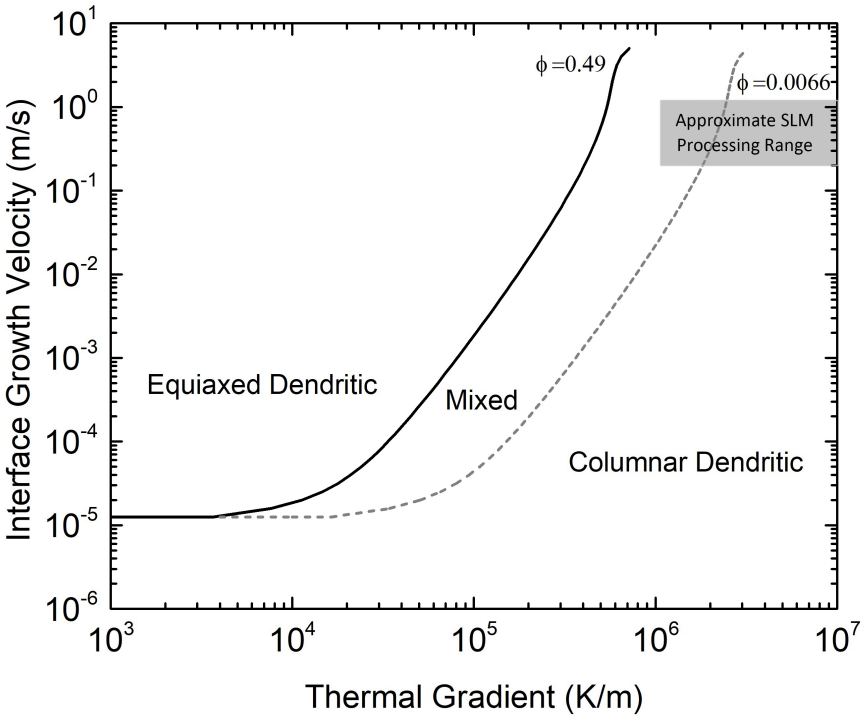

Figure 2.4: Type 2 SMS map for the Al-10wt.%Si-0.5wt.%Mg alloy.

To improve the utility of SMS maps, there is need for advancement both in materials data and with respect to the method's application to additive manufacturing. Specifically, there is need to improve the availability of thermodynamic data for new alloy systems (which is also a requirement for other modeling techniques, such as phase field), develop new approaches that do not require assumptions of a linearized phase diagram and a constant dendrite tip selection parameter, and enhance the characterization method for more accurate estimation of nucleant density and equiaxed nucleation undercooling. Furthermore, there is a need to derive strategies that can use the interface responses without the assumption of uni-directional heat flow. Although this is often a valid assumption at the scale of dendrite growth during additive manufacturing, thermal gradients and velocities may vary by several orders of magnitude

over distances as small as tens of microns.

Acknowledgements: Funding provided to PM and AP by the Natural Sciences and Engineering Council of Canada is acknowledged. Further, this manuscript has been authored by UT-Battelle, LLC under Contract No. DE-AC05-00OR22725 with the U.S. Department of Energy. Research was sponsored the U.S. Department of Energy, Office of Energy Efficiency and Renewable Energy, Advanced Manufacturing Office. The United States Government retains and the publisher, by accepting the article for publication, acknowledges that the United States Government retains a non-exclusive, paid-up, irrevocable, world-wide license to publish or reproduce the published form of this manuscript, or allow others to do so, for United States Government purposes. The Department of Energy will provide public access to these results of federally sponsored research in accordance with the DOE Public Access Plan (http://energy.gov/downloads/doe-public-access-plan).

References

[1] T. DebRoy, H. Wei, J. Zuback, T. Mukherjee, J. Elmer, J. Milewski, A. M. Beese, A. d. Wilson-Heid, A. De, and W. Zhang, "Additive manufacturing of metallic components–process, structure and properties," *Progress in Materials Science*, vol. 92, pp. 112–224, 2018.

[2] A. Hadadzadeh, B. S. Amirkhiz, J. Li, and M. Mohammadi, "Columnar to equiaxed transition during direct metal laser sintering of AlSi10Mg alloy: Effect of building direction," *Additive Manufacturing*, vol. 23, pp. 121–131, 2018.

[3] C. L. Frederick, A. Plotkowski, M. M. Kirka, M. Haines, A. Staub, E. J. Schwalbach, D. Cullen, and S. S. Babu, "Geometry-induced spatial variation of microstructure evolution during selective electron beam melting of Rene-N5," *Metallurgical and Materials Transactions A*, vol. 49, no. 10, pp. 5080–5096, 2018.

[4] M. M. Kirka, P. Nandwana, Y. Lee, and R. R. Dehoff, "Solidification and solid-state transformation sciences in metals additive manufacturing," *Scripta Materialia*, vol. 135, pp. 130–134, 2017.

[5] R. Trivedi and W. Kurz, "Morphological stability of a planar interface under rapid solidification conditions," *Acta Metallurgica*, vol. 34, no. 8, pp. 1663–1670, 1986.

[6] W. . Kurz, B. Giovanola, and R. Trivedi, "Theory of microstructural development during rapid solidification," *Acta Metallurgica*, vol. 34, no. 5, pp. 823–830, 1986.

[7] R. Trivedi, P. Magnin, and W. Kurz, "Theory of eutectic growth under rapid solidification conditions," *Acta Metallurgica*, vol. 35, no. 4, pp. 971–980, 1987.

[8] W. Kurz and R. Trivedi, "Banded solidification microstructures," *Metallurgical and Materials Transactions A*, vol. 27, no. 3, pp. 625–634, 1996.

[9] J. Hunt, "Steady state columnar and equiaxed growth of dendrites and eutectic," *Materials science and engineering*, vol. 65, no. 1, pp. 75–83, 1984.

[10] M. Gäumann, C. Bezencon, P. Canalis, and W. Kurz, "Single-crystal laser deposition of superalloys: processing–microstructure maps," *Acta Materialia*, vol. 49, no. 6, pp. 1051–1062, 2001.

[11] P. Gilgien and W. Kurz, "Microstructure selection in binary and ternary alloys," *Materials Science and Engineering: A*, vol. 178, no. 1-2, pp. 199–201, 1994.

[12] S. Fukumoto and W. Kurz, "Solidification phase and microstructure selection maps for Fe-Cr-Ni alloys," *ISIJ International*, vol. 39, no. 12, pp. 1270–1279, 1999.

[13] M. Pierantoni, M. Gremaud, P. Magnin, D. Stoll, and W. Kurz, "The coupled zone of rapidly solidified Al-Si alloys in laser treatment," *Acta Metallurgica et Materialia*, vol. 40, no. 7, pp. 1637–1644, 1992.

[14] P. Gilgien, A. Zryd, and W. Kurz, "Microstructure selection maps for Al-Fe alloys," *Acta Metallurgica et Materialia*, vol. 43, no. 9, pp. 3477–3487, 1995.

[15] S. Gill and W. Kurz, "Rapidly solidified Al-Cu alloys II. calculation of the microstructure selection map," *Acta metallurgica et materialia*, vol. 43, no. 1, pp. 139–151, 1995.

[16] A. Plotkowski, O. Rios, N. Sridharan, Z. Sims, K. Unocic, R. Ott, R. Dehoff, and S. Babu, "Evaluation of an Al-Ce alloy for laser additive manufacturing," *Acta Materialia*, vol. 126, pp. 507–519, 2017.

[17] A. Plotkowski, P. Mohammadpour, A. Phillion, and S. Babu, "Corrigendum to "evaluation of an Al-Ce alloy for additive manufacturing"[Acta Mater. 126 (2017) 507–519]," *Acta Materialia*, 2018.

[18] J. Gockel, J. Beuth, and K. Taminger, "Integrated control of solidification microstructure and melt pool dimensions in electron beam wire feed additive manufacturing of Ti-6Al-4V," *Additive Manufacturing*, vol. 1, pp. 119–126, 2014.

[19] N. Raghavan, R. Dehoff, S. Pannala, S. Simunovic, M. Kirka, J. Turner, N. Carlson, and S. S. Babu, "Numerical modeling of heat-transfer and the influence of process parameters on tailoring the grain morphology of IN718 in electron beam additive manufacturing," *Acta Materialia*, vol. 112, pp. 303–314, 2016.

[20] Y.-J. Liang, X. Cheng, J. Li, and H.-M. Wang, "Microstructural control during laser additive manufacturing of single-crystal nickel-base superalloys: New processing–microstructure maps involving powder feeding," *Materials & Design*, vol. 130, pp. 197–207, 2017.

[21] M. Haines, A. Plotkowski, C. Frederick, E. Schwalbach, and S. S. Babu, "A sensitivity analysis of the columnar-to-equiaxed transition for Ni-based superalloys in electron beam additive manufacturing," *Computational Materials Science*, vol. 155, pp. 340–349, 2018.

[22] R. R. Dehoff, M. Kirka, W. Sames, H. Bilheux, A. Tremsin, L. Lowe, and S. Babu, "Site specific control of crystallographic grain orientation through electron beam additive manufacturing," *Materials Science and Technology*, vol. 31, no. 8, pp. 931–938, 2015.

[23] M. Aziz, "Model for solute redistribution during rapid solidification," *Journal of Applied Physics*, vol. 53, no. 2, pp. 1158–1168, 1982.

[24] M. J. Aziz and T. Kaplan, "Continuous growth model for interface motion during alloy solidification," *Acta Metallurgica*, vol. 36, no. 8, pp. 2335–2347, 1988.

[25] R. Trivedi and W. Kurz, "Dendritic growth," *International Materials Reviews*, vol. 39, no. 2, pp. 49–74, 1994.

[26] G. Ivantsov, "The temperature field around a spherical, cylindrical, or pointed crystal growing in a cooling solution," in *Dokl. Akad. Nauk SSSR*, vol. 58, pp. 567–569, 1947.

[27] D. Barry, J.-Y. Parlange, and L. Li, "Approximation for the exponential integral (Theis well function)," *Journal of Hydrology*, vol. 227, no. 1-4, pp. 287–291, 2000.

[28] J. A. Dantzig and M. Rappaz, *Solidification*. Lausanne: EPFL Press, 1st ed., 2009.

[29] J. Langer and J. Müller-Krumbhaar, "Stability effects in dendritic crystal growth," *Journal of Crystal Growth*, vol. 42, pp. 11–14, 1977.

[30] J. Ramirez and C. Beckermann, "Examination of binary alloy free dendritic growth theories with a phase-field model," *Acta Materialia*, vol. 53, no. 6, pp. 1721–1736, 2005.

[31] T. Haxhimali, A. Karma, F. Gonzales, and M. Rappaz, "Orientation selection in dendritic evolution," *Nature materials*, vol. 5, no. 8, p. 660, 2006.

[32] W. Kurz and R. Trivedi, "Eutectic growth under rapid solidification conditions," *Metallurgical Transactions A*, vol. 22, no. 12, pp. 3051–3057, 1991.

[33] M. Lima and W. Kurz, "Massive transformation and absolute stability," *Metallurgical and Materials Transactions A*, vol. 33, no. 8, pp. 2337–2345, 2002.

[34] W. Kurz, C. Bezencon, and M. Gäumann, "Columnar to equiaxed transition in solidification processing," *Science and Technology of Advanced Materials*, vol. 2, no. 1, p. 185, 2001.

[35] W. Kurz and D. J. Fisher, *Fundamentals of solidification*, vol. 1. Trans Tech Publications Aedermannsdorf, Switzerland, 1986.

[36] J. Hoyt, M. Asta, T. Haxhimali, A. Karma, R. Napolitano, R. Trivedi, B. B. Laird, and J. R. Morris, "Crystal–melt interfaces and solidification morphologies in metals and alloys," *MRS Bulletin*, vol. 29, no. 12, pp. 935–939, 2004.

[37] M. Rappaz, S. David, J. Vitek, and L. Boatner, "Analysis of solidification microstructures in Fe-Ni-Cr single-crystal welds," *Metallurgical Transactions A*, vol. 21, no. 6, pp. 1767–1782, 1990.

[38] D. Rosenthal, "Mathematical theory of heat distribution during welding and cutting," *Weld J*, vol. 20, no. 5, pp. 34–220, 1941.

[39] L. Thijs, K. Kempen, J.-P. Kruth, and J. Van Humbeeck, "Fine-structured aluminium products with controllable texture by selective laser melting of pre-alloyed AlSi10Mg powder," *Acta Materialia*, vol. 61, no. 5, pp. 1809–1819, 2013.

[40] H. Nguyen-Thi, G. Reinhart, N. Mangelinck-Noël, H. Jung, B. Billia, T. Schenk, J. Gastaldi, J. Härtwig, and J. Baruchel, "In-situ and real-time investigation of columnar-to-equiaxed transition in metallic alloy," *Metallurgical and Materials Transactions A*, vol. 38, no. 7, pp. 1458–1464, 2007.

[41] A. E. Ares, S. F. Gueijman, and C. E. Schvezov, "An experimental investigation of the columnar-to-equiaxed grain transition in aluminum–copper hypoeutectic and eutectic alloys," *Journal of crystal Growth*, vol. 312, no. 14, pp. 2154–2170, 2010.

[42] H. Dong and P. D. Lee, "Simulation of the columnar-to-equiaxed transition in directionally solidified Al-Cu alloys," *Acta Materialia*, vol. 53, no. 3, pp. 659–668, 2005.

[43] X. Liu, C. Zhao, X. Zhou, Z. Shen, and W. Liu, "Microstructure of selective laser melted AlSi10Mg alloy," *Materials & Design*, vol. 168, p. 107677, 2019.

[44] W. Li, S. Li, J. Liu, A. Zhang, Y. Zhou, Q. Wei, C. Yan, and Y. Shi, "Effect of heat treatment on AlSi10Mg alloy fabricated by selective laser melting: Microstructure evolution, mechanical properties and fracture mechanism," *Materials Science and Engineering: A*, vol. 663, pp. 116–125, 2016.

[45] N. T. Aboulkhair, N. M. Everitt, I. Ashcroft, and C. Tuck, "Reducing porosity in AlSi10Mg parts processed by selective laser melting," *Additive Manufacturing*, vol. 1, pp. 77–86, 2014.

Chapter 3

Solidification microstructure selection maps for laser powder bed fusion of multicomponent alloys

Complete Citation:

P. Mohammadpour, A.B. Phillion, "Solidification microstructure selection maps for laser powder bed fusion of multicomponent alloys," *IOP Conference Series: Materials Science and Engineering*, vol. 861, no. 1, pp. 012005, 2020.

Solidification microstructure selection maps for laser powder bed fusion of multicomponent alloys

P. Mohammadpour, A.B. Phillion

Department of Materials Science and Engineering, McMaster University, Hamilton, Canada

Abstract: Solidification Microstructure Selection (SMS) maps provide a simple yet effective approach to predict the non-equilibrium solidification microstructure and grain morphology during Additive Manufacturing. In this study, SMS maps have been created for the Inconel 625 (IN625) alloy processed by Laser Powder Bed Fusion (LPBF). Toward this end, theoretical solid growth models, a model of the Columnar to Equiaxed Transition (CET), interface response theory, thermal simulation results and computational thermodynamics are utilized. The predicted microstructures are compared both qualitatively and quantitatively to experimentally-obtained micrographs. The theoretical analysis was also compared to the earlier analytical calculation for Al-10Si-0.5Mg alloy to show how differences in thermophysical properties affect the microstructural predictions. The theoretical predictions are shown to be in good agreement with the experimental results in terms of the resulting microstructure and dendrite arm spacings. A discussion on the use of SMS maps, formed over a broad range of thermophysical conditions, to help guide industry in improving LPBF microstructure, is provided.

3.1 Introduction

Laser Powder Bed Fusion (LPBF) is a mature Additive Manufacturing (AM) process that uses metal powder as a raw material, along with a laser heat source, to fabricate end-use parts with complex geometries. In metallic components, the mechanical properties are significantly affected by the microstructure—grain size, morphology, and crystallographic orientation. Although metal LPBF has been recently adopted on an industrial scale, the knowledge to optimize the microstructure and consequently mechanical properties of the final product remains inadequate. In this regard, the advanced investigation between processing parameters, solidification microstructure, and mechanical properties is necessary [1]

LPBF is characterized by extremely high solidification rates, V, due to the high laser scan speed, V_s, on the order of 0.1-1.5 m/s, and micron-sized melt pools, which thus leads to high thermal gradients, G, on the order of mega K/m. The laser power needs to be high enough to avoid a lack of fusion during laser melting, but not too high to produce keyhole-induced defects [2]. Large values of G and V change the diffusion length and finally lead to non-equilibrium effects at the solid/liquid interface during solidification [3]. Due to this complicated heat transfer condition at small length scales during LPBF, in situ microstructural observation is challenging. This makes numerical methods—including Phase-Field method (PF) and Cellular Automata (CA) as well as analytical approaches, *i.e.* solidification microstructure selection (SMS) maps [4,5]—an effective alternative for investigating the relationship between solidification parameters and microstructure. Although numerical simulation of solidification is a powerful method for predicting microstructure, these methods

are quite computationally expensive, especially for exploring structure-processing relationships [5]. Unlike PF and CA, SMS maps provide faster and more comprehensive predictions of microstructure in non-equilibrium solidification [4] and, being computationally efficient, allow for investigation over a wide range of compositions and growth velocities in a short time [4].

SMS maps are graphical charts that show the stable solidification microstructure and grain morphology under specific solidification conditions. They are useful for controlling solidification morphology through manipulating the processing parameters in order to obtain AM components with specific properties. Two types of SMS maps can be defined. The first type identifies the stability region of different solidification structures for a set of growth velocities and alloy compositions at a constant thermal gradient. For LPBF, the relevant microstructures include planar, dendritic, eutectic, and banded morphologies. The second type identifies the critical combination of interface velocity and thermal gradient at which the Columnar to Equiaxed Transition (CET) occurs for the dendritic morphology in an alloy with constant composition [3,4,6].

The analytical prediction of solidification morphologies is based on a set of growth models that describe the behaviour of the solid/liquid interface during non-equilibrium solidification. They were first proposed by Kurz et al. for various types of solid growth during directional solidification and laser treatment applications [3,7]. Utilizing Hunt's analytical model for the CET [8], later extended by Gauman et al. [6] to describe this transition during non-equilibrium solidification, columnar and equiaxed morphologies were also included. These analytical models, combined with thermal and thermodynamic data, can be used to create SMS maps [4].

This study aims to improve the AM design space for the popular multi-component Ni alloy Inconel 625 (IN625) processed by LPBF by combining knowledge of microstructure development gained through analytical predictive approaches and experimentation. The SMS maps were created for nonequilibrium solidification of this alloy. The microstructure of LPBF processed material, specifically the primary-dendrite-arm-spacing, was then characterized to validate the SMS maps both qualitatively and quantitatively. Finally, SMS map results for IN625 have been compared with previously published results for AlSi10Mg alloy [4]. These maps can be used to show how microstructure and properties are influenced by changing in solidification parameters and composition.

3.2 Creation of SMS maps

3.2.1 Description of material and phase formation

IN625 is a nickel-based superalloy which is strengthened mainly by solid solution strengthening via niobium, molybdenum, and chromium within the nickel-based (γ-FCC) matrix [9]. The nominal chemical composition of IN625 based on the ASTM F3056 standard is shown in Table 1 [10]. This alloy shows outstanding corrosion and oxidation resistance in elevated temperature/corrosive atmosphere conditions, as well as excellent yield strength, creep strength and fatigue strength due to the formation of intermetallic precipitates including γ" -Ni_3Nb, δ-Ni_3(Nb; Mo), laves-(Ni; Cr; F e)$_2$(Nb; Mo;Ti) and MC carbides in the γ-FCC matrix [9,11].

Fig. 3.1 shows an isopleth section of the Ni-Cr-Nb-Fe- Mo phase diagram with 21 wt% Cr, 5 wt% Fe, 9 wt% Mo, and 0.8 wt% Co calculated via the Thermo-Calc

Table 3.1: Chemical composition of Inconel 625 [10].

Element	C	Mn	Si	Cr	Co	Mo	Nb	Ti	Al	Fe	Ni
Min (wt%)	-	-	-	20.00	-	8.00	3.15	-	-	-	balance
Max (wt%)	0.10	0.50	0.50	23.00	1.00	10.00	4.15	0.40	0.40	5.00	

software using the TCNI9 database [12]. The composition of IN625 is shown by the dashed line. As can be seen, equilibrium solidification of this alloy results in a single solid phase, γ-FCC. However, based on the Scheil solidification path [12] and previous experiments, the microstructure of IN625 parts fabricated via LPBF contain multiple phases: γ" -Ni_3Nb, laves, and (on rare occasions) δ-Ni_3Nb in addition to γ-FCC(Ni-Cr)[9,13,14]. As can be seen in Fig. 3.1, the γ" -Ni_3Nb and laves phases must have formed through a eutectic reaction.

3.2.2 Analytical calculation

The aforementioned Kurz' and his colleagues' non-equilibrium growth models and interface response theory, i.e. the relationship between the solid/liquid interface temperature and velocity, as well as Gaumann's CET model, have been employed to create the type (1) and type (2) SMS maps. These models and calculation procedures have been documented in the literature [3,7,8] and most-recently summarized in [4] and are not completely repeated, but they are briefly discussed in this paper.

The general idea is based on calculating the undercooling of the S/L interface for all possible solidification growth morphologies while taking into account the effect of interface velocity on thermodynamic parameters in order to estimate the interface temperature over a range of C_0, G, V, and finally, to predict the microstructure under

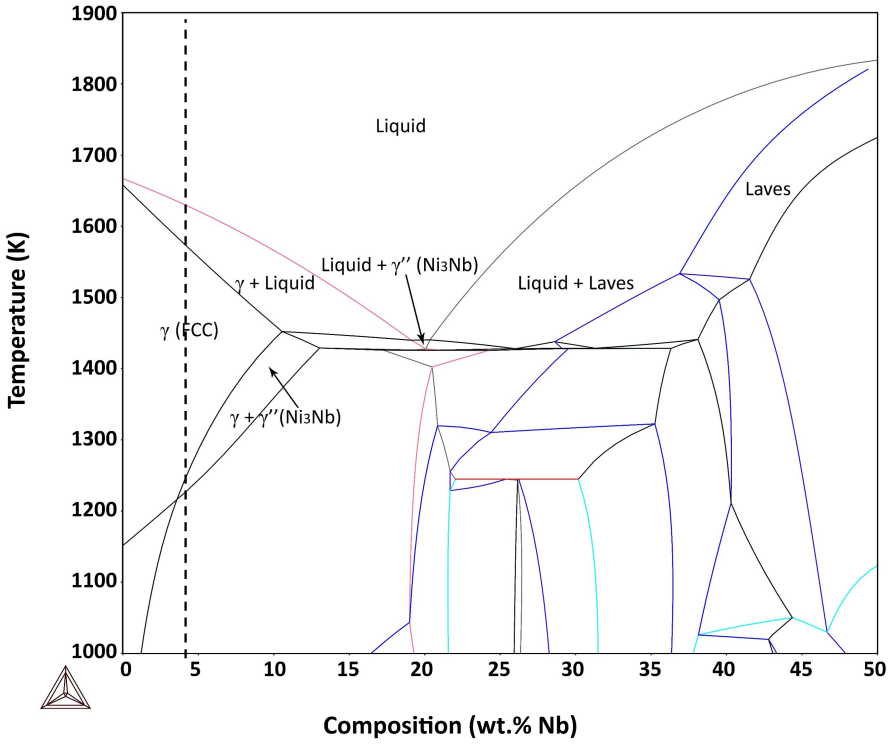

Figure 3.1: Isopleth section of Ni-Cr-Nb-Fe-Mo phase diagram with 21 wt% Cr, 5wt% Fe, 9wt% Mo, and 0.8wt% Co - calculated via the Thermo-Calc software [12].

non-equilibrium solidification conditions. The stable morphology is then the one with the highest interface temperature. The interface temperatures for planar, dendritic, and eutectic growth, i.e. the relevant morphologies for the IN625 system, are shown below,

$$T_{PL} = T_m - \sum^{i} C_{0,i} \frac{m_i^v}{k_i^v} - \frac{V}{\mu_{k,i}}, \tag{3.1}$$

$$T_D = T_{liq} - \Delta T_{tip}, \text{with}$$
$$\Delta T_{tip} = \sum^{i} \Big(\frac{k_i^v \Delta T_{0,i}^v \mathrm{Iv}(Pe_d)}{1-(1-k_i^v)\mathrm{Iv}(Pe_d)} + C_{0,i}(m_i - m_i^v) + \frac{V}{\mu_{k,i}} \Big) + \frac{2\Gamma}{R} + \frac{GD}{V} \quad (3.2)$$

$$T_E = T_{eut} - \Delta T_{eut}, \text{with} \Delta T_{eut} = K_1 \delta V + \frac{K_2}{\delta}, \text{and} \delta^2\, V = \frac{K_2}{K_1}, \quad (3.3)$$

where T_{pl}, T_D, and TE are the planar, dendritic, and eutectic interface temperatures, ΔT_{tip} and ΔT_{eut} are the dendrite tip and eutectic solidification undercooling, T_{eut}, T_{liq}, and T_m are equilibrium eutectic, liquidus, and pure metal melting temperatures, V is the solidification velocity, D_l is the diffusion coefficient in the liquid, R the dendrite tip radius, Γ the Gibbs-Thomson coefficient, $\mu_{k,i}$ the kinetic attachment, δ the lamellar spacing, and C_0, m_i^v and k_i^v the initial composition, velocity-dependent liquidus slope, and velocity-dependent partition coefficient. The i subscript refers to the alloying element. The terms m_i^v and k_i^v are calculated via Aziz' model [15] for solute redistribution during nonequilibrium solidification as $m_i^v = m_i\big(1 + (k_i - k_i^v[1 - \ln(k_i^v)/k_i])/1 - k_i\big)$, and $k_i^v = (k_i + Pe_i)/(1 + Pe_i)$ where Pe is the Péclet number, m_i and k_i are the equilibrium liquidus slope and partition coefficient for element i.The general equation of the CET model is defined as

$$G = \frac{1}{1+n} \sqrt[3]{\frac{-4\pi N_0}{3\ln(1-\phi)}} \Delta T_n \Big(1 - \frac{\Delta T_n^{n+1}}{\Delta T^{n+1}}\Big), \quad (3.4)$$

where ΔT_n and N_0 are the nucleation undercooling and nucleation density of the equiaxed grains, n is a constant and ϕ is the volume fraction of the equiaxed grains.

Previous studies of IN625 have shown that the microstructure contains the γ-FCC(Ni-Cr) phase as a matrix with the texture in $< 100 >$ as well as γ" -Ni_3Nb and

laves precipitates. Potentially, each of these phases could form during non-equilibrium solidification and as such the possible solidification microstructures that must be considered include: Planar- γ-FCC(Ni-Cr), dendrite-γ-FCC(Ni-Cr), planar- γ" -Ni_3Nb, primary- γ" -Ni_3Nb, planar-laves, primary-laves, eutectic (γ- γ"), eutectic (γ-laves) and the banded structure. Of these nine different microstructures, only four are probable, Planar- γ-FCC(Ni-Cr), dendrite- γ-FCC(Ni-Cr), eutectic (γ-γ"), and eutectic (γ-laves), given the alloys' low Nb content. Thus, only these four microstructures will be considered within the calculation of SMS maps.

To perform the necessary calculations, material physical properties are needed. Thermodynamic data, including the equilibrium liquidus slope (m), partition coefficient (k), liquidus temperature (T_{liq}), and solidus temperature (T_S) are calculated with Thermo-Calc software using TCNI9 database [12]. Other needed properties were taken from the available literature. Furthermore, the thermal gradient of the LPBF melt pool must be known. Although sophisticated methods exist, we have used the Rosenthal solution [16]—an analytical solution to the heat conduction equation developed for welding that is able to estimate the temperature field around a moving heat source—to match the desire for a computationally efficient prediction of microstructure during LPBF. The general Rosenthal solution formula, eq. 3.5, was utilized to predict the temperature history:

$$T = T_0 + \frac{\lambda P}{2\pi k r} \exp\left[-\frac{V_s(x+r)}{2\alpha} \right] \tag{3.5}$$

where T_0 is the temperature far from the heat source, r is the radial distance from the moving point, λ is absorptivity, k and α are thermal conductivity and diffusivity, and P is laser power. The thermal gradient for LPBF processing of IN625 is estimated to

be 10^6 to 10^{10} K/m within a meltpool when utilizing P=200 W and V_s=1100 mm/s as scanning power and velocity during single track LPBF processing.

3.3 LPBF single track experiments

3.3.1 Laser powder bed fusion experiment

In order to verify the microstructures predicted by the SMS maps, a single-track LPBF experiment has been performed utilizing the EOSINT M280 machine equipped with a 400 W Ytterbium fiber laser. The IN625 powder had a size distribution of 15-45μm and was processed using a power of P=200 W, scan velocity of V_s=1100 mm/s, and layer thickness of 30μm.

3.3.2 Characterization

After fabrication via AM, samples were prepared for metallography. First, samples were cut transverse cross-sectionally, mounted, polished and then etched chemically using aqua regia 3 HCl: 1 HNO3. Then, the melt pool microstructure was investigated by a KEYENCE optical microscope (OM) and a JEOL JSM-7000F Scanning Electron Microscope (SEM) equipped with an Oxford AZtecHKL Electron Backscatter Diffraction (EBSD) detector. It should be noted that cross-sections of the single track were extracted from 3 different locations along the processed track. Optical microscopy was carried out at each cross-section; However, only one location - showing the most variation in microstructure - is shown in this study.

3.4 Results

3.4.1 Qualitative comparison of the SMS maps of LPBF IN625 with experimental findings

Fig. 3.2(a) shows the interface responses of the four solidification microstructures that are expected to form during LPBF processing of IN625 as a function of interface velocity at the thermal gradient of 2×10^7 K/m. Based on the maximum interface approach, dendrite-γ-FCC(Ni-Cr) has the most stable morphology in the processing range of LPBF, as expected. The information contained in Fig. 3.2(a) can be used to create the SMS Maps. Fig. 3.2(b) and 3.2(c) show the type 1 and type 2 maps, respectively, as well as the LPBF processing conditions. As can be seen in these maps, the dendritic γ-FCC(Ni-Cr) and banded-FCC(Ni-Cr) solidification microstructure, as well as fully columnar grains, are expected to form during LPBP processing of IN625.

Fig. 3.3(a) shows an OM micrograph of the transverse crosssection of single-track LPBF processing of IN625 for the case with a scan velocity of 1100 mm/s and laser power 200 W; the hump represents the deposited layer. Fig. 3.3(b) and 3.3(c) provide the corresponding high-resolution SEM-BSE (BackScattered Electron) micrograph and the EBSD-IPF (Inverse Pole Figure) Z of the melt pool. As can be seen in Fig. 3.3(b), the microstructure consists of dendritic γ-FCC(Ni-Cr). As a result of the non-equilibrium solidification process, the dendritic structure contains mainly primary arms with very short secondary arms that result in the structure appearing to have a cellular morphology. Further, at the base of the melt pool, Fig. 3.3(c), the columnar grains appear to have the same orientation as the substrate, providing evidence that they grew epitaxially towards the centre of the deposit. The epitaxial

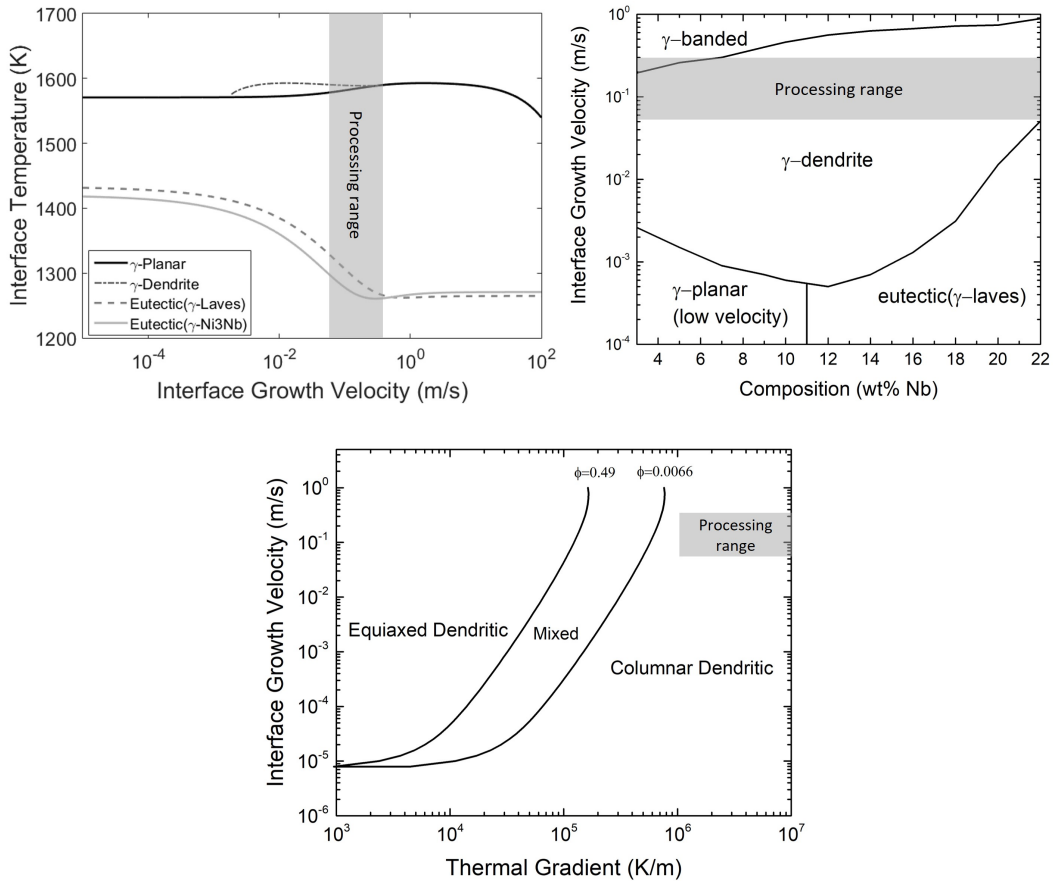

Figure 3.2: The variation of interface temperature with solidification velocity for possible growth morphologies of the IN625 alloy at $G = 2 \times 10^7$K/m, (b) Type (1) SMS map for the IN625 alloy at $G = 2 \times 10^7$K/m over a range of composition for Nb, (c) Type (2) SMS map for the IN625 alloy.

growth is related to the partial melting of the substrate while the elongated morphology is a result of the high thermal gradient and localized directional heat extraction at the edge of the melt pool.

Comparing Fig. 3.3(b) to the SMS map prediction in Fig. 3.2(b), it can be seen that while dendritic γ-FCC(Ni-Cr) is correctly predicted by the SMS map, the formation of γ-banded is not anticipated from the analytical solution. This is likely because, as shown in Fig. 3.3(c), equiaxed dendrites have formed instead ahead of the columnar

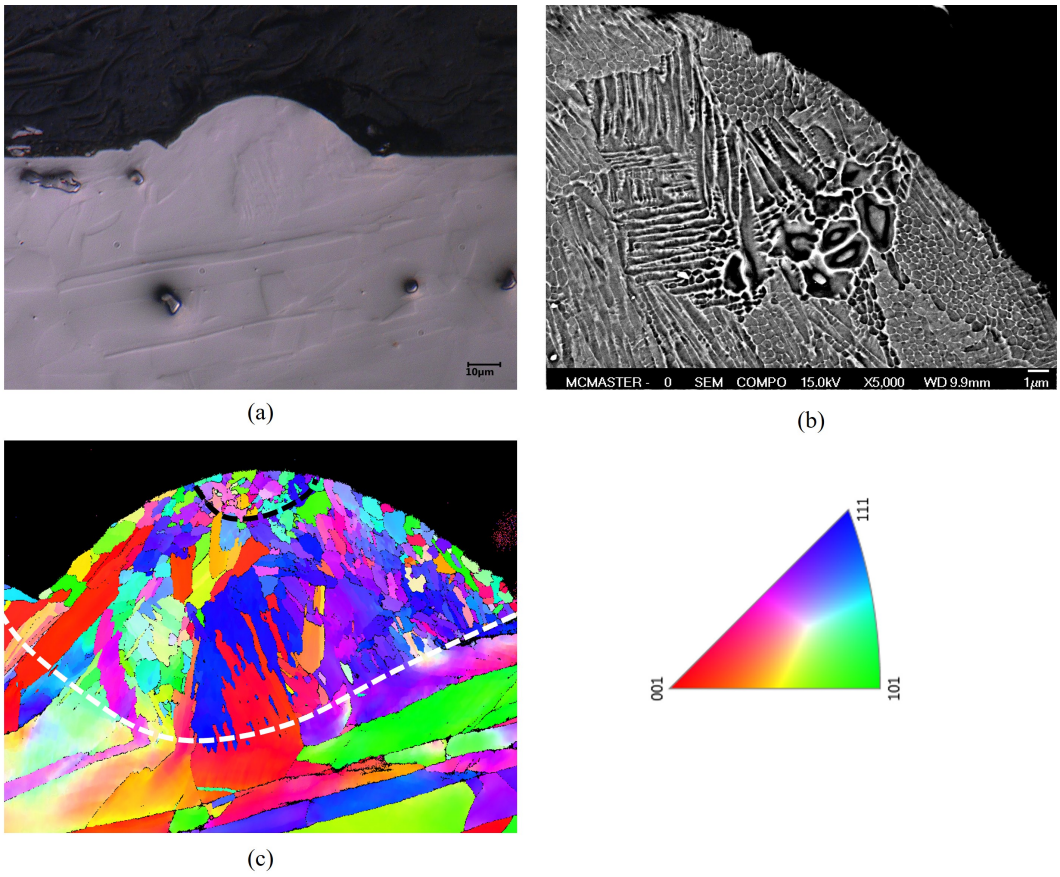

Figure 3.3: (a) OM (b) SEM-BSE micrographs, and (c) EBSD-IPF Z image of the transverse cross-section of IN625 single track melt with powder at scan velocity=1100 mm/s and laser power= 200 W.

dendrites. Neither of the SEM image, SMS map, and equilibrium phase diagram (Fig. 3.1) anticipated the formation of precipitates in the microstructure. On the other hand, Scheil solidification predicts the formation of a γ" and laves precipitates at the end of the solidification through eutectic reactions. The amount of Nb (4wt%) in IN625 is much smaller than the eutectic composition (10wt%Nb for eutectic (γ-γ") and 20wt%Nb for eutectic (γ-laves)). So, these precipitates might have formed due to the microsegregation of the alloying element in the interdendritic region.

Finally, comparing Fig. 3.3(c) to the SMS map prediction in Fig. 3.2(c), it would

appear that while columnar solidification is correctly predicted by the SMS map towards the base of the melt pool, the formation of equiaxed grains was not anticipated by the analytical solution. These equiaxed grains have nucleated ahead of the columnar front due to a drop in the thermal gradient at the end of melt pool's solidification. The calculation shown in Fig. 3.2(c) indicates that a CET will occur when the thermal gradient is less than approx. 5×10^5 K/m. Thus, it is likely that the thermal gradient near the top of the melt pool is significantly reduced as compared to what is predicted via the Rosenthal equation.

3.4.2 Quantitative comparison of primary arm spacing between experiment and calculation

Based on knowledge of the thermal gradient, Kurz and Fisher's model [17] can be used to quantify the Primary Dendrite Arm Spacing (PDAS) during dendritic growth,

$$\lambda = 4.3\left(\frac{\Delta T}{G}\right)^{\frac{1}{2}}\left(\frac{D_l \Gamma}{V k \Delta T_0}\right)^{\frac{1}{4}} \tag{3.6}$$

where λ is the primary arm spacing, k the equilibrium partition coefficient, and ΔT_0 and ΔT the equilibrium and non-equilibrium solidification range. The thermophysical parameters are listed in table 2, while the non-equilibrium solidification interval is given by $\Delta T = m^v C_0(k^v - 1)/k^v$.

Fig. 3.4(a) shows a comparison between the experimentally measured PDAS and the values calculated with Eq. 3.6. The calculated values are shown by the solid and dotted lines, for two thermal gradients. The experimentally-measured points are given by black squares. As expected, the calculation shows that an increase in the growth

Table 3.2: Thermophysical properties used for SMS maps and PDAS calculations in IN625 [12,18].

Parameter		**Unit**
Initial composition, C_0	21Cr-9Mo-5Fe-4.1Nb-0.8Co	wt%
Liquidus slopes for: $m_{Nb,\gamma}$, $m_{Nb,laves}$, m_{Nb,Ni_3Nb}	1199,1356,737	Kwt%$^{-1}$
Partition coefficients for: $k_{Nb,\gamma}$, $k_{Nb,laves}$, k_{Nb,Ni_3Nb}	0.5,0.48,0.37	-
Gibbs-Thomson coefficients for:Γ_γ, Γ_{laves}, Γ_{Ni_3Nb}	$10^{-7}, 2\times10^{-7}, 2\times10^{-7}$	mK
Diffusion coefficient in the liquid, D_l	3×10^{-9}	m^{2}s^{-1}
Material property, n	3.4	-
Nucleation undercooling, ΔT_n	1.5	K
Nucleation density, N_0	2×10^{15}	m^{-3}
Equilibrium solidification range, ΔT_0	75	K

velocity and thermal gradient decreases the PDAS. For the range of conditions [19] seen in LPBF processing, the calculated PDAS at $G = 10^7$ K/m and $G = 2\times10^7$ K/m are seen to change from 0.75 to 1.08 μm and 0.5 to 0.76 μm respectively for different growth velocities. These values match quite closely the experimental points, with locally-averaged measurements of 0.4 and 0.7 μm at two different positions within the melt pool, given uncertainties in materials properties especially D_l and the potential for Marangoni-induced convection. The PDAS is seen to decrease from the melt pool edge to the center due to the increase in the solidification velocity and the decrease in the thermal gradient. It should be noted that the experimental values of PDAS were measured from the SEM images taken from the labeled locations in the melt pool in Fig. 3.4(b).

3.4.3 Comparison of IN625 and AlSi10Mg SMS maps

SMS maps can provide guidance to improve LPBF processed microstructure and understand phase formation. To give an example, the differences between the SMS

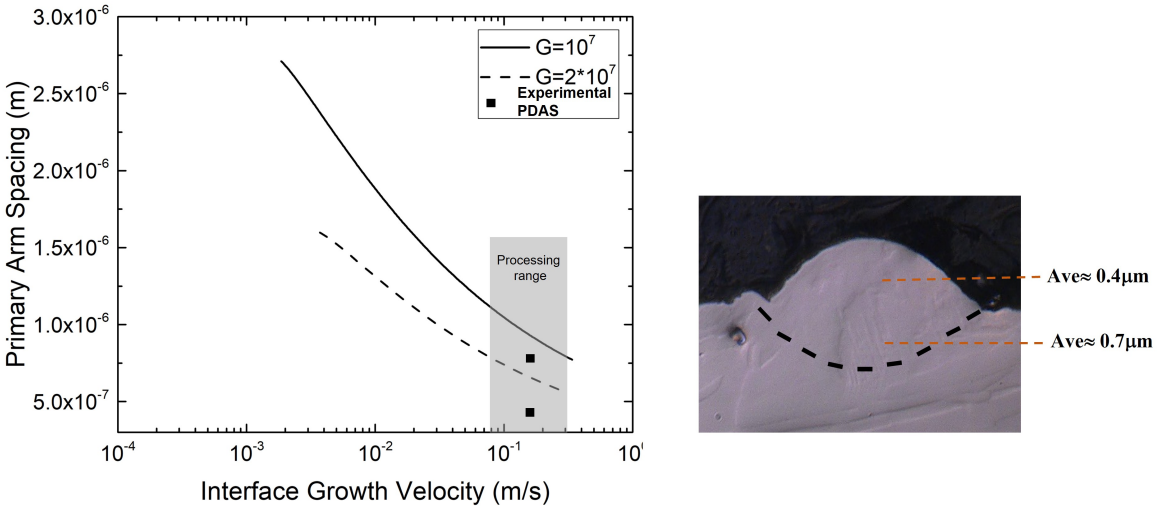

Figure 3.4: (a) Predicted PDAS over a range of growth velocity at the thermal gradient of $G = 10^7$ and 2×10^7 K/m (b) experimental PDAS.

maps of IN625, and AlSi10Mg [4], Fig. 3.5, are striking, owing to the different thermal and thermodynamic properties and compositions.

AlSi10Mg has a near-eutectic composition (12wt% Si), which leads to the formation of the eutectic microstructure. However, in IN625, the composition is far from the eutectic composition and as a result, the only predicted phase is dendritic γ-FCC(Ni-Cr). Furthermore, the grain morphology for LBPF processed AlSi10Mg is expected to be both columnar and equiaxed, whereas only the formation of columnar grains is predicted for IN625. Different parameters can affect the critical G in the columnar to equiaxed transition, such as type and composition of alloying elements, thermodynamic parameters (liquidus slope and partition coefficient), nucleation density, and nucleation undercooling. The overall contribution of these parameters produces a lower critical G for CET in IN625.

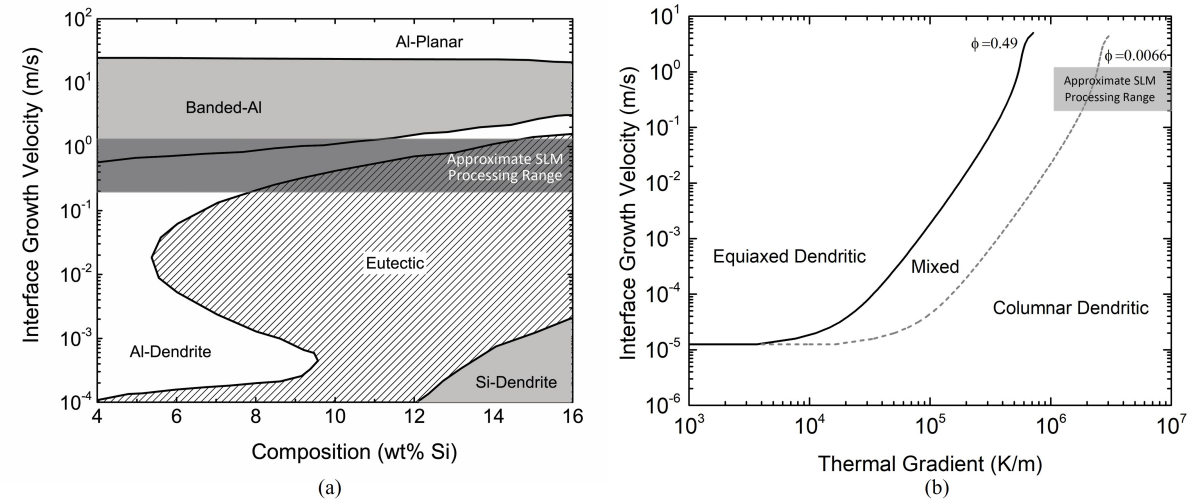

Figure 3.5: SMS maps for the AlSi10Mg alloy (a) Type (1) at $G = 10^6$ K/m and (b) Type (2) over a range of Si compositions [4].

3.5 Conclusion

The modes of solidification and grain morphology formed during LPBF processing are dependent on the G, V, and initial composition of the material. G and V are a function of not only processing parameters but also the position within the melt pool. Due to the high G and V during LBPF processing, the formation of planar, eutectic, columnar dendrite, bands and equiaxed dendrite are expected. The SMS maps predict that columnar dendritic and banded microstructure form in LPBF microstructure of IN625. However, columnar to equiaxed transition has been observed in the experimentally micrograph of this alloy; this can be related to the drop in the thermal gradient in the center of the melt to the lower value than the predicted value by the Rosenthal solution. Since the heat source is moving, the amount of G and V are changing in the melt pool, which leads to the uneven distribution of solidification modes, grain size and PDAS in the single melt pool. The microstructure of LPBF

processed IN625 mostly contains columnar dendrites with a PDAS ranging from 0.4 to 0.7 μm, in agreement with the analytical calculation results in terms of both the mode of solidification and primary arm spacing.

Funding: The authors acknowledge funding from the National Sciences and Engineering Council of Canada, and experimental support from McMaster's Additive Manufacturing Research Group.

References

[1] S. S. Babu, L. Love, R. Dehoff, W. Peter, T. R. Watkins, and S. Pannala, "Additive manufacturing of materials: Opportunities and challenges," *MRS Bulletin*, vol. 40, no. 12, pp. 1154–1161, 2015.

[2] T. DebRoy, H. Wei, J. Zuback, T. Mukherjee, J. Elmer, J. Milewski, A. M. Beese, A. d. Wilson-Heid, A. De, and W. Zhang, "Additive manufacturing of metallic components–process, structure and properties," *Progress in Materials Science*, vol. 92, pp. 112–224, 2018.

[3] W. Kurz, "Solidification microstructure-processing maps: theory and application," *Advanced Engineering Materials*, vol. 3, no. 7, pp. 443–452, 2001.

[4] P. Mohammadpour, A. Plotkowski, and A. B. Phillion, "Revisiting solidification microstructure selection maps in the frame of additive manufacturing," *Additive Manufacturing*, vol. 31, p. 100936, 2020.

[5] J. Dantzig, "Solidification modeling: Status and outlook," *JOM*, vol. 52, no. 12, pp. 18–21, 2000.

[6] M. Gäumann, R. Trivedi, and W. Kurz, "Nucleation ahead of the advancing interface in directional solidification," *Materials Science and Engineering: A*, vol. 226, pp. 763–769, 1997.

[7] W. . Kurz, B. Giovanola, and R. Trivedi, "Theory of microstructural development during rapid solidification," *Acta Metallurgica*, vol. 34, no. 5, pp. 823–830, 1986.

[8] J. Hunt, "Steady state columnar and equiaxed growth of dendrites and eutectic," *Materials science and engineering*, vol. 65, no. 1, pp. 75–83, 1984.

[9] S. Li, Q. Wei, Y. Shi, Z. Zhu, and D. Zhang, "Microstructure characteristics of inconel 625 superalloy manufactured by selective laser melting," *Journal of Materials Science & Technology*, vol. 31, no. 9, pp. 946–952, 2015.

[10] A. International, "Astm f3056-14, standard specification for additive manufacturing nickel alloy (uns n06625) with powder bed fusion," 2014.

[11] G. Dinda, A. Dasgupta, and J. Mazumder, "Laser aided direct metal deposition of inconel 625 superalloy: Microstructural evolution and thermal stability," *Materials Science and Engineering: A*, vol. 509, no. 1-2, pp. 98–104, 2009.

[12] J.-O. Andersson, T. Helander, L. Höglund, P. Shi, and B. Sundman, "Thermo-calc & dictra, computational tools for materials science," *Calphad*, vol. 26, no. 2, pp. 273–312, 2002.

[13] T. Keller, G. Lindwall, S. Ghosh, L. Ma, B. M. Lane, F. Zhang, U. R. Kattner, E. A. Lass, J. C. Heigel, Y. Idell, *et al.*, "Application of finite element, phase-field, and calphad-based methods to additive manufacturing of ni-based superalloys," *Acta materialia*, vol. 139, pp. 244–253, 2017.

[14] G. Marchese, M. Lorusso, S. Parizia, E. Bassini, J.-W. Lee, F. Calignano, D. Manfredi, M. Terner, H.-U. Hong, D. Ugues, *et al.*, "Influence of heat treatments on microstructure evolution and mechanical properties of inconel 625 processed by laser powder bed fusion," *Materials Science and Engineering: A*, vol. 729, pp. 64–75, 2018.

[15] M. Aziz, "Model for solute redistribution during rapid solidification," *Journal of Applied Physics*, vol. 53, no. 2, pp. 1158–1168, 1982.

[16] D. Rosenthal, "Mathematical theory of heat distribution during welding and cutting," *Weld J*, vol. 20, no. 5, pp. 34–220, 1941.

[17] W. Kurz and D. Fisher, "Dendrite growth at the limit of stability: tip radius and spacing," *Acta Metallurgica*, vol. 29, no. 1, pp. 11–20, 1981.

[18] Y. Lee, M. Nordin, S. S. Babu, and D. F. Farson, "Effect of fluid convection on dendrite arm spacing in laser deposition," *Metallurgical and Materials Transactions B*, vol. 45, no. 4, pp. 1520–1529, 2014.

[19] P. Promoppatum, S.-C. Yao, P. C. Pistorius, and A. D. Rollett, "A comprehensive comparison of the analytical and numerical prediction of the thermal history and solidification microstructure of inconel 718 products made by laser powder-bed fusion," *Engineering*, vol. 3, no. 5, pp. 685–694, 2017.

Chapter 4

Microstructure Evolution of Inconel 625 Alloy During Single-track Laser Powder Bed Fusion

Complete Citation:

P. Mohammadpour, H. Yuan, A.B. Phillion, "Revisiting solidification microstructure selection maps in the frame of additive manufacturing," *Additive Manufacturing*, vol. 55, pp. 102824, 2022.

Microstructure Evolution of Inconel 625 Alloy During Single-track Laser Powder Bed Fusion

P. Mohammadpour[a], H. Yuan[b], A.B. Phillion[a]

[a]*Department of Materials Science and Engineering, McMaster University, Hamilton, Canada*

[b]*Canadian Centre for Electron Microscopy, McMaster University, Hamilton, Canada*

Abstract: Elemental microsegregation and precipitate formation are inevitable during solidification of Additive Manufacturing (AM) parts. In this study, single-track Laser Powder Bed Fusion (LPBF) has been combined with optical and electron microscopy, as well as thermodynamic (CALPHAD) simulations, to evaluate the solidified microstucture and also the formation of the precipitates in an as-built LPBF microstructure of Inconel625 (IN625). It is shown that the microstructure consists mainly of columnar Nickel-Chromium (γ-FCC) cell-like dendrites which grew epitaxially from the substrate. Utilizing Scanning Transmission Electron Microscopy (STEM) with Energy-Dispersive X-ray Spectroscopy (EDS) and High-Angle Annular Dark-Field Scanning Transmission Electron Microscopy (HAADF-STEM), we have detected NbC, γ''-Ni_3Nb, and laves precipitates embedded into the interdendritic regions. The level of microsegregation and the microsegregation patterns during the solidification of primary arms are obtained by STEM-EDS, and calculated using the Scheil-Gulliver (with solute trapping) and DIffusion-Controlled TRAnsformations (DICTRA) methods. Good agreement is seen between the Scheil-Gulliver predictions and STEM-EDS observations of microsegregation, however the level of elemental

microsegregation was overestimated in DICTRA simulations as compared to the experimental result. The formation of precipitates was also evaluated computationally by calculation of driving force for the nucleation of the precipitates from the last solidified liquid where the composition and thermal information for the last solidified liquid extracted from the Scheil solidification simulation. The precipitates predicted via CALPHAD were compared with the precipitates identified via HAADF-STEM analysis inside the interdendritic region.

Keyword: Inconel625, Additive manufacturing, Laser Powder Bed Fusion (LPBF), Microsegregation, Precipitation

4.1 Introduction

Inconel 625 (IN625), a nickel-based superalloy, is used extensively in aerospace, marine, and chemical applications due to its excellent high-temperature corrosion resistance, as well as high yield, creep, fatigue, and tensile strength. Although this alloy, with a high content of hardener elements, namely niobium and molybdenum, was developed initially as a solid solution strengthened material, it also gains significant strength via precipitation hardening. In IN625, the precipitates form in a nickel-chromium matrix named γ phase [1,2,3].

The manufacture of IN625 components with complex geometries has always been a challenge due to its low thermal conductivity, poor machinability, and high hardness. However, its excellent weldability makes it a brilliant choice for high-heat-input fabrication methods. Additive Manufacturing (AM) is a layer-by-layer metal fabrication method used to produce a net-shaped 3-D part from a digital model. Laser Powder Bed Fusion (LPBF) as an AM technique uses metal powder as a feedstock and laser beam as an energy source to create a 3-D part. LPBF has attracted much attention from several Inconel alloy producers over the last decade [4,5,6,7].

Metallurgical phase transformation are highly related to thermal condition and chemical composition. In the LPBF process, metal powders experience large thermal gradient and solidification rate. Thus, the laser melted microstructure of IN625 contains mostly fine columnar γ-FCC(Ni-Cr) dendrites. However, equiaxed dendrites have also been observed in this microstructure [8,9, 10]. The formation of the various grain morphologies is dependent on the local thermal conditions as well as the local chemical composition [11,12,13].

Recently, Mohammadpour et al. [8] have analyzed the solidification microstructure

and grain morphology of a single-track IN625 processed by LPBF using Solidification Microstructure Selection (SMS) maps [13] considering the non-equilibrium solidification process. Their analytical simulations predicted the formation of γ phase but did not predict the presence of precipitates. On the other hand, using CALculation of PHAse Diagrams (CALPHAD) approach- Scheil simulation [14], they found that precipitates were predicted to form at the end of solidification. Experimental evidence of precipitation formation during laser melting of IN625 is relatively limited, but generally speaking, higher level of elemental microsegregation and less homogeneous solidification microstructures have been observed. A high amount of microsegregation can facilitate the formation of the secondary phases [15,16,17,18]. Thus, different types of precipitates, including Nb-rich, Laves-$(Fe,Cr)_2Nb$, σ, and complex carbides, including MC, M_2C, M_6C, and $M_{23}C_6$, etc., can form within the γ phase matrix during the solidification of IN625. In IN625 the dominant form for MC is niobium carbide (NbC) due to having relatively high amount of Nb. This MC type carbide may transform to M_6C and $M_{23}C_6$ carbides with the subsequent heat exposure during AM process. $M_{23}C_6$ normally contains only Cr, while M_6C may contain Nb, Mo, and Ni, depending on the degree and distribution of alloying elements [19,3,20,21,1,2,22,23].

Microstructure development of LPBF produced IN625 has been studied previously. In one study, Dinda et al. [24] evaluated microstructural evolution of IN625 during the laser aided Direct Metal Deposition (DMD) process via X-Ray Diffraction (XRD). Although the formation of precipitates was not observed directly, they attributed the change in lattice parameters to the formation of γ'-Ni_3Al, γ''-Ni_3Nb, and δ-Ni_3Nb precipitates. Later, Amato et al. [25] and Li et al. [9] detected Nb-riched

precipitates in the interdendritic region of an as-built IN625 LPBF part via Transmission Electron Microscopy (TEM) and XRD, which they attributed to γ''-Ni_3Nb. However, as crystallographic evidence was not presented, these precipitates could have also been δ-Ni_3Nb. In another study, Li et al. [26] identified NbC and MoC precipitates in the heat-treated IN625 LPBF part utilizing XRD analysis however no precipitates has been observed in an as-built part. Kreitcberg et al. [27] investigated the precipitate formation in the as-built, heat-treated, and deformed LPBF IN625 via TEM and XRD methods. They detected δ-Ni_3Nb, MC, and M_6C carbides in the heat-treated and deformed parts without identifying any precipitates in the as-built part. Meanwhile, Keller [28] studied the microsegregation of IN625 solute elements within the interdendritic region using Energy Dispersive X-Ray Spectroscopy (EDS). They identified considerable microsegregation of Mo and Nb in the interdendritic region. Although γ''-Ni_3Nb, δ-Ni_3Nb and M_6C carbides along with the Laves precipitates were observed in the heat-treated microstructure, they did not detect any precipitates in the as-built specimen. Later, Marchese et al. [29] observed some precipitate-like particles high in Nb and Mo which could have been NbC or Ni_3Nb precipitates. Zhang et al. [15] and Hu et al. [30] carried out elemental segregation analysis to investigate the mechanism for precipitate formation in IN625. While they showed that Nb and Mo locally segregate to interdendritic regions, they did not detect any precipitates in the as-built LPBF part. Lass et al. [31,32] and Gola et al. [21] confirmed the presence of the γ''-Ni_3Nb and δ-Ni_3Nb precipitates in the microstructure of the annealed LPBF IN625 using selected area electron diffraction (SAED) analysis. Recently, Dubiel et al. [33] detected MC, M23C6, and laves precipitates in an as-built Laser-Based Directed Energy Deposition (L-DED) microstructure of

IN625 using high-resolution electron microscopy (HRTEM) imaging in combination with SAED and EDS analysis. However, they did not detect any precipitates in an as-built LPBF part. Finally, Lindwall [34] performed a kinetic simulation to investigate the microstructure evolution in a heat-treated LPBF IN625 part. Their simulation showed that larger degrees of Nb segregation lead to richer interdendritic region and consequently precipitate formation.

The above studies provided rich insight into precipitation formation in heat-treated LPBF IN625 parts. However, to date there has not been a complete microstructural study on the precipitate formation in this alloy as a result of the LPBF process. To evaluate the impact of these precipitates on the mechanical properties of an LPBF part or to design an appropriate post-build heat-treatment procedure, one needs to fully identify the present precipitates in an as-built part. The purpose of this study is to take advantage of computational thermodynamic and kinetics modeling, and modern electron microscopy techniques to comprehensively investigate the solidification microstructure as well as the detailed formation mechanisms of the precipitates during single-track LPBF processing of IN625. Thus, this study will improve our fundamental understanding of the solidification and solid-state phase transformations in nickel-based superalloys. In addition, it will provide the necessary knowledge basis for evaluating microstructure evolution during industrial, i.e. multi-pass laser additive manufacturing.

4.2 Methods

4.2.1 Single-track LPBF Experiment and Characterization

A single-track IN625 sample was made from gas atomized Inconel 625 powder, supplied by Carpenter Additive Inc, utilizing an EOSINT M280 machine equipped with a 400 W Ytterbium fiber laser. The nominal chemical composition of the alloy as reported by Carpenter was C (0.02), S(0.002), Si (0.13), Mn (0.03), Co (0.18), Al (0.28), Ti (0.35), Fe(0.72), Nb(3.8), Mo(8.3), Cr(20.8), Ni (balance) (wt%), and with a size distribution of 15-45 μm. The powder was processed over a solid IN625 substrate using a laser scanning speed, v_{lss}, of 1400 mm/s, and a power, p, of 100 W. These processing parameters were determined based on an initial study whereby 35 single laser-track melts were created over a laser power range between 50 and 250 W, and a scan velocity range between 200 and 2000 mm/s. The cross-section of all these single tracks was characterized using optical microscopy, from which the processing conditions for this study were identified as being optimal in terms of melt pool geometry and defects.

For microscopy analysis, the as-built LPBF sample was cut transverse cross-sectionally; mounted, polished to a 0.05 μm surface finish; and then chemically etched with aqua regia 3 HCl: 1 HNO3 for 25 s. The specimen was characterized initially using Optical Microscopy (OM) to detect the melt pool. Then, Scanning Electron Microscopy (SEM) and Electron Backscatter Diffraction (EBSD) followed by High-Angle Annular Dark-Field-Scanning Transmission Electron Microscopy (HAADF-STEM), and Scanning Transmission Electron Microscopy-Energy-Dispersive X-ray

Spectroscopy (STEM-EDS) analyses were utilized to investigate the microsegregation and precipitation inside the as-solidified melt pool.

OM and SEM microscopy were performed using a KEYENCE OM and a JEOL JSM-7000F SEM with an Oxford Instruments Nordlys II EBSD detector. A thin foil TEM specimen was prepared using the surface Focused Ion Beam (FIB) lift-out method with a Thermo Scientific Helios G4 UXe DualBeam Plasma-FIB. The foil was extracted from a grain having a matrix $< 101 >$ crystallographic orientation within the melt pool's XZ plane. Before TEM experiments, it was cleaned with a Gatan low-energy Solarus plasma cleaner for 180 s. STEM-EDS was performed within a ThermoFisher Scientific Talos F200X TEM microscope equipped with 4 in column SDD super-X detectors operated at 200kV. HAADF-STEM imaging was performed in a FEI Titan cubed 80-300 TEM at 200 kV with a semi-convergence angle of 19 mrad and a semi-collection angle of 64-200 mrad.

4.2.2 CALPHAD-based thermodynamic calculations

Microsegregation of IN625 during LPBF processing was simulated via Thermo-Calc v2021b using two different approaches: (1) the Scheil-Gulliver model with the built-in solute tapping algorithm and (2) the DIffusion-Controlled TRAnsformations (DICTRA) kinetics diffusion model [35,36]. The calculations were performed using the NITC10, and MOBNI5 thermodynamic and mobility databases [37]. The formation of the δ-Ni_3Nb precipitate was suppressed in the Scheil-Gulliver simulation, as it was not observed experimentally anywhere in the LPBF as-built microstructure.

The Scheil-Guilliver solidification model allows for direct estimation of the level of microsegregation during solidification of multicomponent alloys assuming no diffusion

in the solid phase and perfect mixing in the liquid phase. During rapid solidification, a phenomenon known as solute trapping can occur whereby the solid/liquid interface advances without partitioning of some alloying elements. These can then become entrapped inside the solid phase thus changing phase evolution and precipitation during solidification. The amount of solute trapping and consequently the Scheil-Gulliver microsegregation predictions are dependent on the solidification speed. In the IN625 system, Nb commonly experiences solute trapping within the γ phase. Within the Thermo-Calc software, the degree of solute trapping is dependent on the solidification rate, v_{sr}. During LPBF, v_{sr} can be estimated as the product of v_{lss} and the angle between the direction of laser beam motion and a vector normal to the solidification front, i.e. $v_{sr} = v_{lss}cos(\alpha)$. In this experiment, $\alpha \approx 80^{o}$, thus v_{sr} $\approx$0.25 m/s.

The DICTRA kinetics diffusion model directly calculates elemental microsegregation by applying a 1-D non-isothermal multi-component diffusion model. Figure 4.1 shows both (a) an idealized view of two adjacent primary dendrite arms during LPBF processing and (b) the corresponding 1-D simulation domain of solidification. Initially, the domain is fully liquid at $t = 0$. At t>0 the solid-liquid interface has advanced from the core of the primary dendrite to the interdendritic region and thus the domain contains both liquid IN625 and solid γ dendrites. Elemental segregation is greatest in the last liquid to solidify, usually the liquid surrounding the secondary dendrite arms. However, since no secondary arms were observed within the LPBF-built IN625 microstructure, microsegregation from the primary dendrite core to the interdendritic liquid was investigated. Thus the domain size was assumed to be 200 nm, i.e. the one-half width of the Primary Dendrite Arm Spacing (PDAS) as measured

from the SEM micrographs. This value matches closely the analytically-calculated value of 175 nm [8], following the Kurz and Fisher model for rapid solidification. The input cooling rate, 7×10^4 K/s, was estimated from in-situ measurements of the surface temperature evolution during single-track laser melting. The measurements were made using the same thermal measurement setup as described in Rezaeifar's study [38] , i.e using an infrared thermal camera (Optris PI 08 M), but with emissivity excluded from the camera settings. Finally, to reduce the computational cost, only the alloying elements having an amount greater than 1 wt.%, as well as Fe and C were considered. This reduced alloy composition was C (0.02), Fe(0.72), Nb(3.8), Mo(8.3), Cr(20.8), Ni (balance) (wt.%). To further reduce computational cost, precipitate formation was excluded.

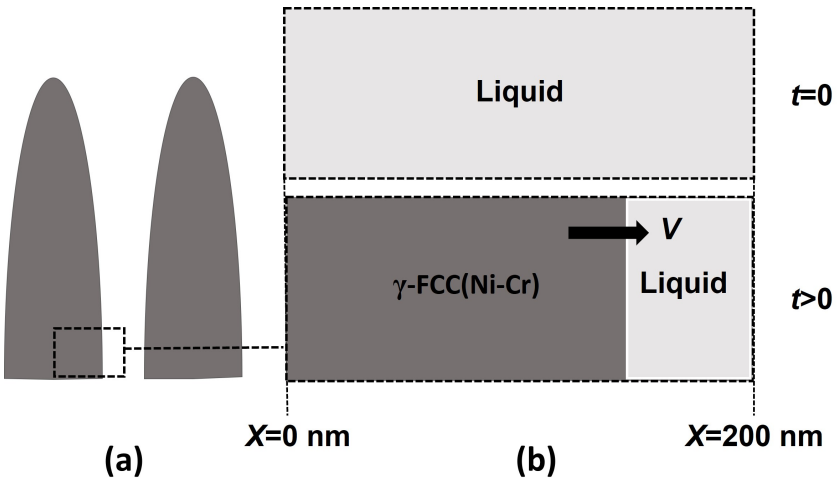

Figure 4.1: Schematic of a) two adjacent primary dendrite arms, and b) the corresponding 1-D simulation domain of the interdendritic region at $t = 0$ and t>0 for the left-most primary dendrite arm.

4.3 Experimental Results

4.3.1 Microstructure Characterization

Figure 4.2a shows an optical micrograph of the single-track as-built LPBF sample; the hump represents the transverse cross-section of deposited single-track protruding above the substrate. Figure 4.2b depicts an Inverse Pole Figure (IPF) Z images of same cross-section as Figure 4.2a; the melt pool boundary is shown with the white dashed line. As can be seen, the columnar grains appear to have the same orientation as the substrate, providing evidence of epitaxial growth towards the center of the deposit. The epitaxial growth is a result of partial melting of the substrate while the elongated morphology is a result of the high thermal gradient and localized directional heat extraction at the edge of the melt pool. The IPF Z image also demonstrates that columnar grain growth from the melt pool boundary to the center of the melt pool is the dominant growth mechanism. During the melt pool's solidification a Columnar to Equiaxed Transition (CET) may occur and as a result equiaxed grains nucleate ahead of the columnar front due to a drop in the thermal gradient. The specific thermal gradient and solidification rate enabling CET strongly depends on alloy composition [11,12,13]. Figure 4.2b does not show equiaxed grains, meaning that the thermal and compositional conditions within the melt pool were not favorable for the CET transition to occur.

Figures 4.3 shows the HAADF-STEM micrograph of a LPBF built IN625 grain having a matrix $< 101 >$ crystallographic orientation relative to the melt pool's XZ plane. The location of the grain within the melt pool is shown by the black dashed rectangle in Figure 4.2b. The gray area indicates the primary arms, whereas the white

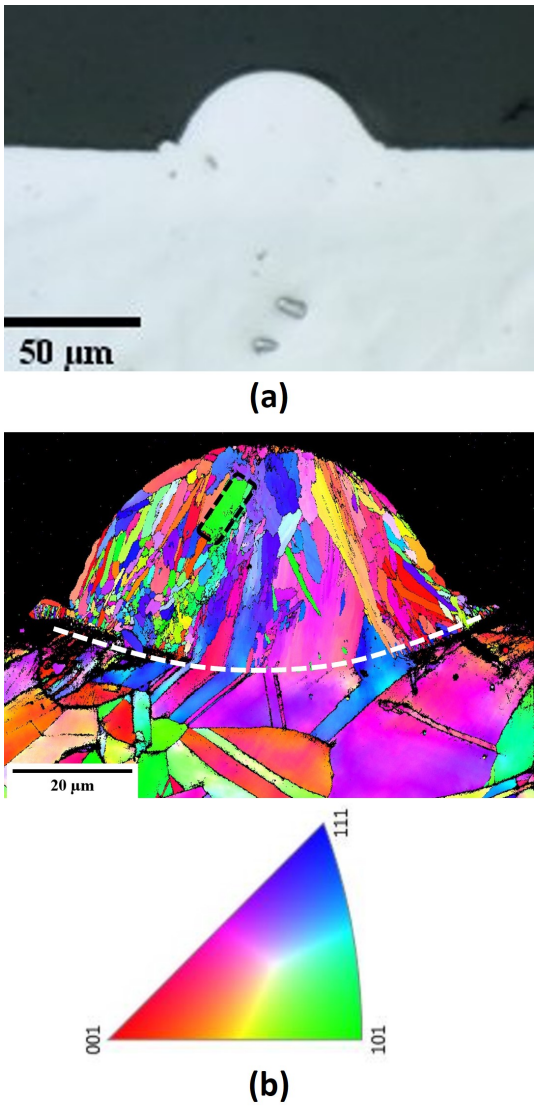

Figure 4.2: (a) OM transverse cross-sectional view, and (b) EBSD-IPF Z image of the single-track IN625 in the as-built condition. With white dashed line representing the melt pool boundary.

area shows the interdendritic region. As shown, the microstructure consists of mostly cell-like primary dendrite arms. Such microstructure is known as cellular/dendritic since the specific solidification and thermal conditions during LPBF create dendritic morphology but without secondary arms. Thus the microstructure appears cellular.

From the line intercept method, the PDAS was estimated to be 0.4 μm.

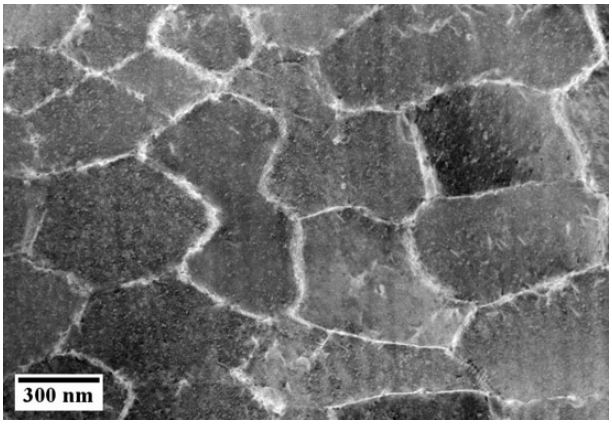

Figure 4.3: HAADF-STEM image of a single-track LPBF-built IN625. The grain is oriented transverse to the build direction, with a zone axis closely parallel to $[101]_{\gamma}$.

Figure 4.4a shows another HAADF-STEM micrograph of the primary dendritic structure, this time containing precipitate-like features mainly within the interdendritic region. Examples of these features are shown by black arrows. The microstructure is further magnified in Figure 4.4b, and examined via STEM-EDS in Figures 4.4c and 4.4d. As can be seen, the EDS maps clearly identify both the interdendritic region and precipitate-like nanoparticles as being rich in Nb.

To further quantify the composition variation traversing the interdendritic region and precipitate-like nanoparticles, Figures 4.5a and 4.5b show STEM-EDS scans across lines 1 and 2 shown in Figure 4.4b. As can be seen, a homogeneous distribution of Cr ($\approx$ 21 wt.%) is observed in both interdendritic and Nb-rich regions. However, the amount of Nb increases significantly in the interdendritic region and the precipitate-like nanoparticle as compared to the bulk value of 3.8 wt.%, reaching $\approx$11 wt.% and $\approx$ 22 wt.%, respectively.

Although it would appear from Figures 4.4b and 4.5b that line 2, with such a high

amount of Nb, contains a Nb-rich precipitate, which precipitate is it? Figure 4.6 shows a Ni-Nb isopleth section of the Ni-Nb-Cr-Fe-Mo-C-Si-Mn-Co-Al-Ti-S phase diagram. In this calculation, the initial composition of powder was utilized. As can be seen, NbC, δ-Ni_3Nb, and Laves can form via $L \rightarrow \gamma + \text{NbC}$; $L \rightarrow \gamma + \delta$; and $L \rightarrow \gamma + \text{Laves}$ eutectic reactions respectively. The first occurs with [Nb]>3 wt.%, while the second and third occur with [Nb]>10 wt.% and [Nb]>22 wt.%. However, other precipitates can also form including the metastable γ''-Ni_3Nb and thus a definitive identification can only be made via crystallographic investigation.

Figures 4.7a, 4.7b, and 4.7c present three HAADF-STEM micrographs showing three potential precipitates sites and 4.7d, 4.7e, and 4.7f depict their corresponding Fast Fourier Transform (FFT) diagrams. In d the green and blue circles represent the matrix γ phase and the γ''-Ni_3Nb precipitate; in e the red circles represent the NbC precipitates; in f the light blue and yellow circles both represent the Laves phase [39]. Thus, the FFT diagrams identify the presence of γ''-Ni_3Nb, NbC, and Laves precipitates within the interdendritic region of the LPBF-built IN625 alloy. No other precipitates were detected in our HAADF-STEM analysis.

4.4 Thermodynamic simulation results

Figure 4.8a and 4.8b respectively present the Scheil-Gulliver phase evolution with temperature in IN625 during solidification as well as the segregation of all alloying elements in the γ phase during the solidification sequence. As can be seen, this simulation predicts the formation of NbC, σ, and γ''-Ni_3Nb precipitates within the γ phase. The simulation also predicts that while all solute elements become segregated, the majority of the segregation occurs within the last 10% solidified γ. The highest

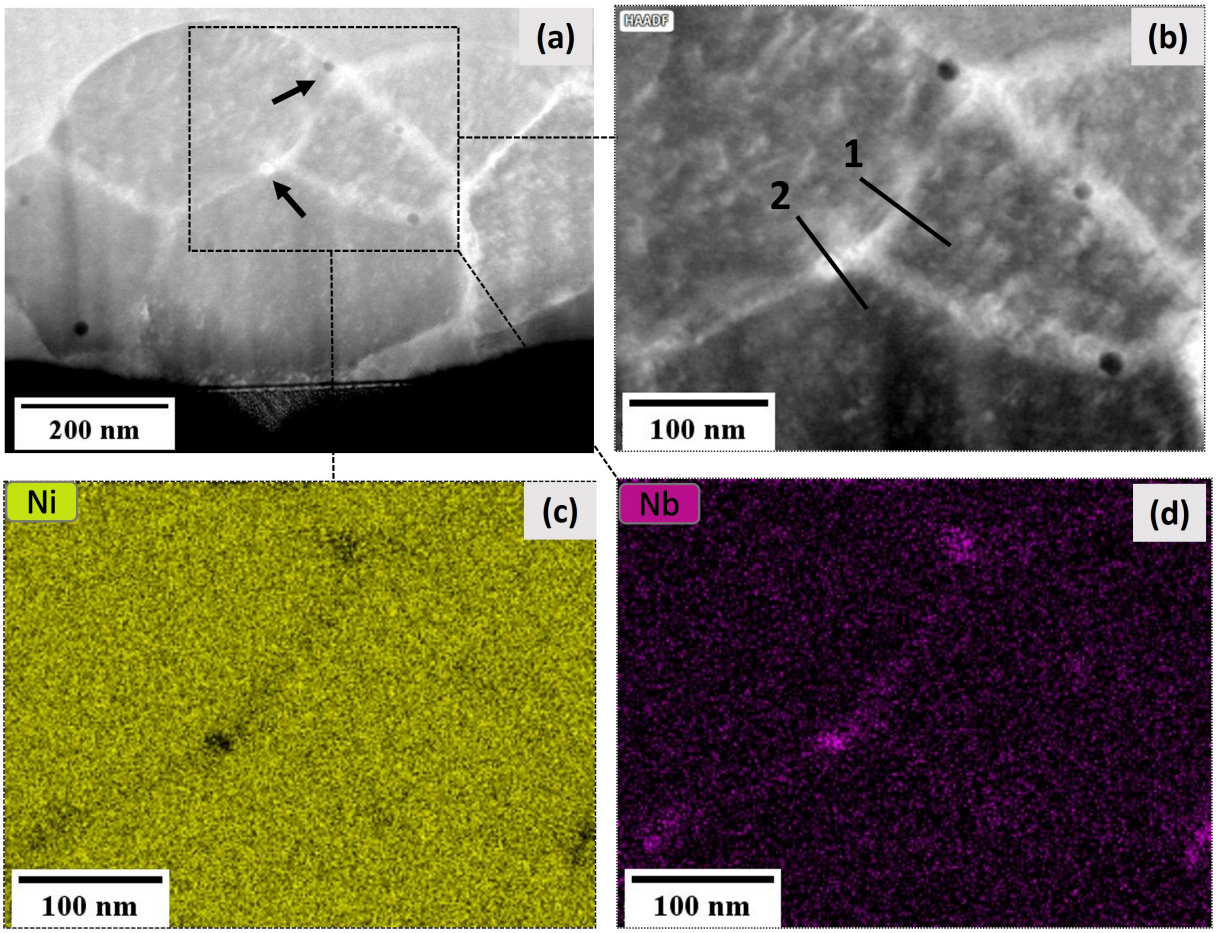

Figure 4.4: (a) HAADF-STEM image from the grain with a matrix < 101 > crystallographic orientation. The black arrows identify the potential precipitate sites within the interdendritic region. (b) Magnified HAADF-STEM view of the interdendritic region. Composition line scans 1 and 2 are provided in Figure 4.5. (c,d) Corresponding STEM-EDS map of Ni and Nb for Figure 4.4(b).

degree of segregation occurs for C (700%), Mn (281%), Si (250%), Nb (242%), Ti (122%), and Mo (68%). Concurrently, Cr (-5%), Co (-36%), Fe (-47%), and Al (-53%) inversely segregate out of the γ phase. the γ phase is depleted of C at the end of the solidification due to the formation of NbC precipitate.

Figure 4.9 shows the microsegregation profile within γ as a function of distance from the dendrite core calculated with DICTRA for Cr, Mo, Nb, Fe, C elements.

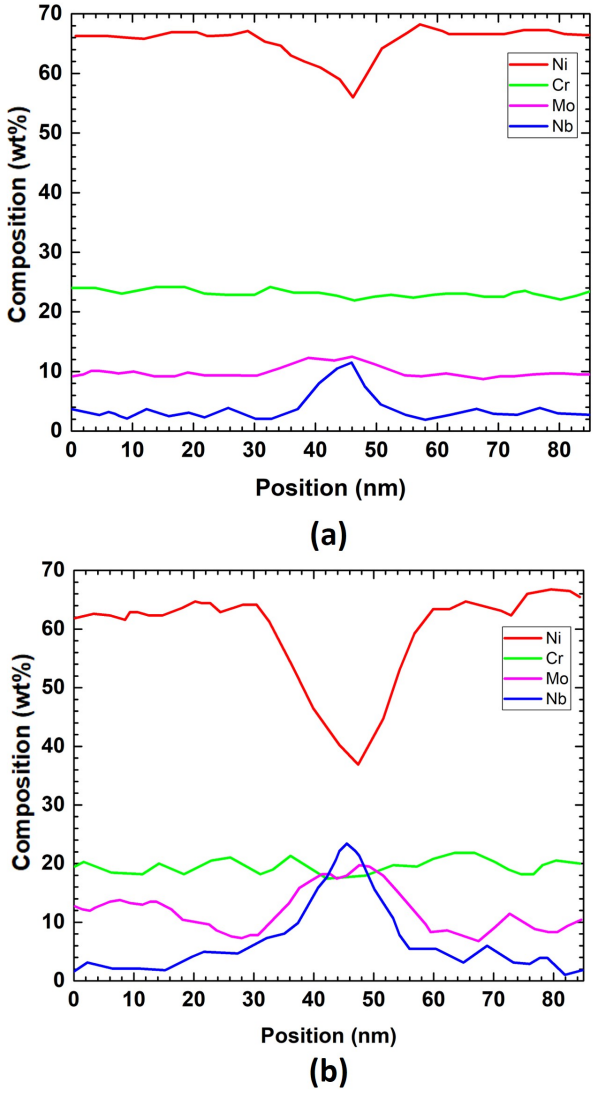

Figure 4.5: (a) STEM-EDS line scan traversing the a) interdendritic region (line1). (b) precipitate-like region (line2) in Figure 4.4b.

As can be seen, microsegregation patterns are qualitatively similar findings to the Scheil-Gulliver simulation, Figure 4.8b but considerably more microsegregation is predicted to have occurred. This is likely because the DICTRA simulation is limited to segregation within the γ phase; no other phases are allowed to form.

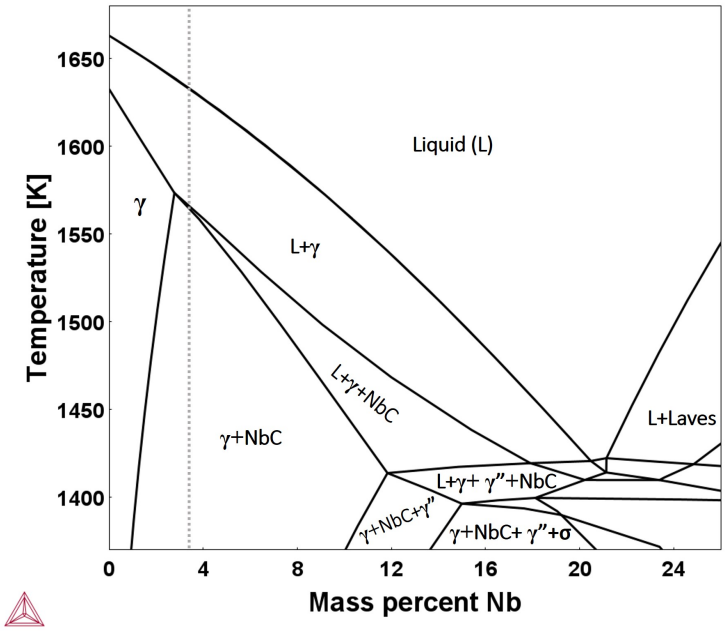

Figure 4.6: Ni-Nb isopleth section of the Ni-Nb-Cr-Fe-Mo-C-Si-Mn-Co-Al-Ti-S phase diagram for the 20.8Cr-0.72Fe-8.3Mo-0.02C-0.13Si-0.03Mn-0.18Co-0.28Al-0.35Ti (wt.%) alloy. All potential phases other than L, γ, γ'', NbC, σ, M_2C, M_6C, and $M_{23}C_6$ were suppressed.

4.5 Discussion

Heat treatment is an important step after building an additively manufactured part. This post-processing stage improves the part's properties by releasing internal stresses and removing microstructure heterogeneity. Heat treatment may also lead to the formation of new precipitates or help grow the as-built precipitates thus modifying mechanical properties. Understanding which precipitates exist in the microstructure of as-LPBF-built components as well as the development of elemental microsegregation will enable an improved post-build heat treatment process to be created.

The solidification microstructure of as-LPBF-built IN625 mainly contains columnar γ primary dendrites with the average width of 0.4 μm. Some precipitates have

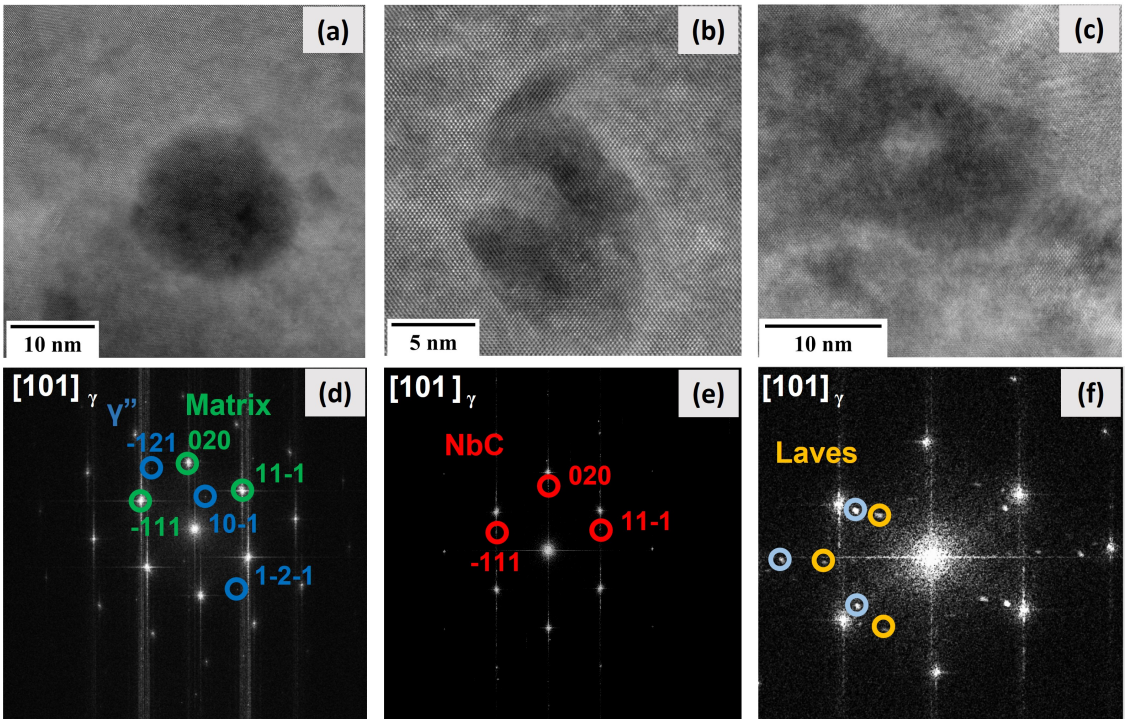

Figure 4.7: (a-c) High-resolution HAADF-STEM images of potential precipitates from Figure 4.4. (d-f) Corresponding FFT diagrams for each potential precipitate site.

also been detected in the interdendritic region. Generally, the PDAS value is dependent on the laser power, scan speed, and laser beam size. Low laser power, small beam size, and high scan velocity lead to the formation of a small melt pool and, consequently, smaller PDAS during the LPBF process compared to conventional welding. The PDAS for both single-track and multi-layer LPBF has been estimated in some studies and reported in the range of 0.2 μm to 1 μm [40,41,26,29]. Gan et al. [42] showed that the nonuniform distribution of G and V within the melt pool during single-track laser melting led to the primary dendrite arm spacing varying from 0.23 μm to 0.79 μm. In another study, Keller et al. [28] used the same processing parameters as Gan and estimated the PDAS as 1 μm in a multi-layer LPBF part. Overall,

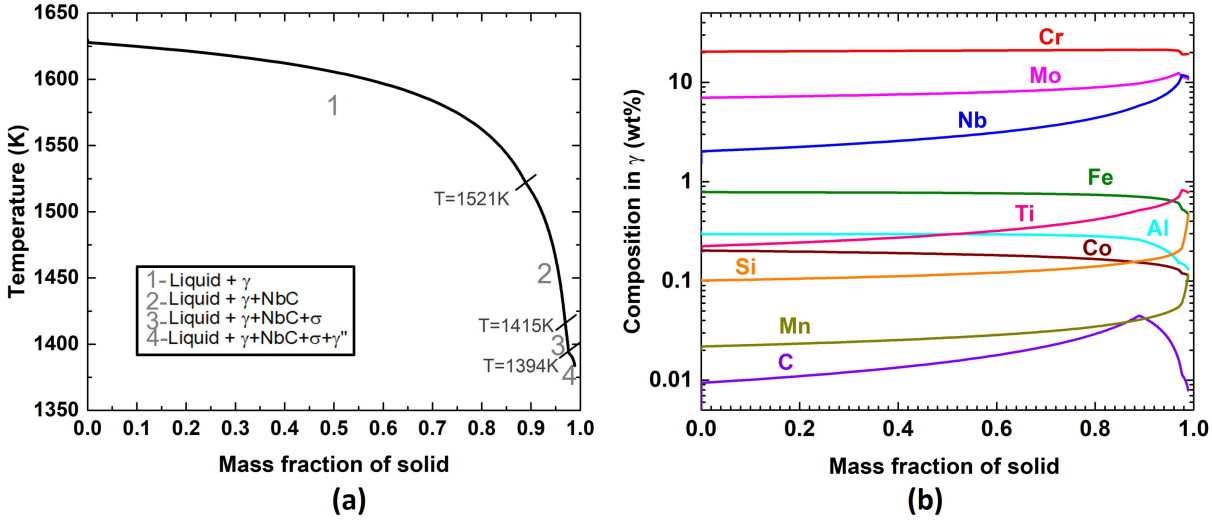

Figure 4.8: Scheil-Gulliver simulation of the phase transformation from $L \rightarrow \gamma + \mathrm{NbC} + \sigma + \gamma''$ using the full alloy composition. (a) Fraction solid evolution as a function of temperature. (b) Elemental microsegregation as a function of fraction γ during solidification.

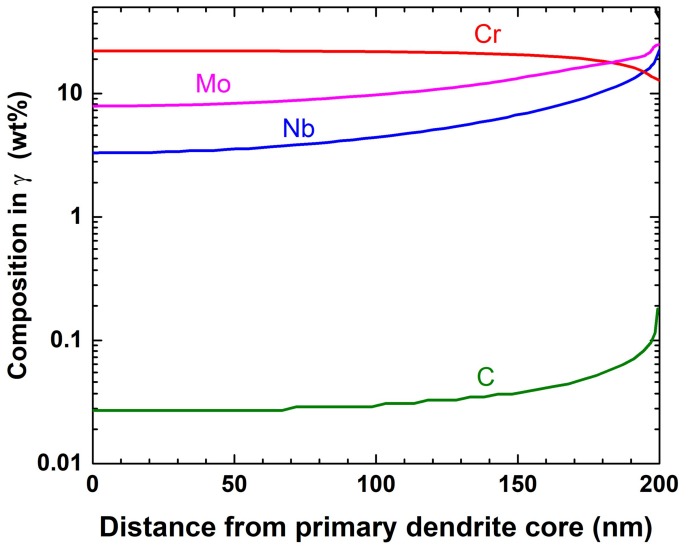

Figure 4.9: Dictra simulation of elemental microsegregation in γ as a function of distance from the dendrite core during solidification for the reduced alloy composition.

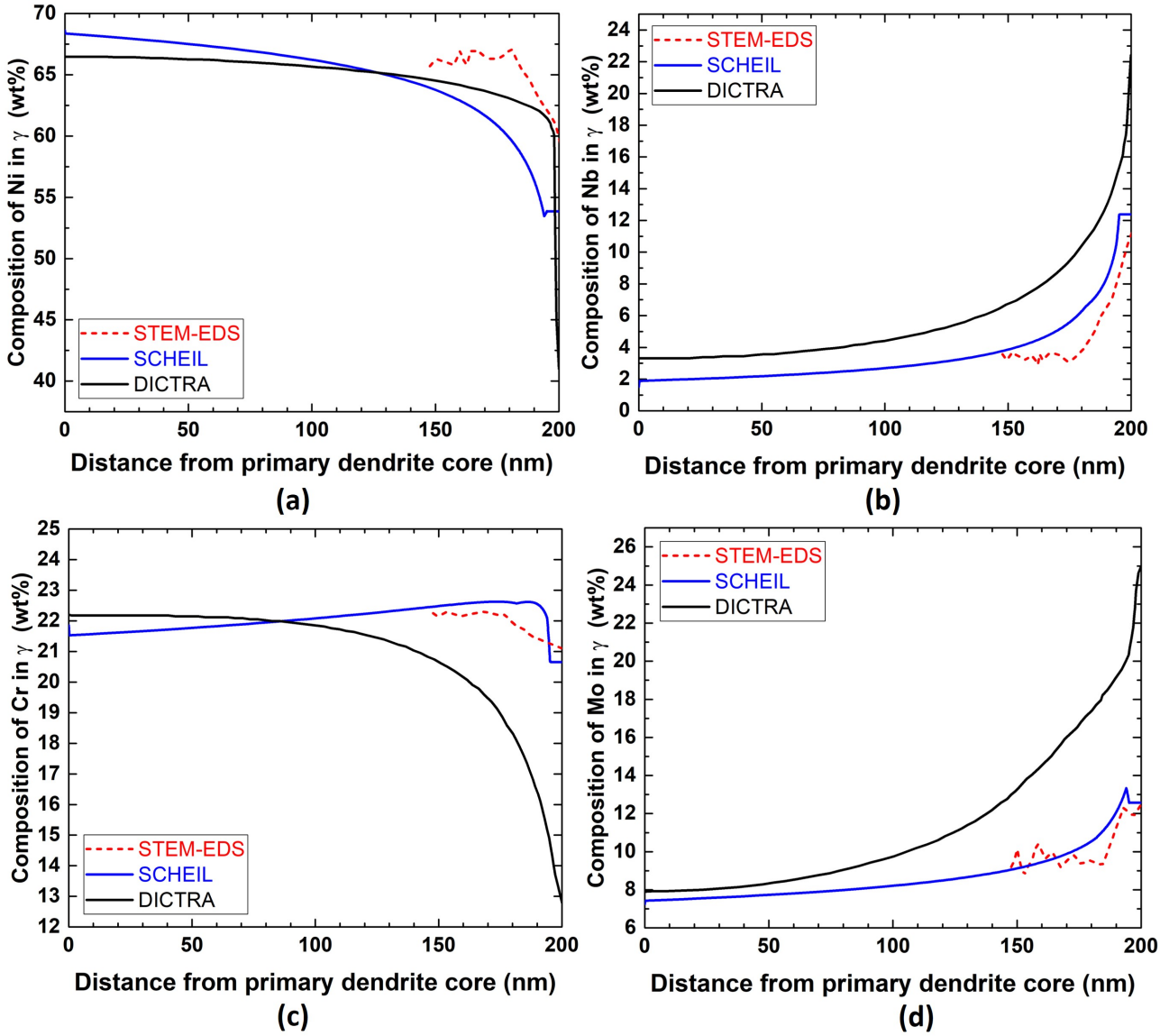

Figure 4.10: Comparison of the Scheil-Gulliver (with solute trapping), DICTRA, and STEM-EDS microsegregation profiles for a)Ni b)Nb, c)Cr, and d)Mo within the γ phase as a function of distance from the dendrite core.

our measurements fall within the range identified by Gan. Although our measurement is below the value measured by Keller, that was for a multi-layer LPBF part where the multiple passes would result in dendrite coarsening.

As shown through Figures 4.4, 4.5, and 4.7, Nb-rich precipitate-like regions were detected by HAADF-STEM and STEM-EDS in the as-built IN625 microstructure. To identify which precipitates were present, HAADF-STEM analysis was carried out on a couple of the potential precipitate sites. The resulting FFT diagrams, identified these regions as γ'', Laves, and NbC. The formation of precipitates during rapid solidification was also been investigated via Scheil-Gulliver simulation, considering solute trapping. As was shown in Fig.4.8, precipitation of only the γ'' and NbC phases, and not the Laves phase, was predicted to occur at the end of the solidification.

To further investigate the sequence of precipitate formation, the driving force for phase nucleation, δG_{nuc}, for all precipitates at the end of IN625 solidification is given in Table 4.1. The temperature, T, and composition, C, of the last 1 wt.% liquid was estimated using the Scheil-Gulliver simulation as T=1383 K and C= C (0.14), Fe(0.37), Nb(18.5), Mo(13.2), Cr(16.6), Ti(0.9), Al(0.058), Si(0.87), Mn(0.13), Co(0.094), Ni (balance) (wt.%). Only precipitates having negative δG_{nuc} are premissible, and are thus listed in the table.

Based on the driving force values, the formation of a given precipitate becomes more thermodynamically favourable towards the end of solidification due to microsegregation of Mo, Nb, and C in the interdendritic region. From a thermodynamic point of view, ignoring the kinetic and interfacial energy contributions, it is expected for NbC to nucleate first followed by the formation of M_2C, δ, M_6C, μ, and γ''. Interestingly, although Scheil-Gulliver with solute trapping predicted the formation of the σ phase, it does not have a negative free energy and thus is not thermodynamically favorable in the last 1 wt.% solidified liquid. Since δ and γ'' have a similar chemical formula but different crystal structures, there will also be a competition in which

of these precipitates form earlier in the interdendritic region. Although the last solidified liquid is more favourable for the formation of δ than γ'' thermodynamically, only γ'' was observed in the LPBF microstructure. M_2C, μ, and M_6C were also not seen in the as-LPBF-built IN625 microstructure in spite of them also having negative δG_{nuc} values. Of course, even a thermodynamically stable precipitate may not be able to nucleate at specific thermal and compositional conditions due to the kinetic considerations [43].

Table 4.1: Driving forces for the formation of permissible precipitates from the last 1wt% solidified IN625 liquid (T=1383 K and C= C (0.14), Fe(0.37), Nb(18.5), Mo(13.2), Cr(16.6), Ti(0.9), Al(0.058), Si(0.87), Mn(0.13), Co(0.094), Ni (balance) (wt.%) as calculated by the Thermo-Calc CALPHAD software.

Last 1 wt.% solidified liquid (1383 K)	
Precipitate	ΔG_{nuc} (j mole^{-1})
NbC	-10896
M_2C	-5447
δ	-544
M_6C	-521
μ	-498
γ"	-29

Figure 4.10 compares the amount of microsegregation of all alloying elements in the γ phase during the rapid solidification as calculated via Scheil-Gulliver with solute trapping, DICTRA, and experimentally-measured via STEM-EDS to carry out a deep study of microsegregation during rapid solidification. For this comparison, the x-axis of the Scheil-Gulliver simulation shown in Figure 4.8b was scaled to the half-length of the measured primary dendrite arm spacing. As can be seen in the figure,

all three methods confirm the occurrence of microsegregation in γ towards the interdendritic region. A very good agreement is observed between the Scheil-Gulliver simulation with solute trapping and the STEM-EDS microsegregation measurements, for throughout the dendrite core, for all elements microsegregation. DICTRA, however, greatly overestimates the microsegregation within the interdendritic region towards the end of solidification.

The simulation results shown in Figure 4.10 are a result of the inherent assumptions made for both Scheil-Gulliver and the DICTRA simulations. The first reason for having an overestimation of microsegregation by DICTRA is that this model assumes an equilibrium solid/liquid interface during the whole solidification process. When the solidification rate is low, the solid/liquid interfacial compositions remain near equilibrium condition. However for rapid solidification processes like LPBF, the solid/liquid interface is far from the equilibrium. The solute trapping effect during non-equilibrium solidification will greatly affect the partition coefficient and compositional undercooling thus changing the microsegregational pattern and the formation of supersaturated solid solution and the secondary meta-stable phases [44]. The second reason for having overestimation of microsegregation by DICTRA is that the formation of secondary solid precipitates and the curvature effect during dendritic solidification have been ignored for the sake of simplicity [45]. However, in the Scheil-Gulliver simulation, the effect of the solute trapping and also the formation of the secondary solid phases are inherently considered. Thus, with inclusion of the solute trapping phenomenon, this model is able to greatly reproduce microsegregation during LPBF processing.

The repeated thermal cycles during the multi-layer LPBF process can lead to

partial remelting, reheating, and resolidification in the solidified layers, which may change local composition, microsegregation patterns, and phase transformation conditions. Previous microstructural studies [28,15] of as-built multi-layer IN625 showed that the remelted material solidifies following a similar pattern as the initial solidified liquid. Although solid-state diffusion would occur in the reheated area to affect the microsegregation pattern, we feel that the impact is not terribly significant due to the short holding time at high temperatures. As shown in Figure 4.11, the single-track microsegregation levels for Nb and Mo measured in this study are higher than multi-layer LPBF microsegregation levels measured by Zhang et al. [15] for similar processing conditions. Thus, it seems clear that homogenization of Mo and Nb occurs as a result of multi-layer LPBF processing, with greater extent of homogenization for Nb than Mo.

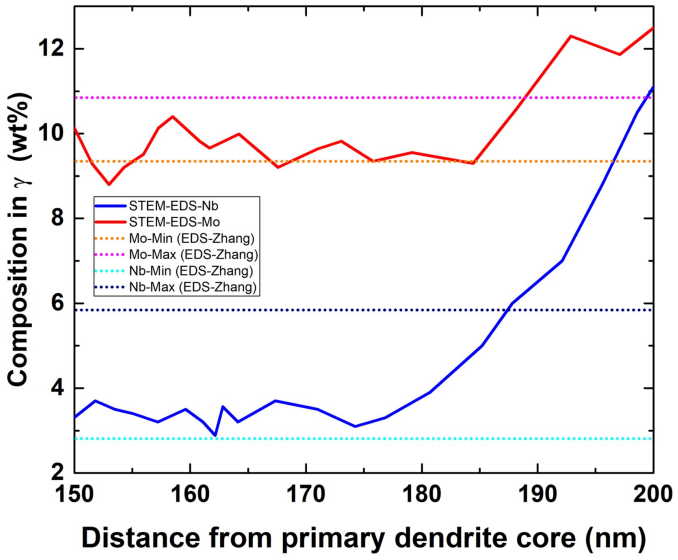

Figure 4.11: Comparison of the Mo and Nb microsegregation in the IN625 γ phase as measured in our single track LPBF experiments and by [15] using EDS in a multi-layer/multi-track build.

The results from this study help to better understand the microstructural evolution during rapid solidification of IN625. These findings can be used as a base guideline to study the phase transformations in multi-layer LPBF parts and to design an appropriate post heat treatment process to achieve the desired properties.

4.6 Conclusions

In this study the as-LPBF-built microstructure of IN625 has been investigated utilizing optical and electron microscopy, along with computational thermodynamics, to better understand solidification microstructure, microsegregation patterns, and the formation of the precipitates. The findings of this study can be summarized as follows:

- The formation of the precipitates was investigated by HAADF-STEM analysis and by calculation of nucleation driving force for the formation of the potential precipitates from the last solidified liquid. Highly concentrated Nb areas were identified via HAADF-STEM analysis as γ'', Laves, and NbC precipitates. Scheil-Gulliver solidification simulation, with solute trapping, also confirmed the formation of γ'' and NbC but not Laves at the end of rapid solidification.

- Although the driving force analysis indicated that all of NbC, M2C, μ, δ, M6C, and γ'' precipitates possibly nucleate from the last solidified liquid, the M2C, μ, δ and M6C precipitates were not observed in the as-LPBF-built microstructure. This is because they may not be able to nucleate at specific thermal and compositional conditions due to having non-equilibrium solid/liquid interface and the occurrence of solute trapping.

- STEM-EDS, Scheil-Gulliver, and DICTRA simulation analyses confirmed the

occurrence of significant microsegregation with the highest level of segregation towards the interdendritic region.

- The Scheil-Gulliver with solute trapping simulation provided a good match to the experimentally-obtained microsegregation patterns, while the DICTRA simulation significantly overestimated the extent of microsegregation.

4.7 Acknowledgement

The authors acknowledge funding from the National Sciences and Engineering Council of Canada, and experimental support from McMaster's Additive Manufacturing Research Group. Electron microscopy was carried out at the Canadian Centre for Electron Microscopy (CCEM), a national facility supported by the Canada Foundation for Innovation under the Major Science Initiatives program, NSERC and McMaster University. HY would like to thank Chris Butcher from CCEM for his help with the EBSD sample.

References

[1] V. Shankar, K. B. S. Rao, and S. Mannan, "Microstructure and mechanical properties of inconel 625 superalloy," *Journal of nuclear materials*, vol. 288, no. 2-3, pp. 222–232, 2001.

[2] M. Shaikh, M. Ahmad, K. Shoaib, J. Akhter, and M. Iqbal, "Precipitation hardening in inconel* 625," *Materials science and technology*, vol. 16, no. 2, pp. 129–132, 2000.

[3] G. Dey, S. Albert, D. Srivastava, M. Sundararaman, and P. Mukhopadhyay, "Microstructural studies on rapidly solidified inconel 625," *Materials Science and Engineering: A*, vol. 119, pp. 175–184, 1989.

[4] T. DebRoy, H. Wei, J. Zuback, T. Mukherjee, J. Elmer, J. Milewski, A. M. Beese, A. d. Wilson-Heid, A. De, and W. Zhang, "Additive manufacturing of metallic components–process, structure and properties," *Progress in Materials Science*, vol. 92, pp. 112–224, 2018.

[5] W. J. Sames, F. List, S. Pannala, R. R. Dehoff, and S. S. Babu, "The metallurgy and processing science of metal additive manufacturing," *International Materials Reviews*, vol. 61, no. 5, pp. 315–360, 2016.

[6] W. E. Frazier, "Metal additive manufacturing: a review," *Journal of Materials Engineering and Performance*, vol. 23, no. 6, pp. 1917–1928, 2014.

[7] C. Farrar, *The alloy tree: A guide to low-alloy steels, stainless steels and nickel-base alloys*. Elsevier, 2004.

[8] P. Mohammadpour and A. Phillion, "Solidification microstructure selection maps for laser powder bed fusion of multicomponent alloys," in *IOP Conference Series: Materials Science and Engineering*, vol. 861, p. 012005, IOP Publishing, 2020.

[9] C. Li, R. White, X. Fang, M. Weaver, and Y. Guo, "Microstructure evolution characteristics of inconel 625 alloy from selective laser melting to heat treatment," *Materials Science and Engineering: A*, vol. 705, pp. 20–31, 2017.

[10] A. Kreitcberg, V. Brailovski, and S. Turenne, "Effect of heat treatment and hot isostatic pressing on the microstructure and mechanical properties of inconel 625

alloy processed by laser powder bed fusion," *Materials Science and Engineering: A*, vol. 689, pp. 1–10, 2017.

[11] J. Hunt, "Steady state columnar and equiaxed growth of dendrites and eutectic," *Materials science and engineering*, vol. 65, no. 1, pp. 75–83, 1984.

[12] M. Gäumann, R. Trivedi, and W. Kurz, "Nucleation ahead of the advancing interface in directional solidification," *Materials Science and Engineering: A*, vol. 226, pp. 763–769, 1997.

[13] P. Mohammadpour, A. Plotkowski, and A. B. Phillion, "Revisiting solidification microstructure selection maps in the frame of additive manufacturing," *Additive Manufacturing*, vol. 31, p. 100936, 2020.

[14] B. Sundman, H. Lukas, and S. Fries, *Computational thermodynamics: the Calphad method*. Cambridge university press New York, 2007.

[15] F. Zhang, L. E. Levine, A. J. Allen, M. R. Stoudt, G. Lindwall, E. A. Lass, M. E. Williams, Y. Idell, and C. E. Campbell, "Effect of heat treatment on the microstructural evolution of a nickel-based superalloy additive-manufactured by laser powder bed fusion," *Acta materialia*, vol. 152, pp. 200–214, 2018.

[16] J. P. Oliveira, A. LaLonde, and J. Ma, "Processing parameters in laser powder bed fusion metal additive manufacturing," *Materials & Design*, vol. 193, p. 108762, 2020.

[17] Y.-J. Liang, X. Cheng, J. Li, and H.-M. Wang, "Microstructural control during laser additive manufacturing of single-crystal nickel-base superalloys: New

processing–microstructure maps involving powder feeding," *Materials & Design*, vol. 130, pp. 197–207, 2017.

[18] N. Chen, H. A. Khan, Z. Wan, J. Lippert, H. Sun, S.-L. Shang, Z.-K. Liu, and J. Li, "Microstructural characteristics and crack formation in additively manufactured bimetal material of 316l stainless steel and inconel 625," *Additive Manufacturing*, vol. 32, p. 101037, 2020.

[19] L. E. Murr, S. M. Gaytan, D. A. Ramirez, E. Martinez, J. Hernandez, K. N. Amato, P. W. Shindo, F. R. Medina, and R. B. Wicker, "Metal fabrication by additive manufacturing using laser and electron beam melting technologies," *Journal of Materials Science & Technology*, vol. 28, no. 1, pp. 1–14, 2012.

[20] F. Xu, Y. Lv, Y. Liu, F. Shu, P. He, and B. Xu, "Microstructural evolution and mechanical properties of inconel 625 alloy during pulsed plasma arc deposition process," *Journal of Materials Science & Technology*, vol. 29, no. 5, pp. 480–488, 2013.

[21] K. Gola, B. Dubiel, and I. Kalemba-Rec, "Microstructural changes in inconel 625 alloy fabricated by laser-based powder bed fusion process and subjected to high-temperature annealing," *Journal of Materials Engineering and Performance*, pp. 1–7, 2020.

[22] M. Sundararaman, L. Kumar, G. E. Prasad, P. Mukhopadhyay, and S. Banerjee, "Precipitation of an intermetallic phase with pt 2 mo-type structure in alloy 625," *Metallurgical and Materials Transactions A*, vol. 30, no. 1, pp. 41–52, 1999.

[23] G. Smith and S. Patel, "The role of niobium in wrought precipitation-hardened nickel-base alloys," *Superalloys*, vol. 718, pp. 625–706, 2005.

[24] G. Dinda, A. Dasgupta, and J. Mazumder, "Laser aided direct metal deposition of inconel 625 superalloy: Microstructural evolution and thermal stability," *Materials Science and Engineering: A*, vol. 509, no. 1-2, pp. 98–104, 2009.

[25] K. Amato, J. Hernandez, L. Murr, E. Martinez, S. Gaytan, P. Shindo, and S. Collins, "Comparison of microstructures and properties for a ni-base superalloy (alloy 625) fabricated by electron and laser beam melting," *Journal of Materials Science Research*, vol. 1, no. 2, p. 3, 2012.

[26] S. Li, Q. Wei, Y. Shi, Z. Zhu, and D. Zhang, "Microstructure characteristics of inconel 625 superalloy manufactured by selective laser melting," *Journal of Materials Science & Technology*, vol. 31, no. 9, pp. 946–952, 2015.

[27] A. Kreitcberg, V. Brailovski, and S. Turenne, "Elevated temperature mechanical behavior of in625 alloy processed by laser powder-bed fusion," *Materials Science and Engineering: A*, vol. 700, pp. 540–553, 2017.

[28] T. Keller, G. Lindwall, S. Ghosh, L. Ma, B. M. Lane, F. Zhang, U. R. Kattner, E. A. Lass, J. C. Heigel, Y. Idell, *et al.*, "Application of finite element, phase-field, and calphad-based methods to additive manufacturing of ni-based superalloys," *Acta materialia*, vol. 139, pp. 244–253, 2017.

[29] G. Marchese, M. Lorusso, S. Parizia, E. Bassini, J.-W. Lee, F. Calignano, D. Manfredi, M. Terner, H.-U. Hong, D. Ugues, *et al.*, "Influence of heat treatments on microstructure evolution and mechanical properties of inconel 625

processed by laser powder bed fusion," *Materials Science and Engineering: A*, vol. 729, pp. 64–75, 2018.

[30] X. Hu, Z. Xue, G. Zhao, J. Yun, D. Shi, and X. Yang, "Laser welding of a selective laser melted ni-base superalloy: Microstructure and high temperature mechanical property," *Materials Science and Engineering: A*, vol. 745, pp. 335–345, 2019.

[31] E. A. Lass, M. R. Stoudt, M. E. Williams, M. B. Katz, L. E. Levine, T. Q. Phan, T. H. Gnaeupel-Herold, and D. S. Ng, "Formation of the ni 3 nb δ-phase in stress-relieved inconel 625 produced via laser powder-bed fusion additive manufacturing," *Metallurgical and Materials Transactions A*, vol. 48, no. 11, pp. 5547–5558, 2017.

[32] E. A. Lass, M. R. Stoudt, M. B. Katz, and M. E. Williams, "Precipitation and dissolution of δ and γ'' during heat treatment of a laser powder-bed fusion produced ni-based superalloy," *Scripta Materialia*, vol. 154, pp. 83–86, 2018.

[33] B. Dubiel and J. Sieniawski, "Precipitates in additively manufactured inconel 625 superalloy," *Materials*, vol. 12, no. 7, p. 1144, 2019.

[34] G. Lindwall, C. Campbell, E. Lass, F. Zhang, M. R. Stoudt, A. J. Allen, and L. E. Levine, "Simulation of ttt curves for additively manufactured inconel 625," *Metallurgical and Materials Transactions A*, vol. 50, no. 1, pp. 457–467, 2019.

[35] J.-O. Andersson, T. Helander, L. Höglund, P. Shi, and B. Sundman, "Thermo-calc & dictra, computational tools for materials science," *Calphad*, vol. 26, no. 2, pp. 273–312, 2002.

[36] H. Larsson, "A model for 1d multiphase moving phase boundary simulations under local equilibrium conditions," *Calphad*, vol. 47, pp. 1–8, 2014.

[37] "Thermo-calc software version2021b, TCNI10 and MOBNI5 nickel/ni-alloys database," 2021.

[38] H. Rezaeifar and M. Elbestawi, "Porosity formation mitigation in laser powder bed fusion process using a control approach," *Optics & Laser Technology*, vol. 147, p. 107611, 2022.

[39] R. Krakow, D. N. Johnstone, A. S. Eggeman, D. Hünert, M. C. Hardy, C. M. Rae, and P. A. Midgley, "On the crystallography and composition of topologically close-packed phases in ati 718plus®," *Acta Materialia*, vol. 130, pp. 271–280, 2017.

[40] C. Li, Y. Guo, and J. Zhao, "Interfacial phenomena and characteristics between the deposited material and substrate in selective laser melting inconel 625," *Journal of Materials Processing Technology*, vol. 243, pp. 269–281, 2017.

[41] S. Ghosh, L. Ma, L. E. Levine, R. E. Ricker, M. R. Stoudt, J. C. Heigel, and J. E. Guyer, "Single-track melt-pool measurements and microstructures in inconel 625," *Jom*, vol. 70, no. 6, pp. 1011–1016, 2018.

[42] Z. Gan, Y. Lian, S. E. Lin, K. K. Jones, W. K. Liu, and G. J. Wagner, "Benchmark study of thermal behavior, surface topography, and dendritic microstructure in selective laser melting of inconel 625," *Integrating Materials and Manufacturing Innovation*, vol. 8, no. 2, pp. 178–193, 2019.

[43] G. Ghosh and G. Olson, "Precipitation of paraequilibrium cementite: Experiments, and thermodynamic and kinetic modeling," *Acta Materialia*, vol. 50, no. 8, pp. 2099–2119, 2002.

[44] T. Pinomaa and N. Provatas, "Quantitative phase field modeling of solute trapping and continuous growth kinetics in quasi-rapid solidification," *Acta Materialia*, vol. 168, pp. 167–177, 2019.

[45] W. . Kurz, B. Giovanola, and R. Trivedi, "Theory of microstructural development during rapid solidification," *Acta Metallurgica*, vol. 34, no. 5, pp. 823–830, 1986.

Chapter 5

Evaluation of Microstructure Heterogeneity in INCONEL 625 Thin-wall Fabricated by Laser Powder Bed Fusion Additive Manufacturing

Complete Citation: P. Mohammadpour, H. Yuan, Z. Li, A.B. Phillion, "Evaluation of Microstructure Heterogeneity in INCONEL 625 Thin-wall Fabricated by Laser Powder Bed Fusion Additive Manufacturing," *to be Submitted to Acta Materiala*.

Evaluation of Microstructure Heterogeneity in INCONEL 625 Thin-wall Fabricated by Laser Powder Bed Fusion Additive Manufacturing

P. Mohammadpour[a], H. Yuan[b], Z.Li[a] A.B. Phillion[a]

[a]*Department of Materials Science and Engineering, McMaster University, Hamilton, Canada*

[b]*Canadian Centre for Electron Microscopy, McMaster University, Hamilton, Canada*

Abstract: Spatial Microstructure heterogeneity is ubiquitous in as-built Laser Powder Bed Fusion (LPBF) parts due to the unique thermal and solidification conditions during Additive Manufacturing (AM) process. This multi-scale microstructure heterogeneity leads to variability in the mechanical properties of LPBF parts. This study aims to complete the process-structure-properties relationship loop in an as-built multi-layer LPBF IN625. Towards this end, numerical thermal simulation, scanning electron microscopy (SEM), Scanning Transmission Electron Microscopy (STEM) with Energy-Dispersive X-ray Spectroscopy (EDS), High-Angle Annular Dark-Field Scanning Transmission Electron Microscopy (HAADF-STEM), Electron Backscatter Diffraction (EBSD), nanohardness test, Scheil solidification model, and DIffusion-Controlled TRAnsformations (DICTRA) methods were utilized to investigate the spatial heterogeneity in terms of grain size and morphology, Primary Dendrite Arm Spacing (PDAS), microsegregation pattern, precipitation, and hardness along the build direction. It was found that the as-built microstructure contains mostly columnar (Nickel–Chromium) dendrites growing epitaxially along the build direction. The hardness was found to be minimal in the middle and maximal in the bottom layers of

the build's height. Smaller melt pools, grains, and PDAS and higher thermal gradients and cooling rates were observed in the bottom layers compared to the top layers. Microsegregation patterns in multiple layers were also simulated using Dictra, and the results were compared with the STEM-EDS results. Different precipitates, including γ', γ'', δ, laves, NbC, Ni_2Al, and Al_4C_3, were observed along the build direction from the bottom to the top layers of the LPBF part. The mechanism for the formation of these precipitates and the dependency of the mechanical properties on the type and distribution of these precipitates were discussed.

Keyword: Inconel625, Additive manufacturing, Laser Powder Bed Fusion (LPBF), Microsegregation, Precipitation, Microstructure heterogeneity

5.1 Introduction

Inconel 625 (IN625) is a solid solution- and precipitation-hardenable nickel-based superalloy, strengthened by the solid-solution hardening effect of chromium, niobium, and molybdenum and through the formation of precipitates within nickel-chromium (γ) matrix. The precipitation hardening in this alloy is mainly due to the formation of γ'' (Ni_3Nb) metastable phase. Moreover, some precipitates such as laves (Ni_2(Cr,Mo)), MC carbides, and (on rare occasions) δ-Ni_3Nb have been observed in the microstructure of this alloy [1,2,3,4,5,6,7]. These microstructural features, in addition to this alloy's excellent high-temperature corrosion and oxidation properties, and weldability, make this alloy a common choice for aerospace, automotive, and marine applications, as well as a potential choice for Additive Manufacturing (AM) [8,9].

Laser Powder Bed Fusion (LPBF), an AM method, is a layered fabrication method to produce cost-efficient near-net shape 3-D parts with complex geometries through laser melting of metal powders [10,11]. The IN625 microstructure formed during laser melting is different from that of a wrought material as a result of the nonequilibrium solidification conditions and the unique microsegregation patterns of the alloying elements within the as-solidified microstructure [12,13,14].

The strengthening of the IN625 alloy depends on the local composition and the morphology of available precipitates. A small change in the quantity of alloying elements may lead to a significant variation in the precipitation behavior and, consequently, the mechanical properties. Microstructural evolution under rapid solidification conditions and in the post-build heat-treatment has been investigated in some previous studies on LPBF IN625 [15,16,17,18,19,12,20,21,22]. Broadly, the results from these studies confirmed the formation of NbC, MoC, M_6C carbide, γ'' (Ni_3Nb),

δ-Ni_3Nb and laves precipitates after heat treatment of the LPBF part, but did not examine the as-solidified structure. Recently, Mohammadpour et al. [23] carried out a comprehensive study examining the microstructural evolution and precipitate formation in an as-built single-track LPBF IN625 using electron microscopy and the CALculation of PHAse Diagrams (CALPHAD) numerical approach. They detected NbC, γ'' (Ni_3Nb) and laves precipitates in the as-built IN625. Importantly for optimizing heat treatment, they also confirmed, both experimentally and via CALPHAD, that significant microsegregation towards the interdendritic region was occurring.

Although [23] provided an initial view of the as-LPBF-solidified IN625 microstructure, commercial application of LPBF contains layer-by-layer melting and rapid solidification of the metal powders during the multi-layer building. These repeated thermal cycles can lead to partial remelting, reheating, and resolidification of the solidified layers, which may change the local composition, microsegregation pattern, and thus the phase transformation conditions, and mechanical properties [24,11,25,26, 27]. The heterogeneity of mechanical properties and the correlation between microstructure and mechanical properties in a multi-layer as-built AM IN625 has only been discussed in a few of the previous studies. Fujia et al. [28] noted that the size and morphology of dendrites vary along the build direction in a Pulsed Plasma Arc Deposition (PPAD) part. Specifically, in comparison with the bottom part that contained dendrite arms, a coarser dendrite structure with classical secondary dendrite arms was observed in the upper part of the build. They have also observed the presence of fine laves precipitates in the bottom layers but a large number of γ'' precipitates in the upper layers. A higher hardness and tensile strength were seen in the bottom layers of the PPAD part, which was correlated to the smaller size of dendrites and

finer distribution of precipitates. In another study, Gola et al. [22] detected finer dendrites in regions of overlapping melt pools as compared to regions where this did not occur. This was attributed to the reheating effect during the multi-layer LPBF process. Wang et al. [26] used Neutron diffraction along with thermomechanical finite element modeling to demonstrate that the thermal history, residual stress, and elemental composition are location-dependent within IN625 walls fabricated by laser-based directed energy deposition (DED) AM. For example, the upper layers of the DED part experienced higher temperature causing the depletion of Cr via vaporization. They also showed that the repeated thermal cycling leads to a residual stress pileup.

The previous studies described above provided a comprehensive microstructural investigation of as-build IN625 PPAD and DED AM processes, i.e. conditions having a much larger melt pool and much lower cooling rates as compared to LPBF. To better understand the industrial potential of LPBF-produced IN625, it is necessary to better understand the correlation between the spatial variations in mechanical properties and the underlying microstructural heterogeneity of a multi-layer as-solidified LPBF part. In this study, modern electron microscopy techniques, nano-hardness testing, Scheil, DIffusion-Controlled TRAnsformations (DICTRA), and numerical thermal simulations were implemented to comprehensively characterize IN625 in the as-solidified condition produced via multi-layer LPBF.

5.2 Methods

5.2.1 Thin-wall LPBF Experiment and Characterization

A 20×1×6 mm^3 multi-layer LPBF part was built from IN625 powder using a Renishaw AM400 machine. The composition of the powder, given in Table 5.1, was measured via Inductively Coupled Plasma (ICP) atomic emission spectroscopy . The part was fabricated using a laser scanning speed (v_{lss}) of 800 mm/s, a power (p) of 195 W, a hatch spacing (H) of 100 μm, and a layer thickness (t) of 30 μm. The build geometry, build direction, and laser scanning direction are shown in Figure 5.1(a). Owing to the 6 mm wall height and the layer thickness of 30 μm, 200 layers were built. In the multi-layer LPBF process, it is essential to build the consecutive layers slightly differently to achieve a strong bond between the layers. Known as scan strategy rotation (SSR), it involves slightly rotating the path of the laser beam. In this study a commonly-used SSR value of 67° counterclockwise has been utilized.

Table 5.1: Chemical composition of IN625 measured by inductively coupled plasma atomic emission spectroscopy (ICP).

Element	C	Mn	Si	Cr	Co	Mo	Nb	Ti	Al	Fe	Cu	Ni
Composition (wt%)	0.02	<0.01	0.07	22.0	0.05	9.3	3.74	0.19	0.12	2.8	0.01	61.7

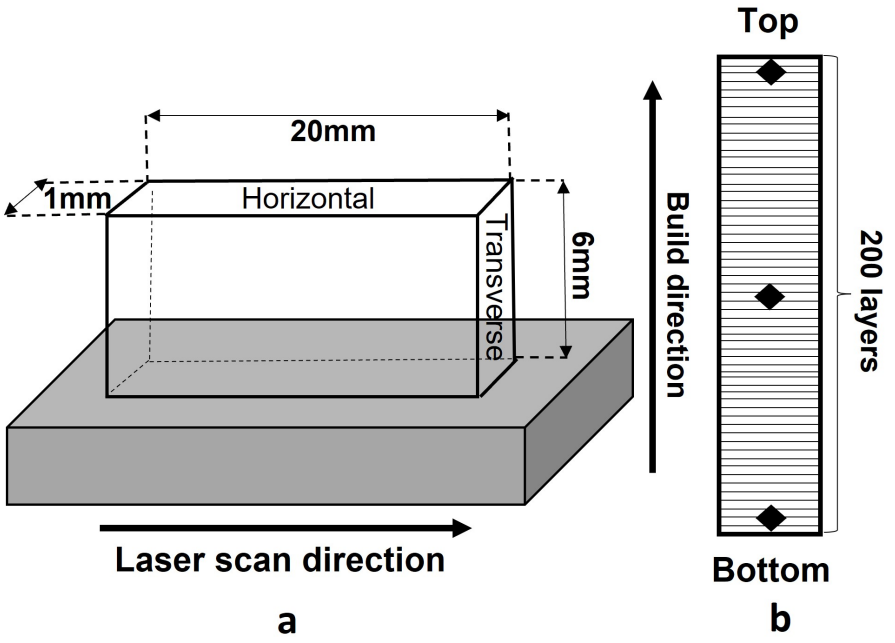

Figure 5.1: a) Schematic of the build geometry; b) Transverse cross-section of the multi-layer build. In (a), the planes Horizontal (perpendicular to the build direction, parallel to the laser scan direction), Longitudinal (parallel to the build direction, parallel to the laser scan direction), and Transverse (parallel to the build direction, perpendicular to the laser scan direction) are shown as indicated. In (b) the black diamonds indicate the approximate positions of the micrographs given in Figures 5.4 and 5.5.

Transverse, longitudinal, and horizontal cross-sections were then machined from the as-solidified part, and characterized in terms of grain morphology and melt-pool morphology. To further investigate the microstructure and mechanical heterogeneity along the build direction, the transverse cross-section was characterized in the bottom, middle, and top layers of the build (see Figure 5.1(b)) in terms of dendrite size, grain size and morphology, melt-pool size, microsegregation pattern, precipitation, and nanohardness using Optical Microscopy (OM), Scanning Electron Microscopy

(SEM), Electron Backscatter Diffraction (EBSD), High-Angle Annular Dark-Field-Scanning Transmission Electron Microscopy (HAADF-STEM), and Scanning Transmission Electron Microscopy-Energy-Dispersive X-ray Spectroscopy (STEM-EDS) analyses. The microscopy samples were mounted, polished to a 0.05 μm surface finish and then the polished samples were etched chemically in aqua regia (3 HCl: 1 HNO3) for 25 s. Nikon-ECLIPSE LV100ND and JEOL JSM-7000F SEM were used for OM and SEM microscopy. EBSD maps were acquired in a Thermo Scientific Helios G4 UXe Dual Beam Plasma-FIB using an Oxford Instruments Symmetry S2 camera at 20 kV and a step size of 0.5 μm. Three thin foils were then lifted out from the bottom, middle and top sections of the transverse cross-section from grains close to $< 101 >$ crystal orientation using the same PFIB. STEM specimens were cleaned with a Gatan low-energy Solarus plasma cleaner for 180 s just before the experiments. STEM-EDS was carried out using a ThermoFisher Scientific Talos F200X TEM microscope equipped with four in-column SDD super-X detectors operated at 200 kV. For HAADF-STEM imaging, a FEI Titan 80–300 cubed TEM was used at 200 kV with a semi-convergence angle of 19 mrad and a semi-collection angle of 64–200 mrad. Finally,the nano-hardness within the transverse cross-section along the build direction was measured using an Anton Paar NHT^3 nanoindenter machine with the maximum load of 50 mN. The hardness was measured at 27 different locations with 200 μm intervals along the build's height from the bottom to the top layers. It should be noted that the hardness at each point is the average of 4 measurements.

5.2.2 Thermodynamic and Thermal Simulations

Thermo-Calc v2021b, with the commercial NITC10 and MOBNI5 thermodynamic and mobility databases, was used to simulate the microsegregation of alloying elements in IN625 during the multi-layer LPBF process [29,30,31].

The initial solidification was simulated using Scheil-Gulliver to acquire the complete microsegregation pattern of all alloying elements including the precipitation of various secondary phases. The input composition matched the experimentally-determined composition of the powder (Table 5.1). Solute trapping is needed since, during rapid solidification, this phenomenon can occur within the γ phase of IN625 thus affecting the microsegregation patterns. The effect of solute trapping on the microsegregation profile was considered by including the solidification rate in the calculation via Thermo-Calc's new solute trapping algorithm. The solidification rate was estimated as $\approx$0.14 m/s, i.e. the product of the laser scan speed (0.8 m/s) and the scanning angle (80^{o}).

Note that in the Scheil simulations, the formation of δ, μ, ρ, σ, and β phases were suppressed. This assumption was shown to be valid in our previous study [23].

Finally, the re-heating phase of LPBF was simulated using the 1-D non-isothermal DICTRA kinetics diffusion model to calculate the final elemental microsegregation occurring within the bottom, middle, and top layers during LPBF processing. For the sake of simulation time, only Nb, Mo, Cr, C, and Ni elements were included in the DICTRA simulation.

DICTRA requires three inputs: the initial composition profile, the temperature evolution with time (assumed to be the same throughout in the domain), and the size of the domain. These inputs are described below:

- The initial composition profile was taken from the output of the Scheil solidification simulation.
- The temperature evolution with time was taken from a thermal simulation of the thin wall LPBF build process, described below.
- The size of the domain was assumed to be the distance from the core of γ to the interdendritic region, i.e. the one-half width of the Primary Dendrite Arm Spacing (PDAS). These distances, measure from the SEM images in Figures 5.4(c) were found to be 193 nm, 557 nm, and 762 nm, respectively, for the bottom, middle, and top layers.

In order to determine the temperature evolution for the DICTRA simulations at the bottom, middle, and top layers, a finite-element thermal simulation of the LPBF multi-layer build process was performed using the ABAQUS software. In this simulation, a Gaussian-distributed moving heat source was adopted, and temperature-dependent materials properties were considered. For the sake of the simulation time, only the deposition of 20 layers was simulated, and the temperature distribution in the substrate and the deposited layers is calculated. The dimensions of the substrate and deposited layer are set as 6 mm $\times$ 2mm $\times$ 0.6mm and 6 mm $\times$ 2mm $\times$ 0.03mm, respectively. As a high temperature gradient and cooling rate is expected during the AM process, a finer mesh is adopted where 57600($240 \times 80 \times 3$) elements are defined in each layer. During the LPBF process, the governing equation of the heat transfer process is formulated as [32]

$$\rho c_p \frac{\partial T(X,Y,Z,t)}{\partial t} = -\nabla \cdot \vec{q}(X,Y,Z,t) + Q(X,Y,Z,t) \tag{5.1}$$

where ρ is the density, c_p represents the specific heat capacity under constant pressure and T is the local temperature. Additionally, $\vec{q} = -k(T)\nabla T$ is the heat flux resulting from the temperature gradient, which represents the heat conduction, and $k(T)$ is the temperature-dependent heat conductivity of the material. Q represents the other heat sources, which includes heat input from lasers and the release of latent heat in this model, while convection and radiation are not considered.

In the present FEA model, the heat input from the laser beam is simulated by a Gaussian distributed moving heat source, written as [33]

$$q(x,y) = \frac{2\lambda P}{\pi r_0^2} exp\{\frac{-2[(x-x_0)^2 + (y-y_0)^2]}{r_0^2}\} \tag{5.2}$$

where λ is the absorptivity of the material, P is the laser power, r_0 is the laser radius and (x_0, y_0) is the position of the laser center varying with the time. To simulate the multi-layers printing process, an element death and birth method are applied, i.e. the deposited 20 layers are deactivated before the deposition process, and it will be activated one by one once the laser is going to scan through the layer.

Please note the following additional model assumptions. First, the SSR was assumed to be 0°. Second, a recoating time of 17 s was assumed to homogenize the heat between laser passes. The Finite Element Analysis (FEA) process parameters and material properties of this simulation are listed in table 5.2.

Table 5.2: Material properties for IN625 and the processing parameters [34,29]

Density (Kg/m^3)	8440
Specific heat (J/Kg K)	T<T$_s$, $0.2437T + 338.98$ T>T$_l$, 735
Conductivity (W/mK)	T<T$_s$, $0.015T + 5.331$ T>T$_l$, 30.5
Latent heat (KJ/Kg)	227
Solidus temperature (K)	1623
Liquidus temperature (K)	1348
Laser radius (mm.radius)	0.1
Waiting time between consecutive layers (s)	17
Layer thickness (μm)	30

5.3 Experimental Results

5.3.1 Microstructure Characterization and Nano-hardness

Figure 5.2 shows the 3-D OM and EBSD-Inverse Pole Figure (IPF) Z view of the middle layer of the build, i.e. the horizontal, longitudinal, and transverse images combined on one plot. As can be seen in (a), a fish-scale like melt-pool morphology is observed in the longitudinal and transverse cross-sections, while the melt track of the deposited laser is seen in the horizontal direction. The EBSD-IPF Z views, (b) shows clearly that columnar grain growth is dominant along the build direction, i.e. the longitudinal and transverse cross-sections. However, the "cut" columnar grains appear equiaxed in the horizontal plane.

Figure 5.3 shows the measured nano-hardness in the transverse cross-section along the build direction from the bottom to the top layer of the build. As can be seen, the maximum nano-hardness occurs at the bottom layer, 414 HV. Then, a decrease in hardness was observed until reaching a plateau in the central layers of the build

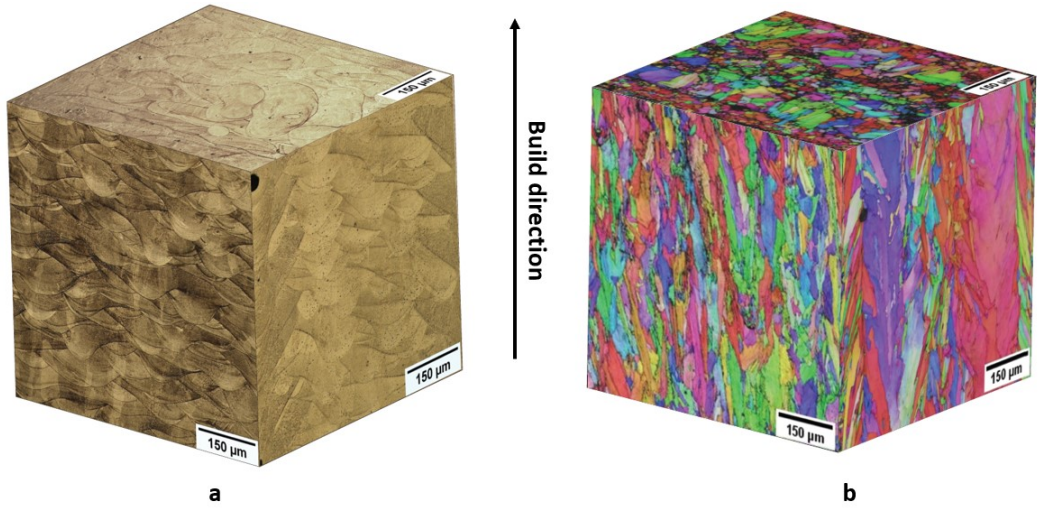

Figure 5.2: 3-D combined a)OM and b)EBSD-IPF Z views of the middle layer within the multi-layer LPBF IN625.

with an average hardness value of 350 HV. At the top of the build, the hardness is seen to increase again achieving a hardness of 410 HV in the top-most layer.

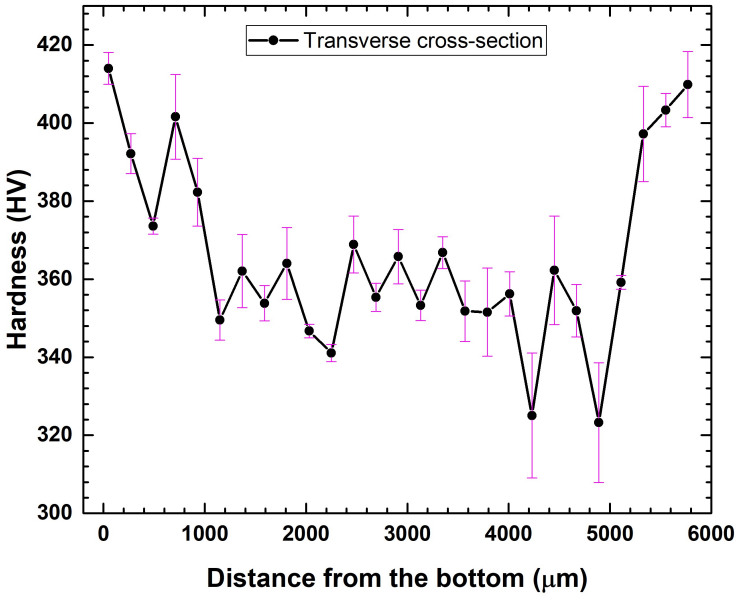

Figure 5.3: Nano-hardness in transverse cross-section along the build direction from the bottom to the top of the build.

Figure 5.4 shows the (a) EBSD-IPF Z, (b) OM, and (c) SEM images from the bottom, middle, and top layers inside the transverse cross-section of the build. As can be seen in (a), the microstructure mainly contains columnar grains growing epitaxially from the substrate (or previous layer) along the build direction. This is in contrast with wrought material where equiaxed grains would have formed [35]. Epitaxial growth results from partial remelting of the top layer during the deposition of the subsequent layers. A few tiny equiaxed grains are observed in the bottom layer, as well as at the edge of the build (in all three locations). Generally, a columnar to equiaxed transition (CET) occurs at a specific range of solidification rate and thermal gradient during solidification [14]. The edges of the build experience a lower solidification rate due to a lower heat transfer between the edges of the build and the surrounding unmelted powder as compared to the deposited layers. This is in favor of the occurrence of a CET. In addition, the grains in the inner region of the build are seen to be larger and show a lower level of misorientation as compared to the ones on the sides. This is because the heat transfer in the center of the thin-wall is largely uni-directional while the heat transfer towards the edges becomes multi-dimensional with cooling from the unmelted powder. From the line intercept method, the width of the elongated grains was estimated as 20.5 μm, 42.4 μm, and 54.8 μm in the bottom, middle, and top layers, respectively.

The morphology of the melt pools, Figure 5.4(b), looks similar in all three OM images, from the bottom to the top layers. The size of the melt pools in the bottom, middle, and top layers is seen to vary from 222 μm, 240 μm, to 298 μm, respectively. The size of the grains and melt pools increases from the bottom to the top of the build as a result of the heat accumulation and lower solidification rate in the top

compared to the bottom.

Finally, the γ dendritic structure is shown in Figure 5.4(c). As can be seen, cell-like dendrites exist in the bottom and middle layers, while the dendrites in the top layer appear to be more dendritic with long dendrites containing small secondary arms interspersed with cells. This is in contrast to our previous single-track LPBF study [23], and shows the importance of carrying out not only detailed research on single-track-produced material, but also multi-track builds. The PDAS in the bottom, middle, and top were estimated using the line intercept method as 0.39 μm, 1.12 μm, and 1.52 μm, respectively.

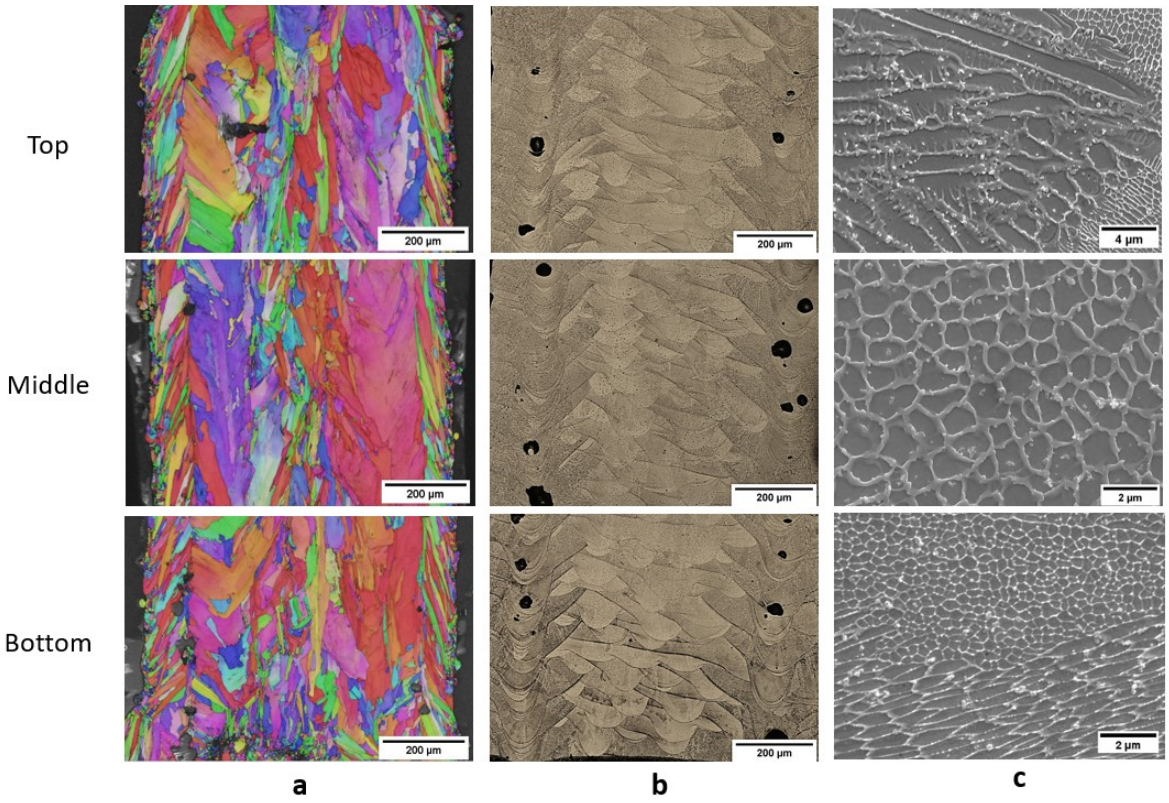

Figure 5.4: a) EBSD-IPF Z (grains), b) OM (melt pools), and c) SEM (dendrites) on the LPBF microstructure from the bottom, middle, and top Regions.

Figure 5.5 shows EDS maps for C, Nb, and Mo taken from STEM-HAADF images at the bottom, middle, and top layers of the multi-layer build. These EDS maps show that the interdendritic region is rich in Nb and Mo in all three regions. Furthermore, within the interdendritic region, some Nb- and C- rich precipitate-like particles (marked with white arrows) were also detected. The concentration of the precipitate-like particles is relatively similar in all layers examined.

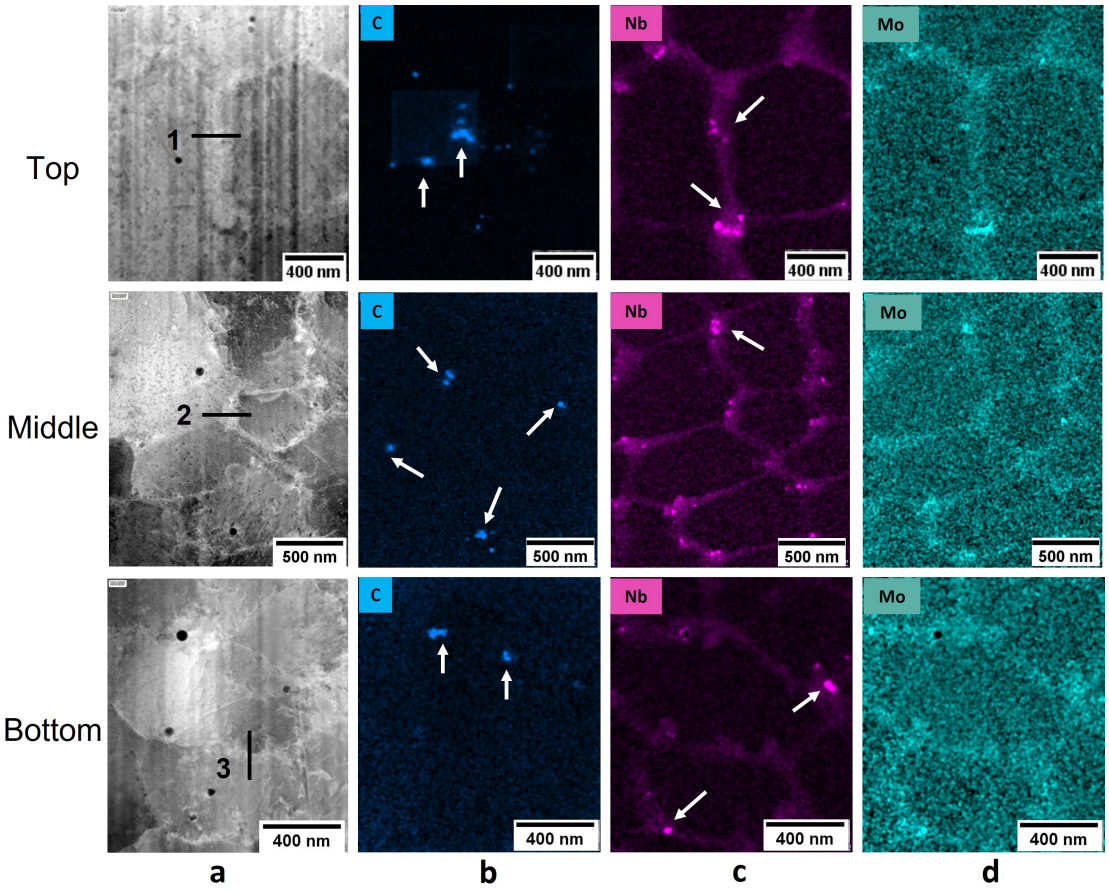

Figure 5.5: (a) STEM-HAADF images, along with STEM-EDS maps of (b)C, (c)Nb, and (d)Mo from the bottom, middle, and top layers.

Figure 5.6 shows the detailed variation in C, Nb, Cr, and Mo composition across the interdendritic regions. These line scans were performed on cross lines 1,2, and 3

shown in Figure 5.5. The 0 positions on the x-axes correspond to the center of the interdendritic region and the vertical dotted lines represent the edges of the interdendritic regions. As can be seen, both Nb and Mo show appreciable segregation, with the concentration of Nb and Mo being greatest at the center and then decreasing towards the edge of the interdendritic region, in all layers. In contrast, the distribution of C and Cr is relatively homogeneous. A much higher level of microsegregation is observed in the top layer as compared to the bottom layers. The degree of segregation of Nb, i.e. wt% (max)/ wt%Nb (as measured by ICP), is seen to increase from 1.6 at the the bottom layer to 2.6 at the top layer of the build.

To further investigate the precipitate-like particles found in Figure 5.5, HAADF-STEM analysis was implemented. Figures 5.7-5.9 show HAADF-STEM images of various precipitate-like particles in the bottom, middle, and top layers, along with their corresponding Fast Fourier Transform (FFT) diagrams. The FFT 5.7(e-h) analysis for the bottom layer (Figure 5.7(a-d)) confirmed the presence of γ', δ, laves, and Al_4C_3 precipitates within this inital region of the built part. However, the FFT analysis for the middle layers, Figure 5.8, showed γ', NbC, and Ni_2Al precipitates. Finally, the NbC precipitate was found in the top layer, Figure 5.9. Please note a few Nb-rich precipitate-like particles were found in the bottom and top layers whose FFT diagrams could not be detected. However, the STEM-EDS line scan traversing these precipitate-like particles showed that these particles might have been γ''. The HAADF-STEM images of these precipitates and the corresponding STEM-EDS line scans are presented in appendix.A (5.8).

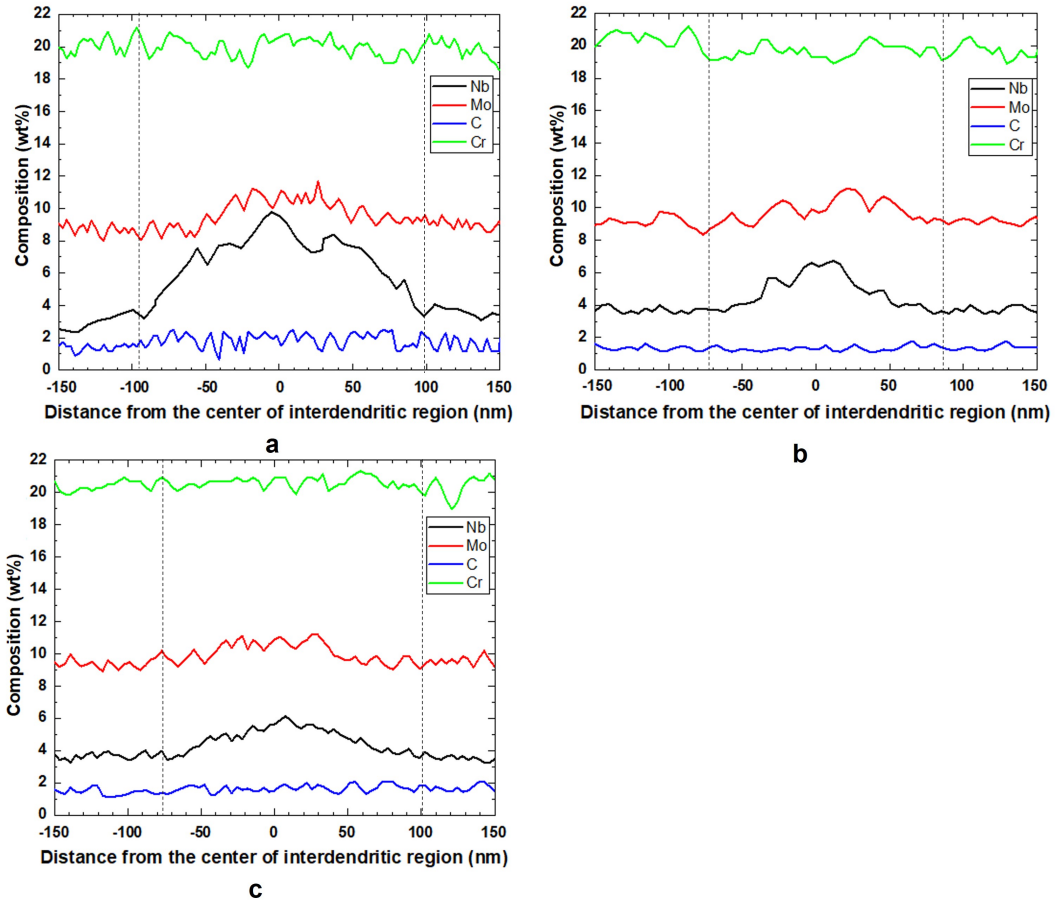

Figure 5.6: a) STEM-EDS Line scans traversing line a) 1, b) 2, and c) 3 in Figure 5.5a-top, middle, and bottom. Note that the 0 positions on the x-axes correspond to the center of the interdendritic region. Note also that the vertical dotted lines represent the edges of the interdendritic regions

5.4 Simulation Results

Figure 5.10 shows the (a) Scheil phase evolution and (b) microsegregation of all alloying elements in the matrix (γ phase) during the initial solidification of the bottom layer of the LPBF IN625 build. As can be seen, the Scheil simulation with solute trapping predicted the formation of NbC, γ'', and laves precipitates, as well as segregation of all alloying elements toward the end of the solidification. Note that Scheil

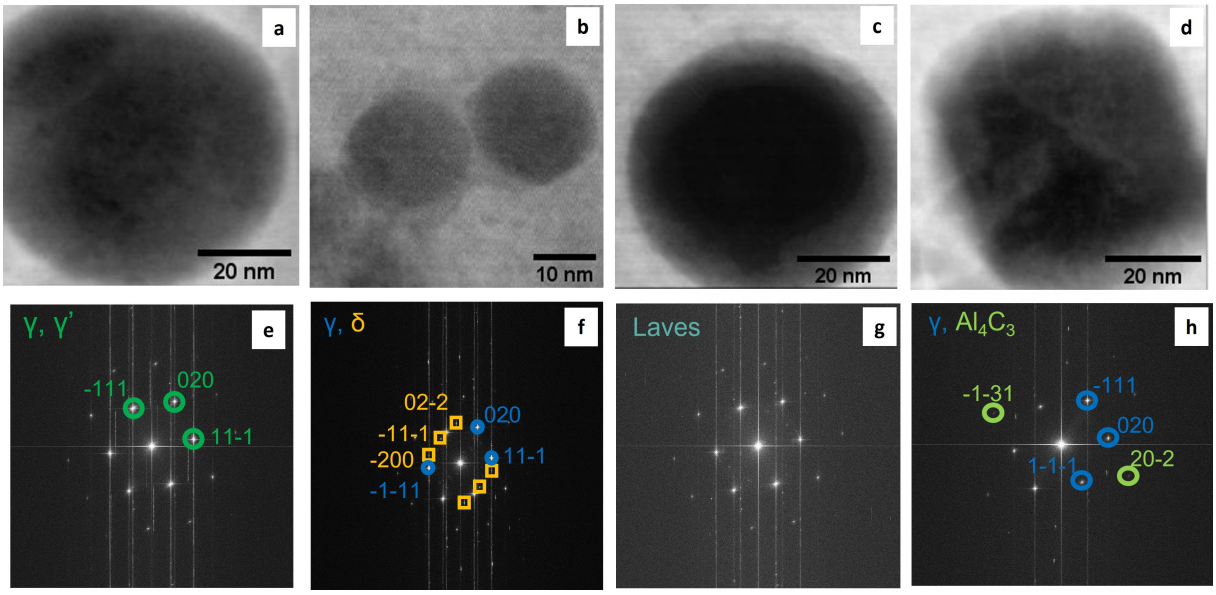

Figure 5.7: (a-d) HAADF-STEM images of the precipitates in the bottom layers of the build, (e-h) Corresponding FFT patterns.

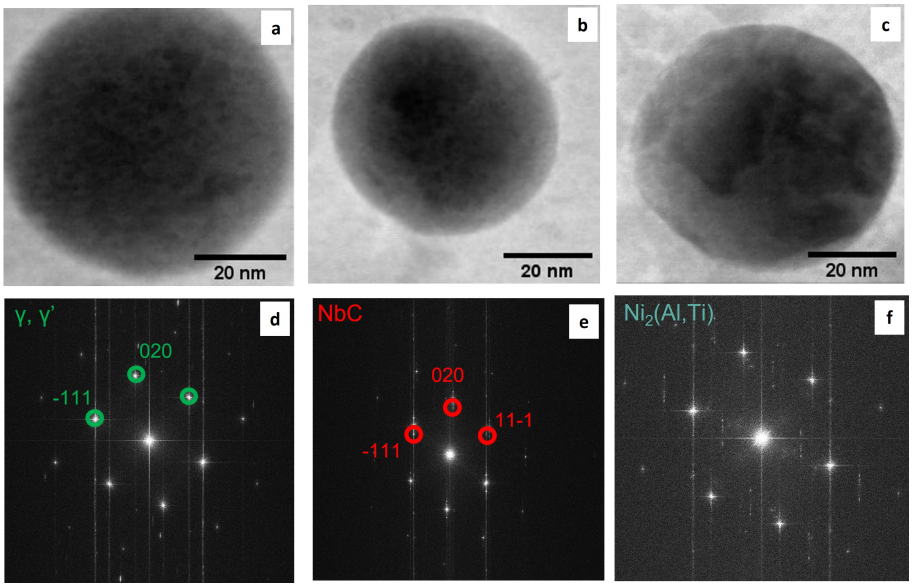

Figure 5.8: (a-c) HAADF-STEM images of the precipitates in the middle layers of the build, (d-f) Corresponding FFT patterns.

simulations for the middle and top layers was also carried out, but are not shown as they were nearly identical to the profiles given in Figure 5.10.

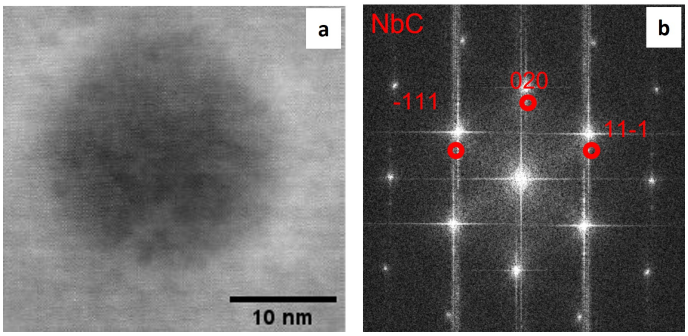

Figure 5.9: (a) HAADF-STEM images of the precipitate in the top layers of the build, (b) Corresponding FFT pattern.

The DICTRA simulation requires the alloying-element amounts at the end of the initial solidification as well as the thermal evolution history within the part during the LPBF process. The Scheil-predicted microsegregation profile of the alloying elements in the first solidified layer, shown in Figure 5.10(b), was used as an input in the DICTRA simulation.

Figure 5.11 (a) shows the thermal history of the bottom, middle, and top layers as predicted by the 20-layer FEA simulation. As can be seen, a deposited layer partially remelts during the deposition of the next layer but does not remelt during the deposition of any additional layers. Further, the bottom and middle layers are both reheated during the deposition, undergoing significant reheating for up to the next nine layers; with a descending reheating peak temperature as the deposition progresses. The solidification cooling rate and thermal gradient and well as the cooling rate after reheating process have been extracted from the 3D FEA model results at different nodal points in various layers. It should be noted that there were 3 elements in the thickness of each layer and the thermal data was extracted from the middle element. At each nodal point, The solidification cooling rate and the cooling rate after reheating were calculated via eq. 5.3 and 5.4, respectively,

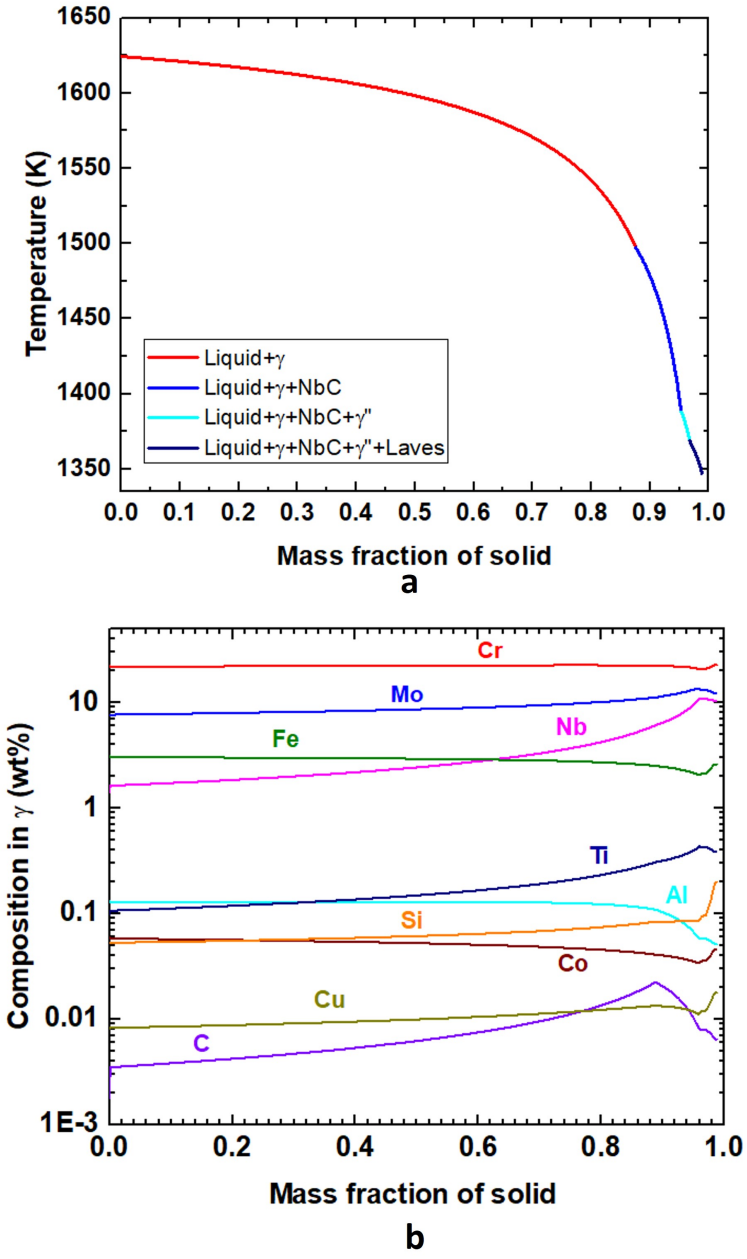

Figure 5.10: The a) Scheil phase evolution and b) microsegregation of all alloying elements in matrix (γ phase) during the solidification of the first layer of the LPBF IN625 build.

$$\frac{\partial T}{\partial t}(Solidification) = \left| \frac{T_S - T_L}{t_S - t_L} \right| \tag{5.3}$$

$$\frac{\partial T}{\partial t}(Reheating) = \left| \frac{T_{Peak} - T_{Min}}{t_{Peak} - t_{Min}} \right| \tag{5.4}$$

where T_L and T_S are liquidus and solidus temperatures reached at t_L and t_S. While T_{Peak} and T_{Min} are the peak and minimum temperatures in each reheating cycle captured at t_{Peak} and t_{Min}, respectively. The solidification thermal gradient at each nodal point was determined at t=t_l as

$$\frac{\partial T}{\partial Z} = \left| \frac{T_n - T_{n-1}}{Z_n - Z_{n-1}} \right| \tag{5.5}$$

where T_n and T_{n-1} are the temperatures at two adjacent nodes, Z_n and Z_{n-1}, along the Z direction.

Figure 5.11 (b) shows the corresponding cooling rate and peak temperature within the first (bottom) and tenth (middle) layers during the deposition of their seven subsequent layers. As can be seen, during the re-heating phase, the peak temperatures and cooling rates decrease significantly as the heat source moves further away from the initial layer.

Table 5.3 shows the corresponding thermal gradients, cooling rates, and peak temperatures predicted by these simulations to occur during solidification. From the bottom to the top, the thermal gradients and cooling rates are seen to decrease while the peak temperature is seen to increase due to the heat accumulation in the upper layers due to the multiple heat inputs and lower heat transfer into the substrate.

In the DICTRA simulations, for the bottom and middle layers, the temperature

Table 5.3: Thermal information during the initial solidification of the bottom, middle, and top layers estimated using FEA.

Layer number	**1(Bottom)**	**10(Middle)**	**20(Top)**
$\bar{G}$ **(K/m)**	11,113,178	10,788,469	10,046,267
$\dot{T}$ **(K/s)**	6,687,153	5,468,891	4,654,712
Peak Temp. (K)	4,822	5,052	5,094

evolution included all of the heat input during building of the additional nineteen and nine layers, respectively. For the top layer, the temperature evolution considered only the cooling curve during deposition of the last layer.

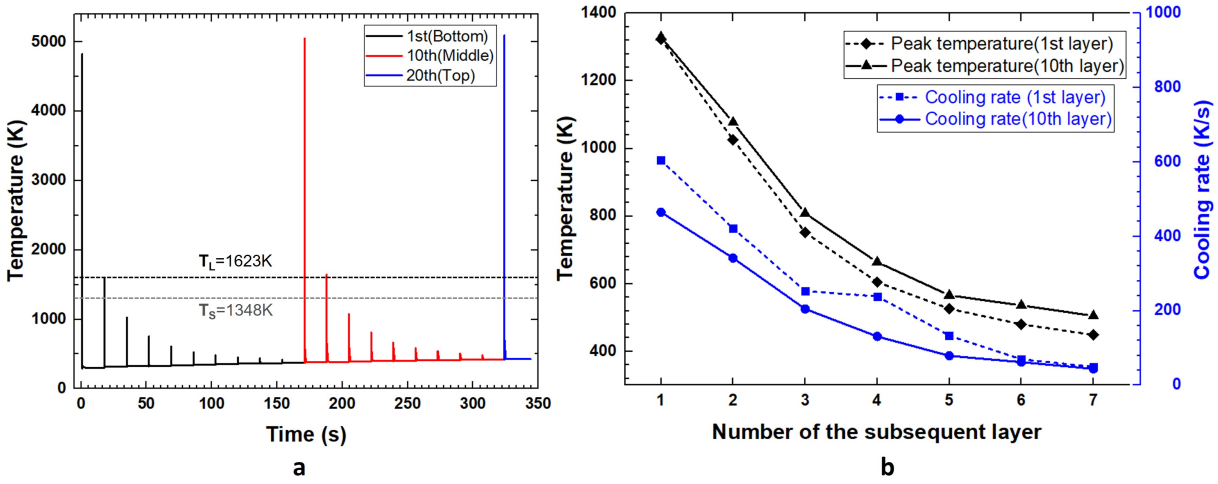

Figure 5.11: a) Thermal history of the bottom, middle, and top layers during the multi-layer LPBF build process for IN625. b) the cooling rate and peak temperature within the first (bottom) and tenth (middle) layer during the deposition of their seven subsequent layers

Figure 5.12 (a) and 5.12 (b) depict the DICTRA microsegregation profiles for Nb and Mo over the last 100 μm of solidification within the interdendritic region in the bottom, middle, and top layers in the transverse cross-section of the multi-layer LPBF IN625. As can be seen, Nb and Mo homogenized in the bottom layer due

to the repeated solid-state heating post-remelting during the multi-layer build. In contrast, the middle layer is seem to be less homogenized especially towards the end of solidification, while the top layer shows no homogenization.

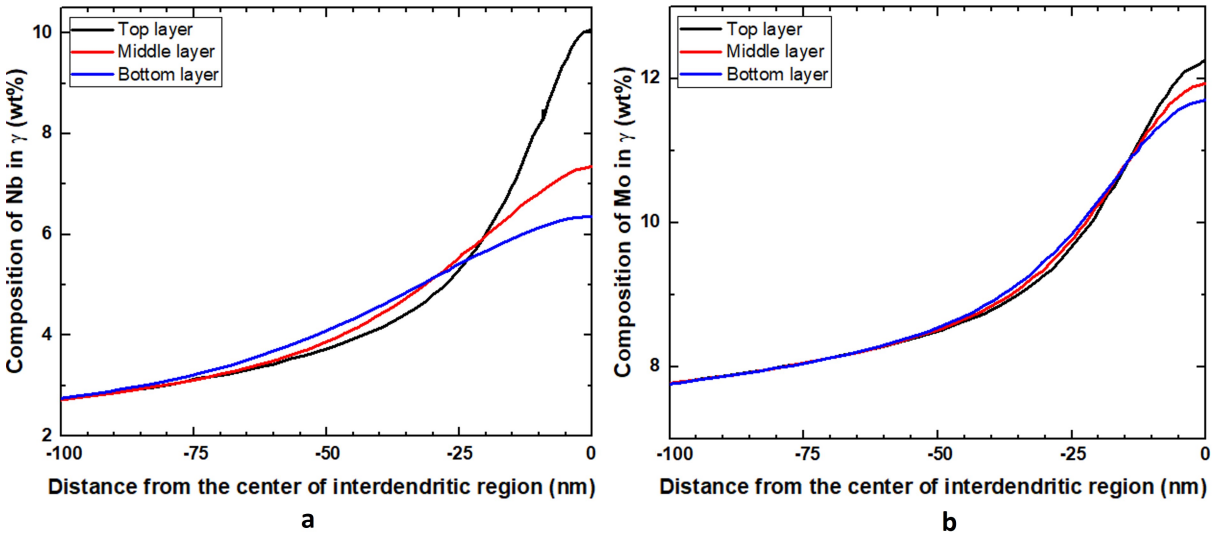

Figure 5.12: The DICTRA-predicted microsegregation profiles for a)Nb and b)Mo over the last 100 μm of solidification within the interdendritic region in the bottom, middle, and top layers.

5.5 Discussion

As shown in Figures 5.2 and 5.4, the as-built LPBF IN625 mainly consists of γ columnar grains that grew epitaxially from the substrate or the previous layer along the build direction, and opposite to heat flow. These appear as equiaxed grains in the transverse direction. An elongated grain may contain a couple of melt pools. Or one part of a single melt pool may fall partially into one grain and partially into another. The micrographs in Figure 5.4 (c) show clearly that the very fast solidification of the bottom (first) layer lead to the formation of cellular-like dendrites without secondary

arms, whereas secondary arms developed in the top (last) layer owing to the slower solidification rate (Figure 5.11) and larger melt pool. No consistent relationship between the size of the primary arms in the overlapped and non-overlapped sections was observed.

Figures 5.13a and 5.13b compare the level of microsegregation of Nb and Mo in the γ phase in the bottom, middle, and top layers both measured experimentally using STEM-EDS and simulated with Scheil including solute trapping. For both elements, a promising agreement is observed between the STEM-EDS in the top-most layer and the Scheil segregation patterns especially towards the end of solidification. However, agreement between the bottom and middle layers experiencing reheating is poor. The top layer was not remelted, resolidified, or reheated, and therefore the microstructure is the nearest the solidification structure. In contrast, the bottom and middle layers experience these processes, which affect the microstructure evolution as a result of reheating, Figure 5.11 (a). Overall, although the Scheil with solute trapping solidification results provides a reliable estimate for predicting the segregation pattern resulting from solidification during LPBF, it is challenging to predict the final segregation pattern owing to the reheating phenomena. Figure 5.13 also shows that the bottom and middle layer have experienced homogenization due to the repeated reheating cycles.

Figures 5.14a and 5.14b compare the level of microsegregation of Nb and Mo in the γ phase in the bottom and middle layers as determined via STEM-EDS and the DICTRA simulations considering the reheating effects. As can be seen, the prediction is now much-improved, especially at the point of final solidification, and especially for Nb.

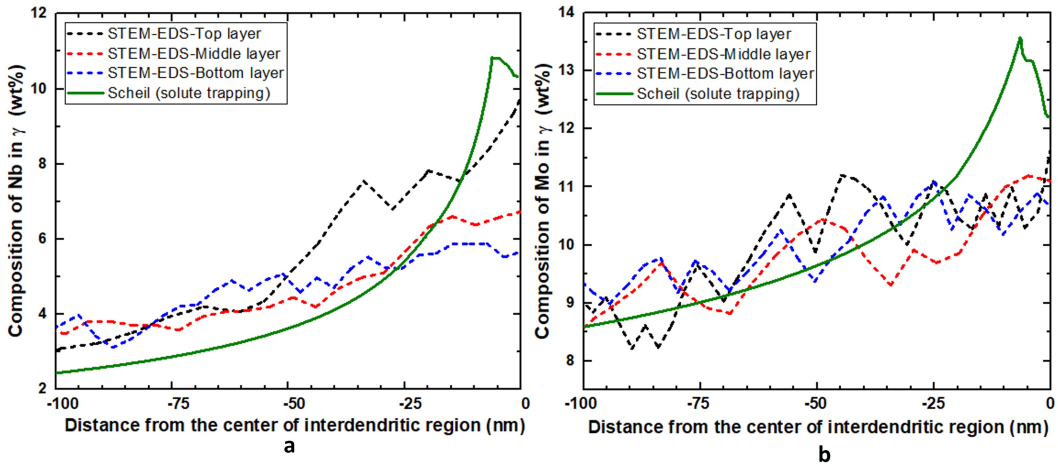

Figure 5.13: Composition profile of a) Nb b) Mo elements as within 100 μm distance from the interdendritic region calculated using Scheil solidification model and STEM-EDS line scan from the bottom region, middle region, and top region.

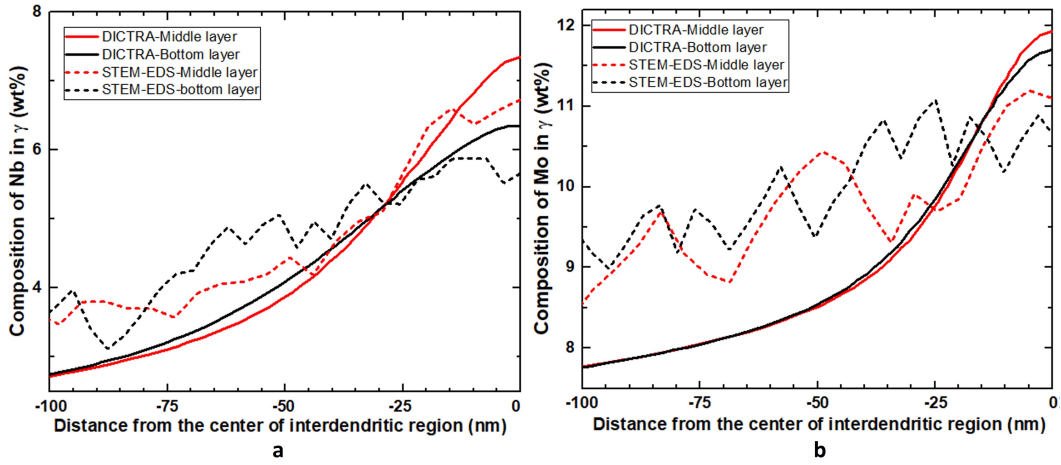

Figure 5.14: Composition profile of a) Nb b) Mo elements within 100 μm distance from the center of the interdendritic region simulated using DICTRA after reheating and EDS-line scan from the bottom region, middle region, and top region.

As shown in Figure 5.11, a deposited layer partially remelts during deposition of the next layer which was excluded from the DICTRA simulation. Re-solidification was also simulated using Scheil-Gulliver to evaluate the effect of resolidification on the composition of the last-to-solidify γ. The results are reported in table 5.4. As

Table 5.4: Scheil estimated the amount of alloying elements in the last 5 wt% of resolidified γ [29].

Element	**Cr**	**Nb**	**Mo**	**Fe**	**C**
IN625 Powder Composition (wt%)	22	3.74	9.3	2.8	0.02
Solidified γ composition (wt%)	20.61	10.84	13.57	2.05	0.022
Resolidified γ composition (wt%)	20.66	10.64	12.93	2.01	0.016

can be seen the amount of Cr, Nb, Mo,Fe and C are almost similar to the amount of these elements in the initial solidified microstructure of the γ phase. These results confirmed that using the as-solidified segregation profile as an input composition in DICTRA simulation is a valid assumption.

Figure 5.15 depicts the schematic of the thermal evolution and microstructure combined with the hardness results within the transverse cross-section from the bottom to the top layers of the LPBF IN625. As can be seen in 5.15 (a), The bottom and middle layer experience reheating that affect the level of homogenization and the precipitate variation and distribution. From the bottom to the top layers of the LPBF thin-wall, the magnitude of cooling rate and thermal gradient decrease which lead to an increase in the size of PDAS and grain as shown in Figure 5.15(b).

As demonstrated in Figure 5.7, 5.8, and 5.9, and appendix.A (5.8), HAADF-STEM analysis and the resulting FFT patterns identified γ', γ'', δ, laves, and Al_4C_3 precipitates in the bottom, NbC, γ', and Ni_2Al in the middle, and γ'' and NbC in the top layers of the build. As shown in (b), most of the precipitates were observed within the interdendritic region, which formed as a result of microsegregation, while only a few precipitates were observed inside the γ dendrites, mainly in the bottom layers. In the bottom and middle layers, due to the repeated heating and cooling cycles, the laves and NbC phases (i.e., the solidification products) can dissolve and

enrich the matrix with Nb, resulting in the formation of new precipitates inside the γ dendrites [36]. Solute trapping could be another reason to observe the precipitates inside the γ. Due to the higher cooling rate in the bottom layers, solute trapping may occur and result in the entrapment of Nb and the formation of the Nb-rich precipitates inside the dendrite [19]. No NbC precipitate was detected in the bottom layers because the higher cooling rate in this region suppresses the formation of the carbides during solidification [37], or some NbC precipitates might have formed but dissolved later during the reheating process. A few γ'-Ni_3(Al,Ti) precipitates were observed in the bottom and middle layers. Although γ' is the dominant straightening precipitates in most of the Inconel alloys, the formation of γ' is not common in the microstructure of IN625 due to the low content of Al in this alloy. However, γ' may form in the deposited layers (bottom and middle) during the deposition of the subsequent layers due to the reheating effect in LPBF process [4]. γ' might have been available in the top layer, but because they are very fine, we could not detect them. However, the γ' precipitates might have been coarsened during reheating process in the bottom and middle layers and became detectable. In the top layers, only the solidification products (γ'', Laves, and NbC) [23,18] was expected to be observed due to the minimal post-solidification heat exposure while the laves precipitate was not detected. Although the top-most layer does not experience reheating, the solidification cooling rate and thermal gradient are smaller and the melt's peak temperature is larger in the LPBF's top layer compared to a single-track solidification. In the topmost layer, a very high temperature might have caused the Cr evaporation and depletion of this layer from Cr, which could be the reason for not seeing laves precipitates.

Turning back to the hardness in Figure 5.15c, it is shown that hardness is location-dependent in the build direction. Along the build direction, from the bottom to the top, the hardness varied from 323 HV to 414 HV. The highest hardness is observed within the bottom layer due to the smaller PDAS. The hardness decreases from the bottom layer to the middle layer and then increases by moving toward the top layers, creating a U-shaped hardness variation pattern along the height. Although the PDAS increases from the bottom to the top layers, the hardness unexpectedly starts rising from the middle of the build height to the upper layers.

The reason for this rise in hardness is discussed below through investigation of links between the thermal evolution history, microstructural evolution, and hardness variation pattern in the bottom, middle, and top layers.

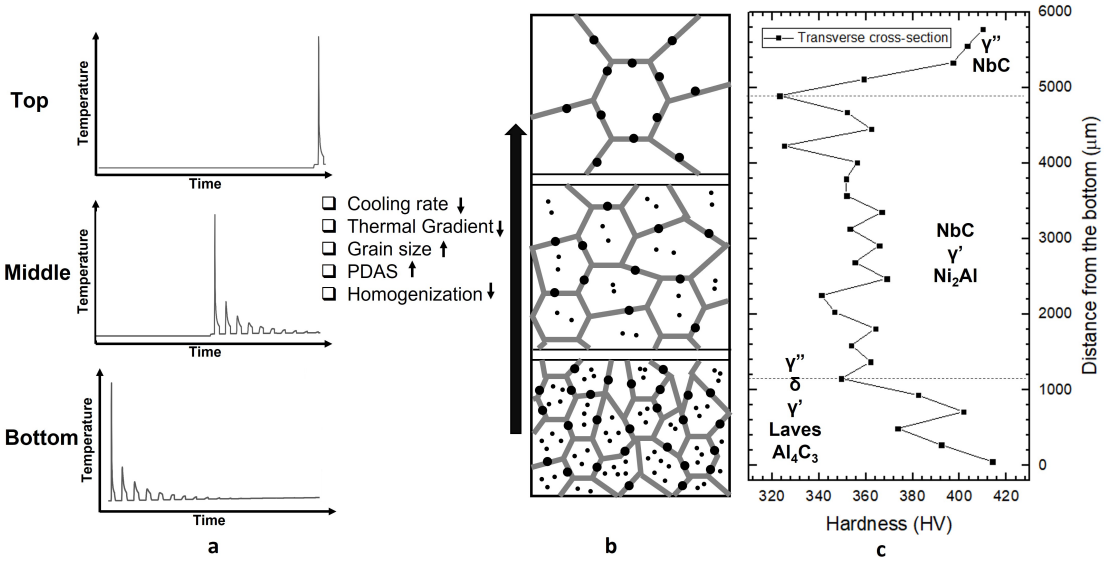

Figure 5.15: Composition profile of a) Nb b) Mo elements as within 100 μm distance from the interdendritic region calculated using Scheil solidification model and STEM-EDS line scan from the bottom region, middle region, and top region.

- **Homogenization effect:** In previous studies [38,39], it was observed that the

homogenized structure showed a lower hardness as compared to the as-built structure, which can be one of the reasons for the increase of the hardness in the upper layers as the level of the homogenization decreases from the bottom to the top layers. Although the degree of homogenization is highest in the bottom layer, precipitation hardening as well as the PDAS and grain size effects prevail over the effect of homogenization on hardness resulting in the highest hardness in the bottom layer.

- **Precipitation effect:** More NbC was observed in the middle layer compared to the top layers, which could be responsible for the higher hardness in the upper layers because generally, laves and carbides decrease the hardness and tensile strength while γ', γ'' (Ni3Nb), and δ enhance the hardness and tensile strength.

- **Residual stress:** An uneven distribution of the residual stresses and built-in dislocation density could be another reason for the mechanical heterogeneity, which is beyond the scope of this study.

We can use the results shown in Figures 5.2 to 5.15 to understand better the initial microstructural heterogeneity in an as-built multi-layer LPBF IN625. Only through doing all of this work one can demonstrate the process-microstructure-property relationship that exists for hardening behavior in nickel-based superalloys. LPBF manufactured parts often show more inconsistent properties as compared to wrought materials [35]. Thus, The LPBF processing is usually followed by heat treatment to eliminate any microstructural heterogeneity and release the residual stresses. However, in IN625, an improper heat treatment design could also lead to the growth or

formation of different precipitates, including laves and carbides, that might affect the high-temperature mechanical properties, including part embrittlement. (16). Thus, understanding the as-build LPBF microstructure and the process-microstructure-properties relationship is also important to design an appropriate heat-treatment process to achieve suitable mechanical properties and reduce the alloy development cost.

5.6 Conclusions

In this study, a detailed analysis of the microstructural and mechanical heterogeneity in an as-built LPBF IN625 thin-wall was performed utilizing electron microscopy, FEA thermal simulation, and CALPHAD. The microstructure of the LPBF IN625 was found to contain mostly columnar grains that grew epitaxially from the substrate or previous layer. From the bottom to the top layers of the LPBF build, the size of the melt pools, grains, and dendrites increased due to the decrease in the cooling rate and thermal gradient resulting from the heat accumulation. The hardness decreased from 414HV to 323HV from the bottom layers to the middle layers, which was related to the increase in the grains and dendrites sizes. However, an increase in hardness was observed by moving from the middle to the top layers despite containing larger grains and PDAS. Both STEM-EDS results and DICTRA simulation of the microsegregation profile from the bottom, middle, and top layers, confirmed that the bottom layer was slightly homogenized in comparison to the upper layers, which could be the reason for obtaining higher hardness in the upper layer. A promising agreement was also observed between the experimental and DICTRA/FEA thermal simulations of the microsegregation profile. Replacing experiments with a combined DICTRA/FEA

thermal simulation approach would help to reduce alloy development costs for additive manufacturing by reducing the number of expensive and time-consuming experiments needed. A variety of precipitates, including γ', γ'', δ, laves, and Al_4C_3, was observed in the bottom layers of the build. Most of these precipitates were seen in the inter-dendritic region, while only a few were seen within the γ dendrites. In the middle layer, NbC, γ', and Ni_2Al precipitates were found, while in the upper layers, the near eutectic products i.e., NbC and γ'' were observed. Compared to the middle layers, more γ'' and fewer NbC were found within the upper layers which could be another reason for the higher hardness in this region.

5.7 Acknowledgement

The authors acknowledge funding from the National Sciences and Engineering Council of Canada, and experimental support from McMaster's Additive Manufacturing Research Group. Electron microscopy was carried out at the Canadian center for Electron Microscopy (CCEM), a national facility supported by the Canada Foundation for Innovation under the Major Science Initiatives program, NSERC and McMaster University.

5.8 Appendix. A. STEM-EDS line scans from precipitate-like particles

Figures 5.16 and 5.17 show the STEM-EDS line scans traversing the precipitate-like particles in the bottom and top regions, respectively.

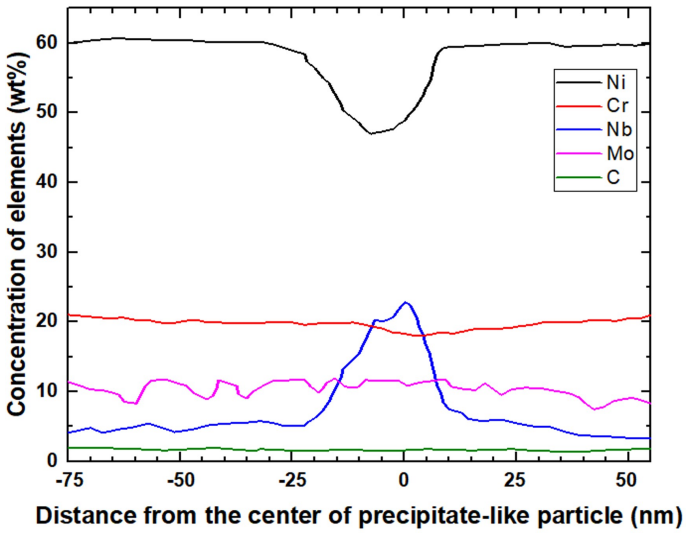

Figure 5.16: STEM-EDS line scans traversing the precipitate-like particles in the bottom region.

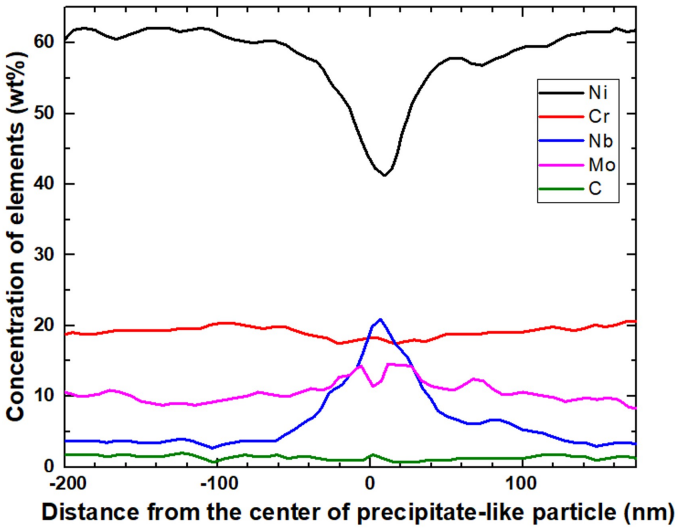

Figure 5.17: STEM-EDS line scans traversing the precipitate-like particles in the top region.

References

[1] V. Shankar, K. B. S. Rao, and S. Mannan, "Microstructure and mechanical properties of inconel 625 superalloy," *Journal of nuclear materials*, vol. 288,

no. 2-3, pp. 222–232, 2001.

[2] M. Shaikh, M. Ahmad, K. Shoaib, J. Akhter, and M. Iqbal, "Precipitation hardening in inconel* 625," *Materials science and technology*, vol. 16, no. 2, pp. 129–132, 2000.

[3] G. Dey, S. Albert, D. Srivastava, M. Sundararaman, and P. Mukhopadhyay, "Microstructural studies on rapidly solidified inconel 625," *Materials Science and Engineering: A*, vol. 119, pp. 175–184, 1989.

[4] G. Dinda, A. Dasgupta, and J. Mazumder, "Laser aided direct metal deposition of inconel 625 superalloy: Microstructural evolution and thermal stability," *Materials Science and Engineering: A*, vol. 509, no. 1-2, pp. 98–104, 2009.

[5] K. Amato, J. Hernandez, L. Murr, E. Martinez, S. Gaytan, P. Shindo, and S. Collins, "Comparison of microstructures and properties for a ni-base superalloy (alloy 625) fabricated by electron and laser beam melting," *Journal of Materials Science Research*, vol. 1, no. 2, p. 3, 2012.

[6] L. E. Murr, S. M. Gaytan, D. A. Ramirez, E. Martinez, J. Hernandez, K. N. Amato, P. W. Shindo, F. R. Medina, and R. B. Wicker, "Metal fabrication by additive manufacturing using laser and electron beam melting technologies," *Journal of Materials Science & Technology*, vol. 28, no. 1, pp. 1–14, 2012.

[7] M. Sundararaman, L. Kumar, G. E. Prasad, P. Mukhopadhyay, and S. Banerjee, "Precipitation of an intermetallic phase with pt 2 mo-type structure in alloy 625," *Metallurgical and Materials Transactions A*, vol. 30, no. 1, pp. 41–52, 1999.

[8] J. DuPont, "Solidification of an alloy 625 weld overlay," *Metallurgical and Materials Transactions A*, vol. 27, no. 11, pp. 3612–3620, 1996.

[9] W. J. Sames, F. List, S. Pannala, R. R. Dehoff, and S. S. Babu, "The metallurgy and processing science of metal additive manufacturing," *International Materials Reviews*, vol. 61, no. 5, pp. 315–360, 2016.

[10] T. DebRoy, H. Wei, J. Zuback, T. Mukherjee, J. Elmer, J. Milewski, A. M. Beese, A. d. Wilson-Heid, A. De, and W. Zhang, "Additive manufacturing of metallic components–process, structure and properties," *Progress in Materials Science*, vol. 92, pp. 112–224, 2018.

[11] W. J. Sames, K. A. Unocic, R. R. Dehoff, T. Lolla, and S. S. Babu, "Thermal effects on microstructural heterogeneity of inconel 718 materials fabricated by electron beam melting," *Journal of materials research*, vol. 29, no. 17, pp. 1920–1930, 2014.

[12] F. Zhang, L. E. Levine, A. J. Allen, M. R. Stoudt, G. Lindwall, E. A. Lass, M. E. Williams, Y. Idell, and C. E. Campbell, "Effect of heat treatment on the microstructural evolution of a nickel-based superalloy additive-manufactured by laser powder bed fusion," *Acta materialia*, vol. 152, pp. 200–214, 2018.

[13] A. Kreitcberg, V. Brailovski, and S. Turenne, "Elevated temperature mechanical behavior of in625 alloy processed by laser powder-bed fusion," *Materials Science and Engineering: A*, vol. 700, pp. 540–553, 2017.

[14] P. Mohammadpour, A. Plotkowski, and A. B. Phillion, "Revisiting solidification

microstructure selection maps in the frame of additive manufacturing," *Additive Manufacturing*, vol. 31, p. 100936, 2020.

[15] C. Li, R. White, X. Fang, M. Weaver, and Y. Guo, "Microstructure evolution characteristics of inconel 625 alloy from selective laser melting to heat treatment," *Materials Science and Engineering: A*, vol. 705, pp. 20–31, 2017.

[16] A. Kreitcberg, V. Brailovski, and S. Turenne, "Effect of heat treatment and hot isostatic pressing on the microstructure and mechanical properties of inconel 625 alloy processed by laser powder bed fusion," *Materials Science and Engineering: A*, vol. 689, pp. 1–10, 2017.

[17] S. Li, Q. Wei, Y. Shi, Z. Zhu, and D. Zhang, "Microstructure characteristics of inconel 625 superalloy manufactured by selective laser melting," *Journal of Materials Science & Technology*, vol. 31, no. 9, pp. 946–952, 2015.

[18] T. Keller, G. Lindwall, S. Ghosh, L. Ma, B. M. Lane, F. Zhang, U. R. Kattner, E. A. Lass, J. C. Heigel, Y. Idell, *et al.*, "Application of finite element, phase-field, and calphad-based methods to additive manufacturing of ni-based superalloys," *Acta materialia*, vol. 139, pp. 244–253, 2017.

[19] G. Marchese, M. Lorusso, S. Parizia, E. Bassini, J.-W. Lee, F. Calignano, D. Manfredi, M. Terner, H.-U. Hong, D. Ugues, *et al.*, "Influence of heat treatments on microstructure evolution and mechanical properties of inconel 625 processed by laser powder bed fusion," *Materials Science and Engineering: A*, vol. 729, pp. 64–75, 2018.

[20] E. A. Lass, M. R. Stoudt, M. E. Williams, M. B. Katz, L. E. Levine, T. Q.

Phan, T. H. Gnaeupel-Herold, and D. S. Ng, "Formation of the ni 3 nb δ-phase in stress-relieved inconel 625 produced via laser powder-bed fusion additive manufacturing," *Metallurgical and Materials Transactions A*, vol. 48, no. 11, pp. 5547–5558, 2017.

[21] E. A. Lass, M. R. Stoudt, M. B. Katz, and M. E. Williams, "Precipitation and dissolution of δ and γ'' during heat treatment of a laser powder-bed fusion produced ni-based superalloy," *Scripta Materialia*, vol. 154, pp. 83–86, 2018.

[22] K. Gola, B. Dubiel, and I. Kalemba-Rec, "Microstructural changes in inconel 625 alloy fabricated by laser-based powder bed fusion process and subjected to high-temperature annealing," *Journal of Materials Engineering and Performance*, pp. 1–7, 2020.

[23] P. Mohammadpour, H. Yuan, and A. Phillion, "Microstructure evolution of inconel 625 alloy during single-track laser powder bed fusion," *Additive Manufacturing*, vol. 55, p. 102824, 2022.

[24] Y. Kok, X. P. Tan, P. Wang, M. Nai, N. H. Loh, E. Liu, and S. B. Tor, "Anisotropy and heterogeneity of microstructure and mechanical properties in metal additive manufacturing: A critical review," *Materials & Design*, vol. 139, pp. 565–586, 2018.

[25] Z. Liu, D. Zhao, P. Wang, M. Yan, C. Yang, Z. Chen, J. Lu, and Z. Lu, "Additive manufacturing of metals: Microstructure evolution and multistage control," *Journal of Materials Science & Technology*, vol. 100, pp. 224–236, 2022.

[26] Z. Wang, E. Denlinger, P. Michaleris, A. D. Stoica, D. Ma, and A. M. Beese,

"Residual stress mapping in inconel 625 fabricated through additive manufacturing: Method for neutron diffraction measurements to validate thermomechanical model predictions," *Materials & Design*, vol. 113, pp. 169–177, 2017.

[27] Y. Zhao, K. Li, M. Gargani, and W. Xiong, "A comparative analysis of inconel 718 made by additive manufacturing and suction casting: Microstructure evolution in homogenization," *Additive Manufacturing*, vol. 36, p. 101404, 2020.

[28] F. Xu, Y. Lv, Y. Liu, F. Shu, P. He, and B. Xu, "Microstructural evolution and mechanical properties of inconel 625 alloy during pulsed plasma arc deposition process," *Journal of Materials Science & Technology*, vol. 29, no. 5, pp. 480–488, 2013.

[29] J.-O. Andersson, T. Helander, L. Höglund, P. Shi, and B. Sundman, "Thermo-calc & dictra, computational tools for materials science," *Calphad*, vol. 26, no. 2, pp. 273–312, 2002.

[30] H. Larsson, "A model for 1d multiphase moving phase boundary simulations under local equilibrium conditions," *Calphad*, vol. 47, pp. 1–8, 2014.

[31] "Thermo-calc software version2021b, TCNI10 and MOBNI5 nickel/ni-alloys database," 2021.

[32] H. Azizi, A. Ebrahimi, N. Ofori-Opoku, M. Greenwood, N. Provatas, and M. Mohammadi, "Characterizing the microstructural effect of build direction during solidification of laser-powder bed fusion of al-si alloys in the dilute limit: a phase-field study," *Acta Materialia*, vol. 214, p. 116983, 2021.

[33] P. Promoppatum, S.-C. Yao, P. C. Pistorius, and A. D. Rollett, "A comprehensive comparison of the analytical and numerical prediction of the thermal history and solidification microstructure of inconel 718 products made by laser powder-bed fusion," *Engineering*, vol. 3, no. 5, pp. 685–694, 2017.

[34] Y. M. Arısoy, L. E. Criales, and T. Özel, "Modeling and simulation of thermal field and solidification in laser powder bed fusion of nickel alloy in625," *Optics & Laser Technology*, vol. 109, pp. 278–292, 2019.

[35] N. Ramenatte, A. Vernouillet, S. Mathieu, A. V. Put, M. Vilasi, and D. Monceau, "A comparison of the high-temperature oxidation behaviour of conventional wrought and laser beam melted inconel 625," *Corrosion Science*, vol. 164, p. 108347, 2020.

[36] R. M. Kindermann, M. Roy, R. Morana, and P. B. Prangnell, "Process response of inconel 718 to wire+ arc additive manufacturing with cold metal transfer," *Materials & Design*, vol. 195, p. 109031, 2020.

[37] B. Guo, Y. Zhang, F. He, J. Ma, J. Li, Z. Wang, J. Wang, J. Feng, W. Wang, and L. Gao, "Origins of the mechanical property heterogeneity in a hybrid additive manufactured hastelloy x," *Materials Science and Engineering: A*, vol. 823, p. 141716, 2021.

[38] F. Xu, Y. Lv, Y. Liu, B. Xu, and P. He, "Effect of heat treatment on microstructure and mechanical properties of inconel 625 alloy fabricated by pulsed plasma arc deposition," *Physics Procedia*, vol. 50, pp. 48–54, 2013.

[39] A. A. Gamon, *Microstructure and Hardness Comparison of Inconel 625 Alloy*

of Various Additive Manufacturing Processes Following Heat Treatments. PhD thesis, The University of Texas at El Paso, 2021.

Chapter 6

Summary and Conclusions

6.1 Summary and conclusive remarks

INCONEL 625 (IN625) is one of the most widely used nickel-based superalloys because of its excellent properties, especially the high-temperature corrosion, fatigue resistance, and high tensile strength. These properties make this alloy a prime candidate in the marine, aerospace, and nuclear industries. IN625 exhibits poor machinability while good weldability. Laser Powder Bed Fusion (LPBF) is an additive manufacturing (AM) technique with better dimensional accuracy and versatility compared to other AM methods. Thus, LPBF can be used as a promising choice to fabricate IN625 alloy. As mentioned, this alloy is being used in sensitive industries; therefore, a high level of quality assurance is needed for the manufactured part.

The LPBF processing of IN625 alloy has been studied over the past decade. Most of the studies focused on printability, mechanical properties, effects of heat treatment on the properties, and the correlation of processing parameters and mechanical properties of this alloy, but paying less attention to the Process-Structure-Property

(PSP) relationship . Microstructure is the heart of any AM process, which links the processing parameters to the properties of the AM part. Therefore, it is essential to investigate the microstructural evolution happening during the LPBF process of IN625 and the PSP relationship to guide, develop, and speed up the fabrication process or part design and guarantee quality assurance. This study focuses on the correlation between processing parameters, microstructure, and mechanical properties of IN625 manufactured using the LPBF process.

Knowledge of solidification is required to produce metal parts using AM techniques. Solidification conditions control the microstructure, defects, and, therefore, the properties of components. To study the resulting solidification microstructure and grain morphology of LPBF-produced multi-component alloys, a theoretical concept, so-called "Solidification Microstructure Selection (SMS) maps," was revisited and developed. The theory has been derived with analytical methods that predict the grain morphology and the interface response of the possible solidification morphologies that are potentially available at high thermal gradients and solidification velocities. The results from the SMS map method study showed that this method is an informative tool that efficiently maps the process–microstructure relationship for a range of processing parameters which will enhance the tailoring of the final AM part properties. The predictions of the SMS map method are approximate but useful for efficient qualitative or semi-quantitative analysis of experimental results.

The SMS map approach was implemented to predict the solidification microstructure and grain morphology of an as-built single-track LPBF IN625. A set of single-track LPBF experiments was also performed to validate the simulation results. It is found that the modes of solidification and grain morphology formed during LPBF

processing are significantly influenced by the thermal gradient (G), solidification velocity (V), and the initial composition (C_0) of the alloy. The value of G and V is dependent on the processing parameters and the location within the melt pool. The moving heat source during the LPBF process causes the uneven distribution of G and V values in the melt pool, leading to the variation of solidification modes, grain size, and Primary Dendrite Arm Spacing (PDAS) in the single melt pool. The experimentally LPBF microstructure of IN625 was found to mainly contain γ-FCC(Ni-Cr) columnar dendrites, which grow epitaxially from the substrate. A few equiaxed grains were observed to nucleate ahead of the columnar front due to a drop in the thermal gradient at the end of the melt pool's solidification. Although the columnar solidification is correctly predicted by the SMS map, the columnar to equiaxed transition was not anticipated by the analytical solution. This can be related to the overestimation of the thermal gradient value at the center of the melt pool by the Rosenthal solution. The PDAS values measured experimentally were shown to closely agree with the analytical models' prediction. A small discrepancy shown between the experimental and analytical results of PDAS values could be related to the uncertainties in materials properties, especially the diffusion coefficient in the liquid and the potential for Marangoni-induced convection.

Although the SMS map correctly predicted the dendritic *gamma* phase, the analytical solution was not incapable of predicting formation of precipitates. On the other hand, using the CALculation of PHAse Diagrams (CALPHAD) approach, it is found that some precipitates may form at the end of the solidification. Thus, electron microscopy and computational thermodynamics were implemented to further investigate the solidification microstructure, microsegregation patterns, and the formation of the

precipitates in the LPBF microstructure of the IN625. Both experimental (STEM-EDS) and thermodynamic simulation (Scheil and DICTRA) results confirmed significant microsegregation with the highest level of segregation towards the interdendritic region. This caused the compositional heterogeneity in the microstructure and may help meta-stable precipitate to nucleate within the interdendritic region. Although the DICTRA simulation overestimated the level of microsegregation during the solidification, the Scheil–Gulliver with solute trapping simulation was found to match closely to the experimentally-obtained microsegregation patterns. HAADF-STEM analysis identified the highly concentrated Nb areas as γ'', Laves, and NbC precipitates, while Scheil-Gulliver simulation (with solute trapping) confirmed the formation of γ'' and NbC but not Laves at the end of rapid solidification. The driving force for the formation of potential precipitates at the end of solidification was also calculated using the CALPHAD approach. Although the driving force analysis showed that NbC, M_2C, μ, δ, M_6C, and γ'' precipitates can form within the last solidified liquid, M_2C, μ, δ and M_6C precipitates were not observed in the as-solidified microstructure which can be related to the solute trapping effect. The non-equilibrium solid/liquid interface and the occurrence of solute trapping may create specific thermal and compositional conditions unfavorable for the formation of these precipitates.

Finally, a detailed analysis of the layer-by-layer melting and rapid solidification as well as the microstructural and mechanical heterogeneity in an as-built multi-layer LPBF IN625 was carried out using electron microscopy, FEA thermal simulation, and CALPHAD approach. The microstructure mostly contained columnar grains that grow epitaxially from the substrate or previous layer. The size of the melt pools, grains, and dendrites was found to increase from the bottom to the top layers of the

LPBF part due to the decrease in the solidification cooling rate and thermal gradient and the increase in the peak temperature. Heat accumulation during the layered LPBF process was shown to be responsible for this governing thermal condition. The microsegregation profile obtained by DICTRA/FEA thermal simulation showed to match closely to the experimentally measured one. From the bottom to the top layers, the hardness decreased toward the middle layers and then started increasing towards the top layers despite containing larger grains and PDAS. The highest hardness (414 HV) was observed in the bottom layers, which was related to the smaller grains and dendrites in this area compared to the upper layers. Both the experimental results and the DICTRA simulations of the microsegregation profiles at the bottom, middle, and top layers confirmed that the level of compositional homogenization slightly decreased from the bottom to the upper layers because of the reheating effect. The increase in the hardness in the top layers could be related to the minimal homogenization in the top layers. Although the degree of homogenization is the highest in the bottom layers, the effect of grain and dendrite size on the hardness seemed to prevail over the homogenization effect. The distribution of the precipitates was shown to be location-dependent in the multi-layer LPBF part. The various types of precipitates, including γ', γ'', δ, NbC, laves, and Al_4C_3 were observed in the bottom layers. Most of these precipitates were seen in the interdendritic region, while only a few were seen within the γ dendrites. The presence of γ', γ'', and δ, could have been another reason for the highest hardness in the bottom region. NbC, γ', and Ni_2Al precipitates were detected in the middle layer, and the near eutectic products, i.e., NbC and γ'' were observed in the upper layers. Another reason for the higher hardness in the upper layers compared to the middle region could be the presence of more γ'' and fewer

NbC in the top layers.

6.2 Limitations and future work

The limitations of this study, along with some potential future works to the present findings, can be listed as follows:

- **Study of SMS map:** The first limitation is the availability of thermodynamic data; for some alloying systems, only limited information is available in the literature or the computational thermodynamic databases. The second limitation could be all the simplifying assumptions made in SMS simulations; such as directional solidification in the scale of dendrites, steady state solidification, linear phase diagram, constant values for nucleant density and nucleation undercooling in CET calculation, neglecting the convection in the melt pool and Marangoni flow in Rosenthal thermal simulation, and unidirectional heat flow. And finally, the prediction is limited to the solidification of a single melt pool; however, in the industrial LPBF process, the deposition of the following layer will affect the microstructure of the first layer. To enhance the functionality of SMS map method in AM, there is a need to improve the availability of thermodynamic data for new alloy systems and enhance the characterization methods to estimate the nucleant density and equiaxed nucleation undercooling more accurately. Further, it is required to develop new approaches that can use the interface response method without the assumptions of a linear phase diagram and a unidirectional heat flow. Eventually, due to the layered nature of AM, it is also beneficial to couple the SMS map approach with micro-scale numerical

heat transfer methods (considering the convection) to enhance the microstructure prediction.

- **Study of microstructural and mechanical heterogeneity in the as-built LPBF IN625:** The mechanical properties evaluation was limited to the hardness test in the multi-layer LPBF part. Investigating the other mechanical properties, such as residual stress, tensile strength, and fatigue test, would be beneficial in an as-built LPBF part. This will help to increase the understanding of the PSP relationship and ultimately, obtain higher-quality products. In another future study, one could use the finding from this work to design a heat-treatment process to achieve the desired property. Further, in the FEA, a few simplifying assumptions, including considering the single-track deposition in each layer and scan strategy rotation (SSR) equal to 0°, might have affected the accuracy of the PSP evaluation. To improve the accuracy of the thermal analysis, an FEA model that is able to simulate the thermal condition of all deposited layers with different SSR angles is required. The other alternative to the FEA thermal analysis could be the enhancement of the In-situ thermal measurement methods.

6.3 Contribution

This study provides fundamental insight into the process-microstructure-property relations during LPBF of IN625 and can help industries select appropriate processing parameters selection and improve quality assurance. The overall contributions of this study to the literature can be identified as follows:

- **Processing parameter selection:** SMS maps are useful tools for predicting and tracking phase transformation and designing the LPBF process as they obtain desirable microstructure by manipulating process parameters. The knowledge of the process-microstructure relationship will also aid in expanding the use of LPBF for diverse applications.

- **Quality assurance:** The results from this study will help researchers to better understand the correlation between microstructural evolution and mechanical properties of as-built LPBF IN625. Moreover, the LPBF process is usually followed by post heat-treatment process to eliminate the residual stresses or to homogenize the microstructure. The findings from this study which include a thorough investigation of solidification and solid-state transformation, can be used as a guideline to design an appropriate heat treatment process to achieve high-quality products with desired properties.

- **Research and development:** Replacing experiments with Scheil model (with solute trapping) and a combined DICTRA/FEA thermal simulation approach will help to reduce alloy development costs for additive manufacturing by reducing the number of expensive and time-consuming experiments needed to investigate the compositional segregation during rapid solidification and reheating process.

To improve the accuracy of the thermal analysis, a FEA model that is to be able to simulate thermal condition of all deposited layers with different SSR angles is required.